

Supporting Information

Tailoring the π -system of benzimidazole ligands towards stable light-harvesting cyclometalated iridium(III) complexes

Sergei V. Tatarin, Daniil E. Smirnov, Ilya V. Taydakov, Mikhail T. Metlin, Victor V. Emets and Stanislav I. Bezzubov*
*

Table of Content

1. NMR and HRMS spectra.
2. X-ray data.
3. Redox and optical properties
4. Computational details
5. Photovoltaic measurements

1. NMR and mass spectra.

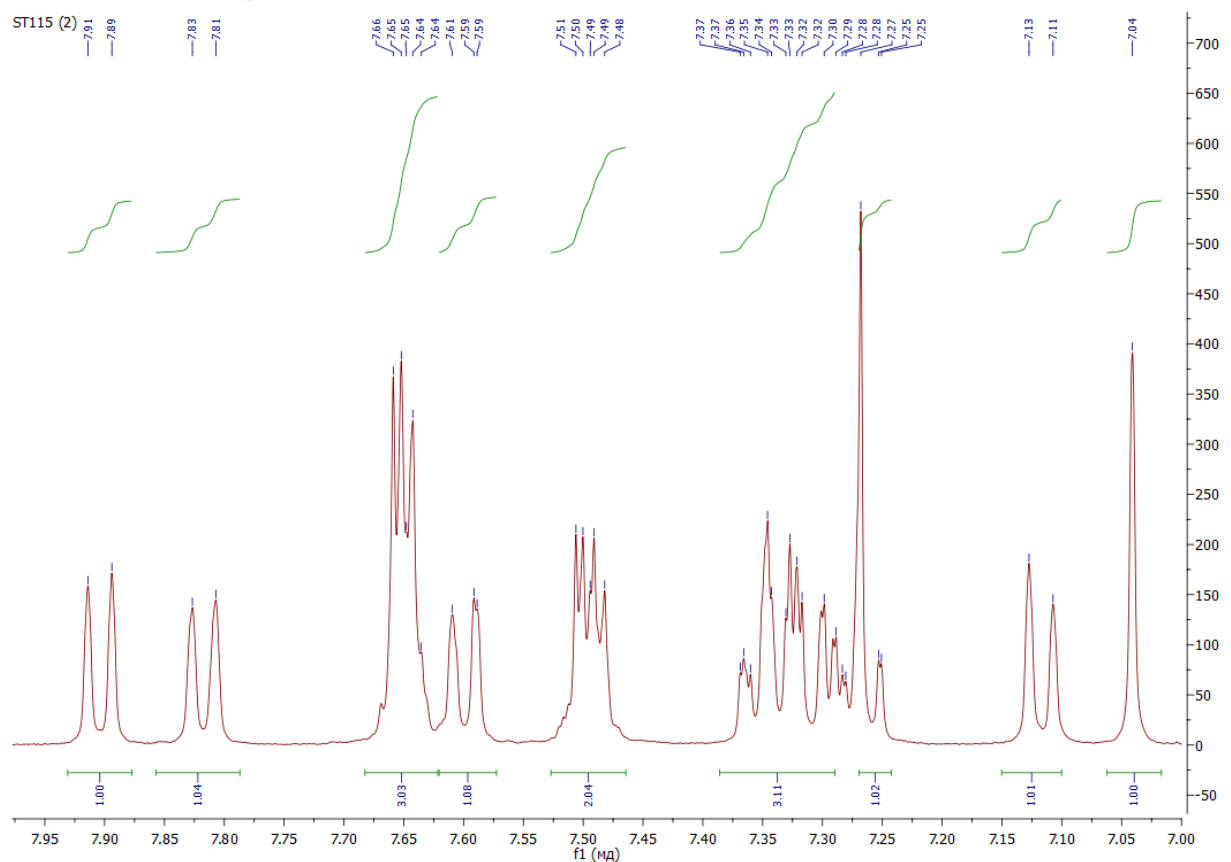


Figure S1. ^1H NMR spectrum of btbi (400 MHz, 298K, CDCl_3).

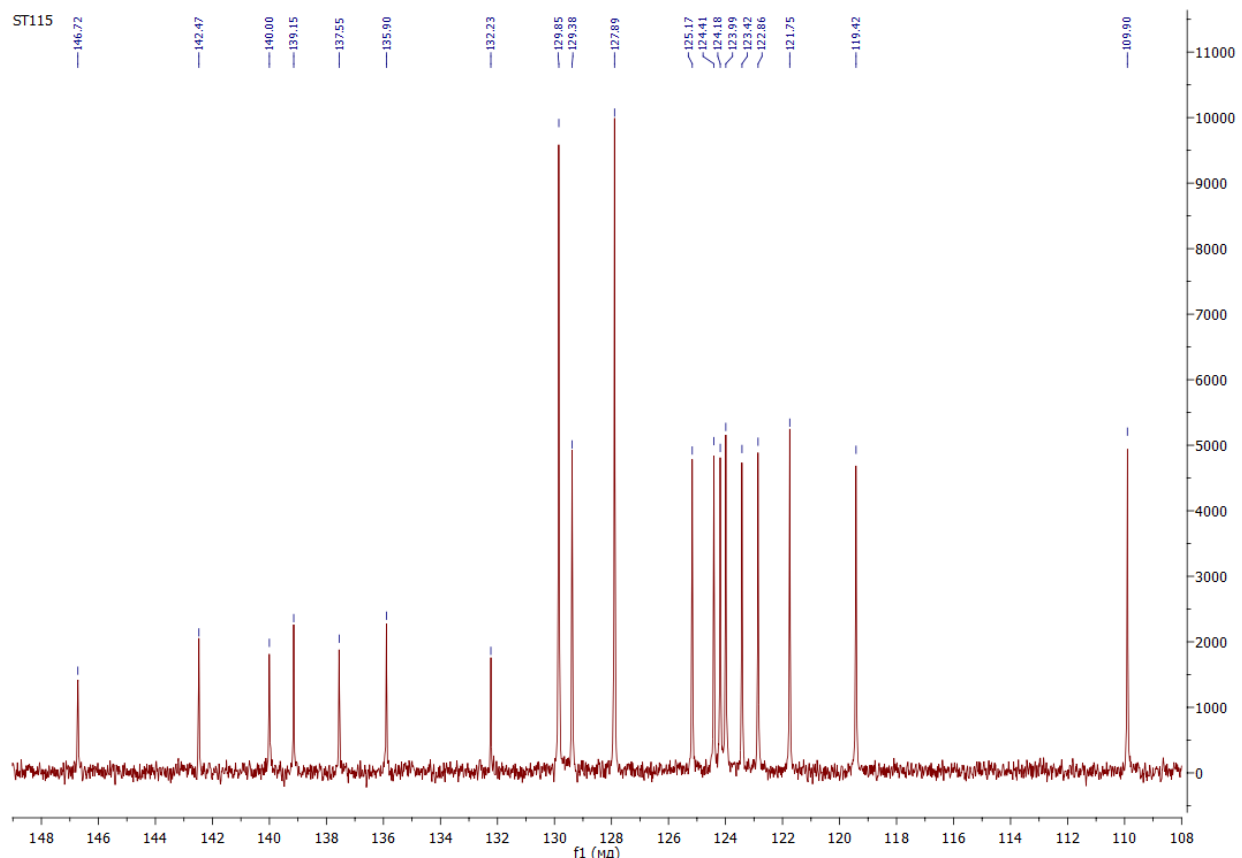


Figure S2. ^{13}C $\{{}^1\text{H}\}$ NMR spectrum of btbi (101 MHz, 298K, CDCl_3).

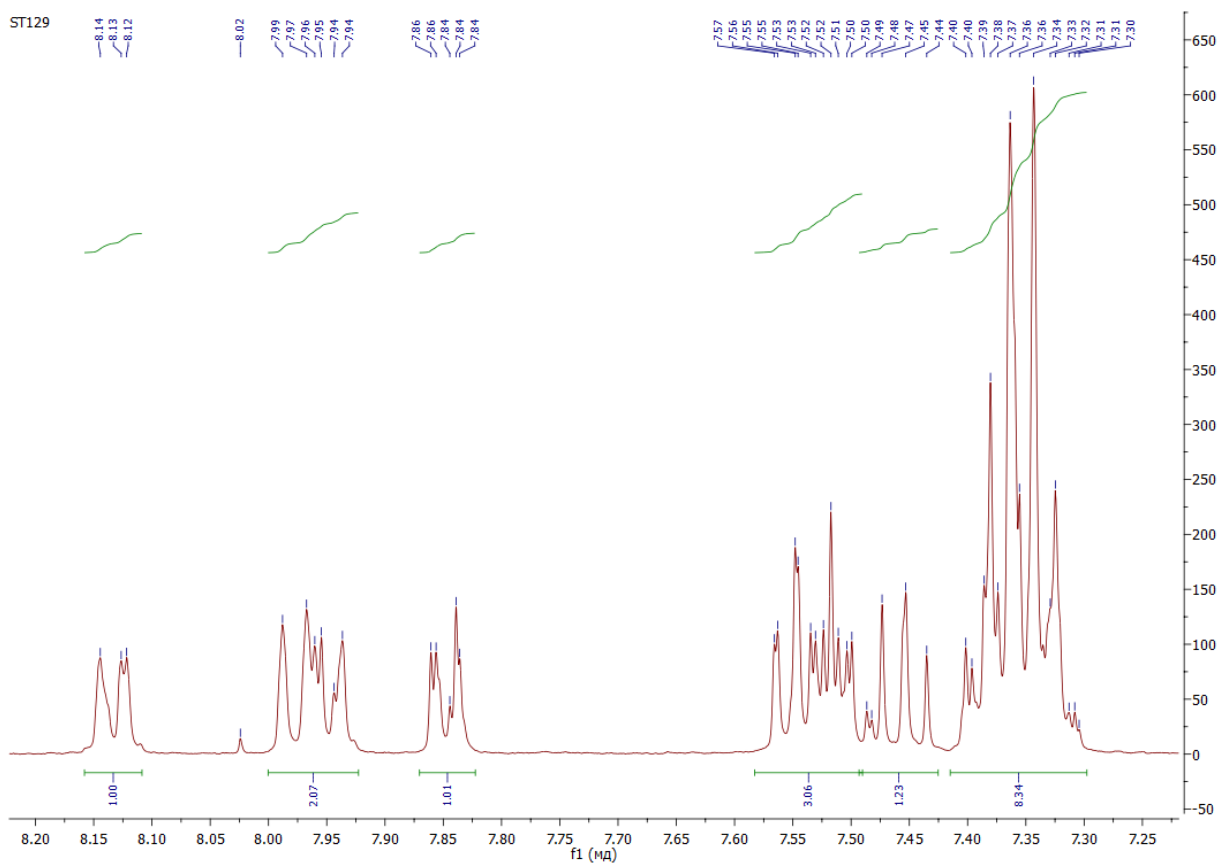


Figure S3. ^1H NMR spectrum of nbi-1 (400 MHz, 298K, acetone-D₆).

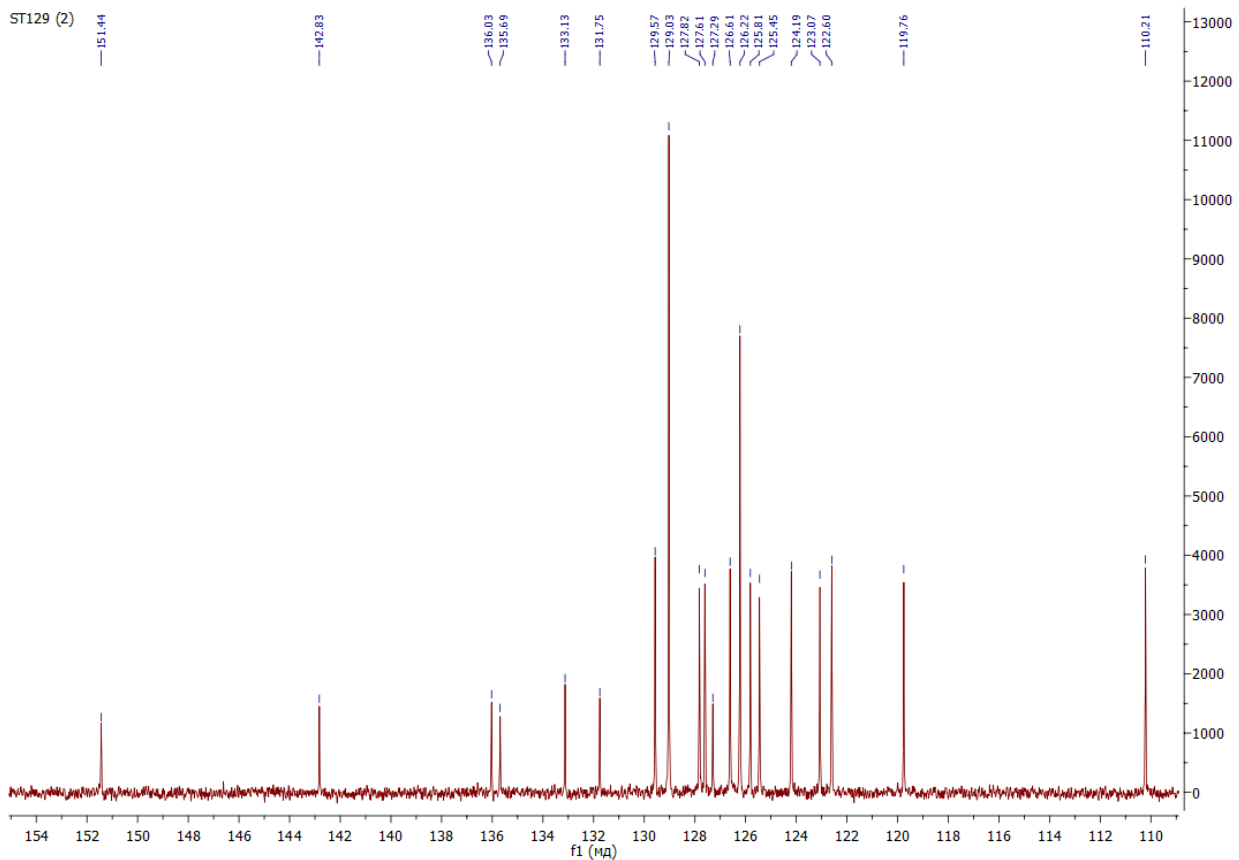


Figure S4. $^{13}\text{C}\{^1\text{H}\}$ NMR spectrum of nbi-1 (101 MHz, 298K, CDCl₃).

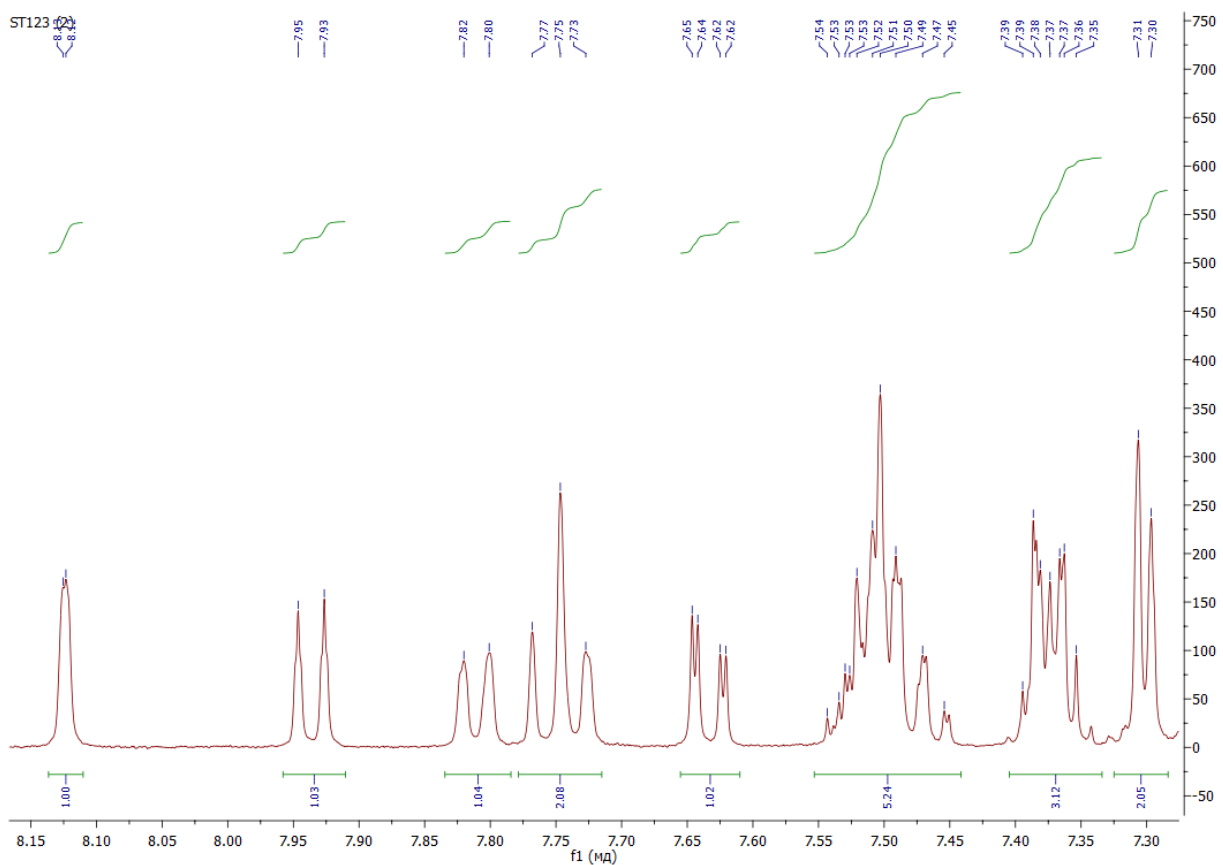


Figure S5. ^1H NMR spectrum of nbi-2 (400 MHz, 298K, CDCl_3).

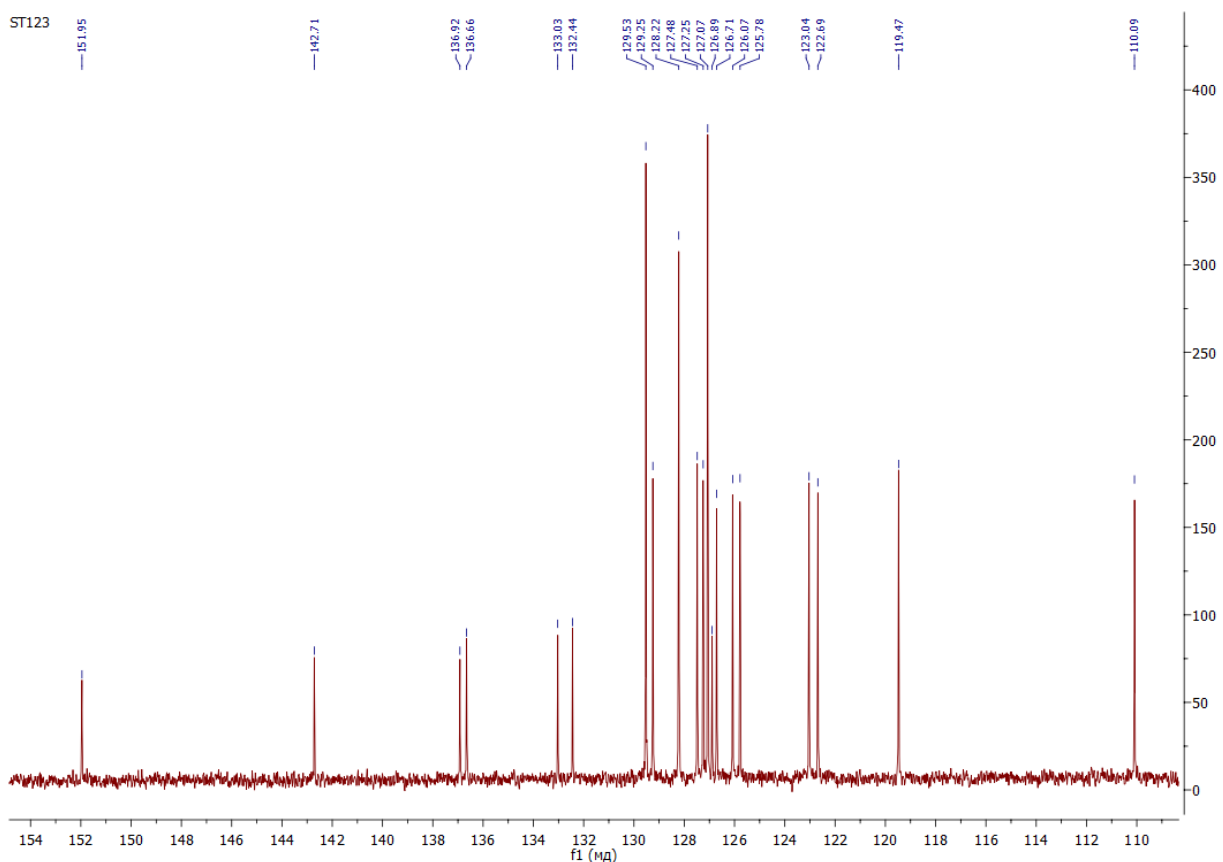


Figure S6. $^{13}\text{C}\{^1\text{H}\}$ NMR spectrum of nbi-2 (101 MHz, 298K, CDCl_3).

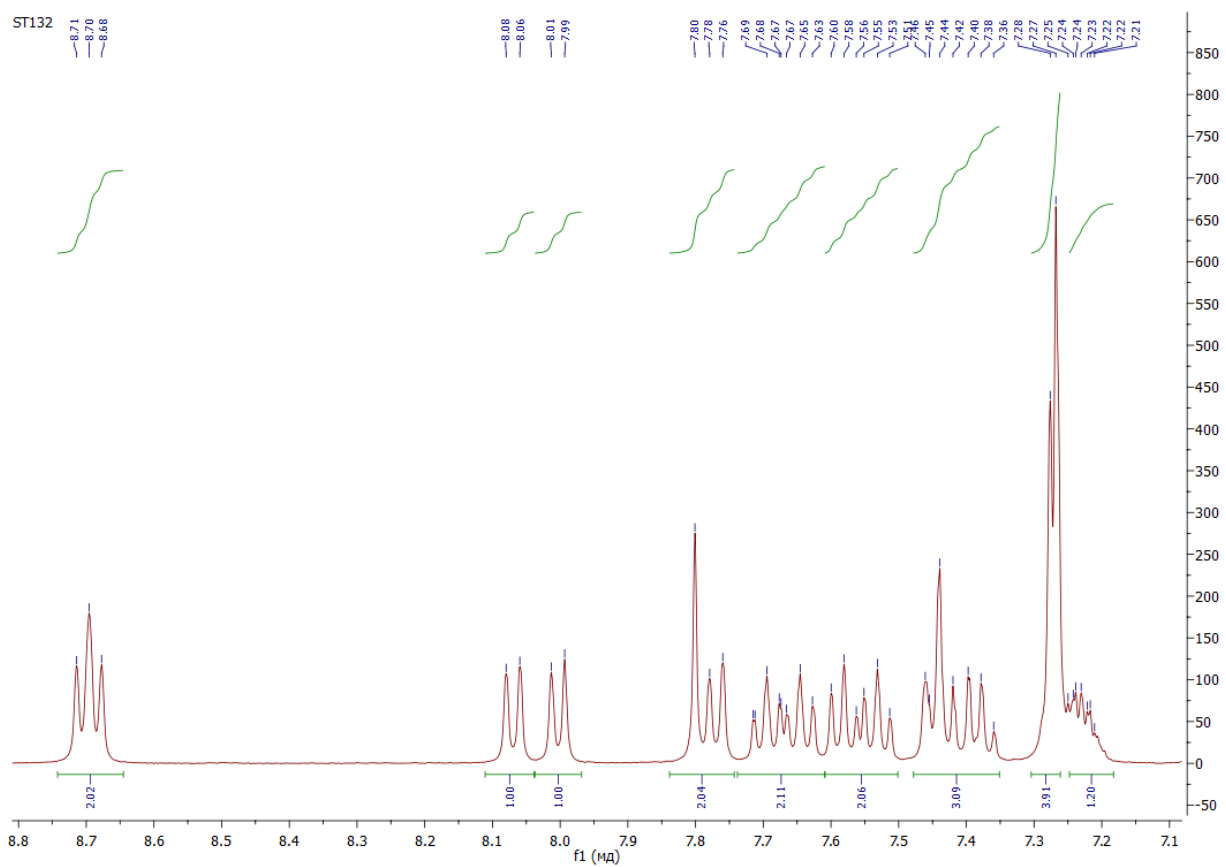


Figure S7. ¹H NMR spectrum of phbi (400 MHz, 298K, CDCl₃).

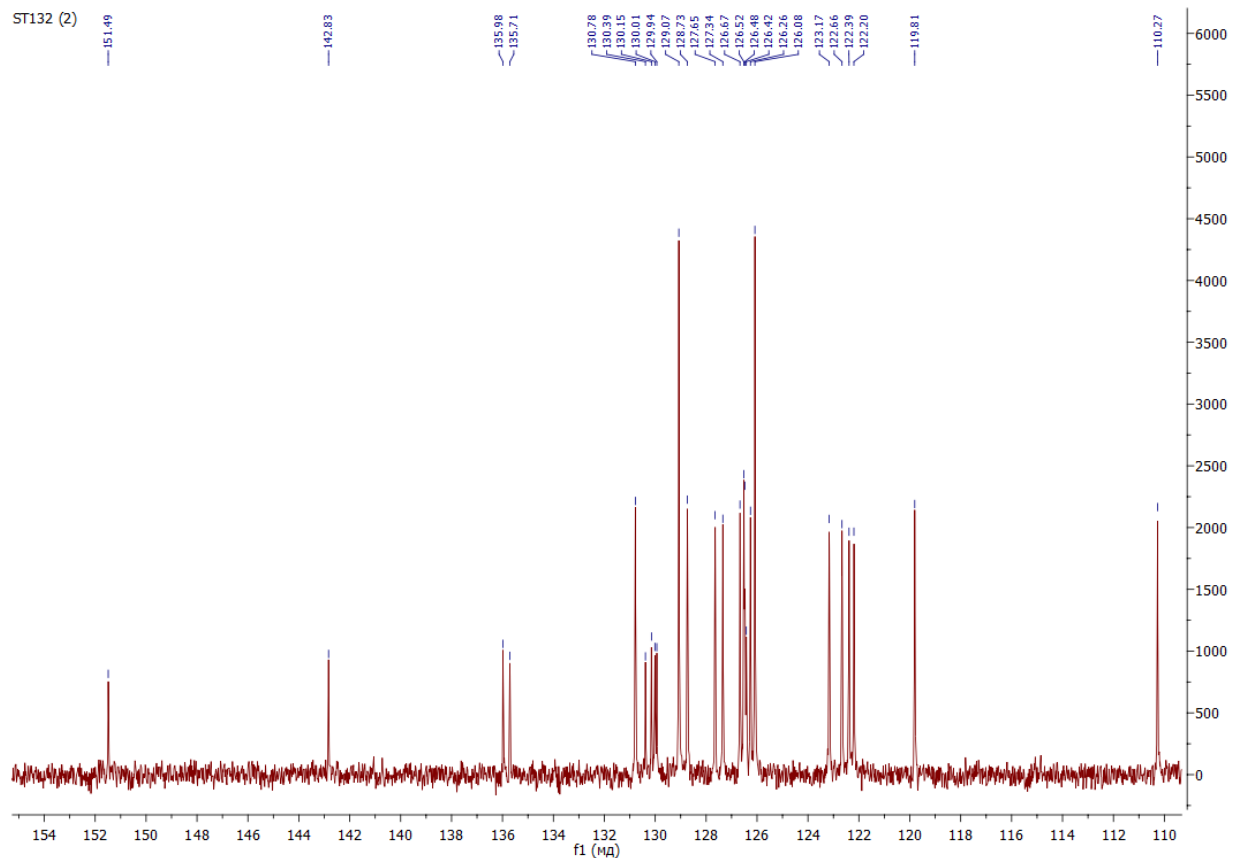


Figure S8. ¹³C {¹H} NMR spectrum of phbi (101 MHz, 298K, CDCl₃).

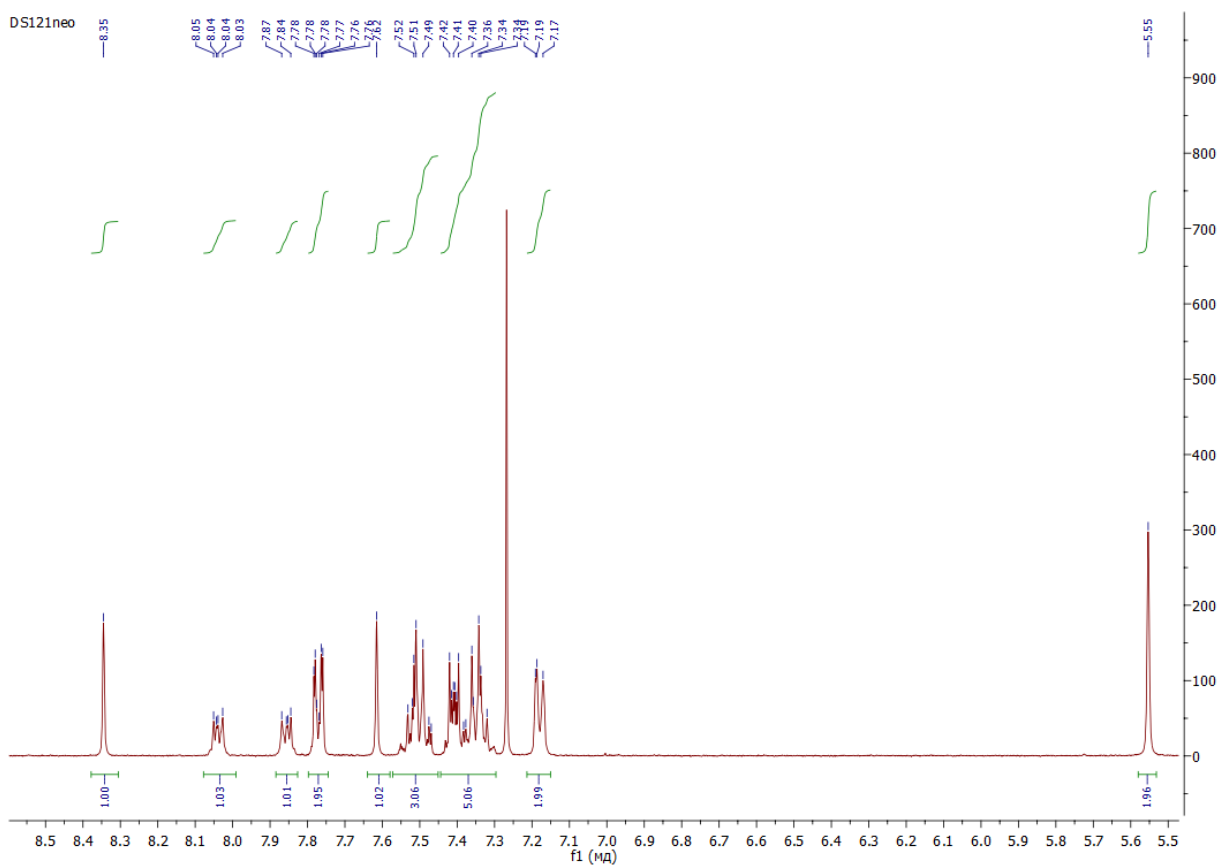


Figure S9. ¹H NMR spectrum of bni (400 MHz, 298K, CDCl₃).

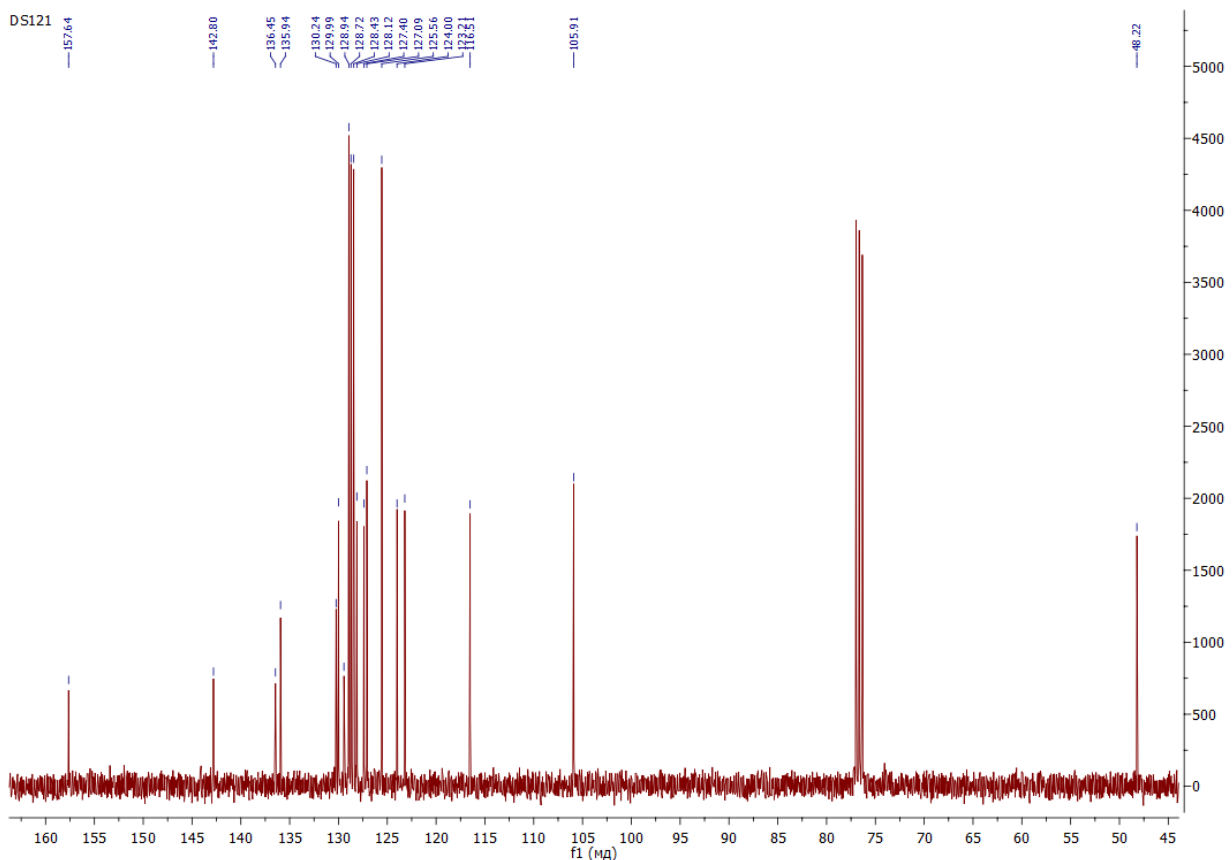


Figure S10. ¹³C {¹H} NMR spectrum of bni (101 MHz, 298K, CDCl₃).

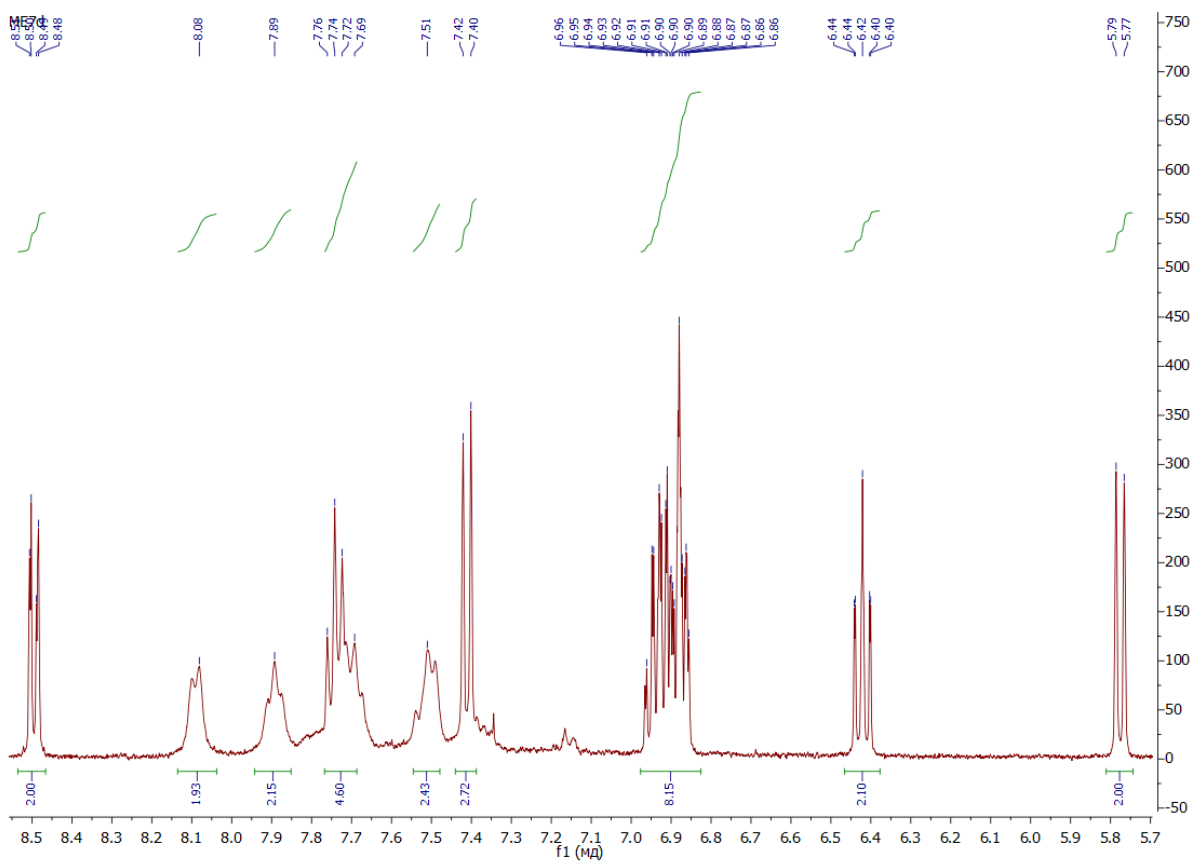


Figure S11. ^1H NMR spectrum of $[\text{Ir}(\text{btbi})_2\text{Cl}]_2$ (400 MHz, 298K, CD_2Cl_2).

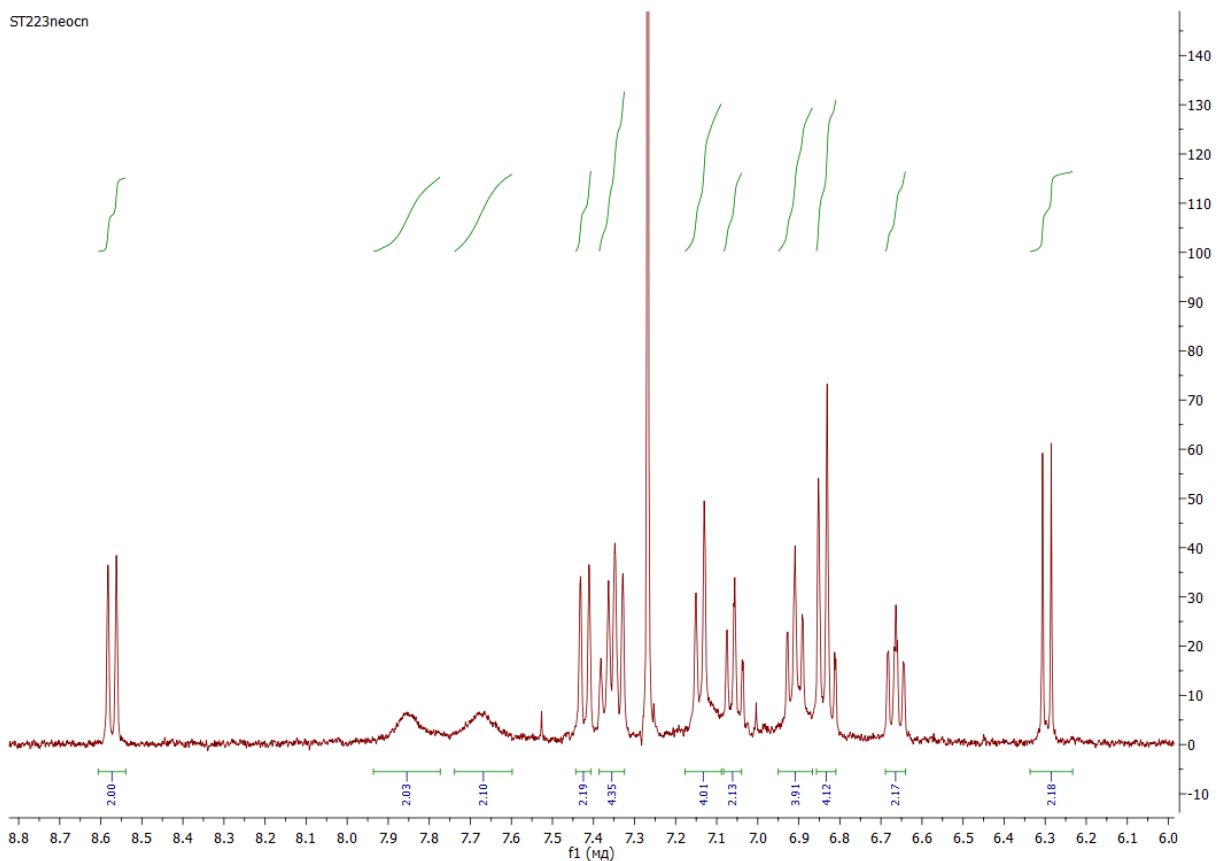


Figure S12. ^1H NMR spectrum of $[\text{Ir}(\text{nbi}-1)_2\text{Cl}]_2$ (400 MHz, 298K, CDCl_3).

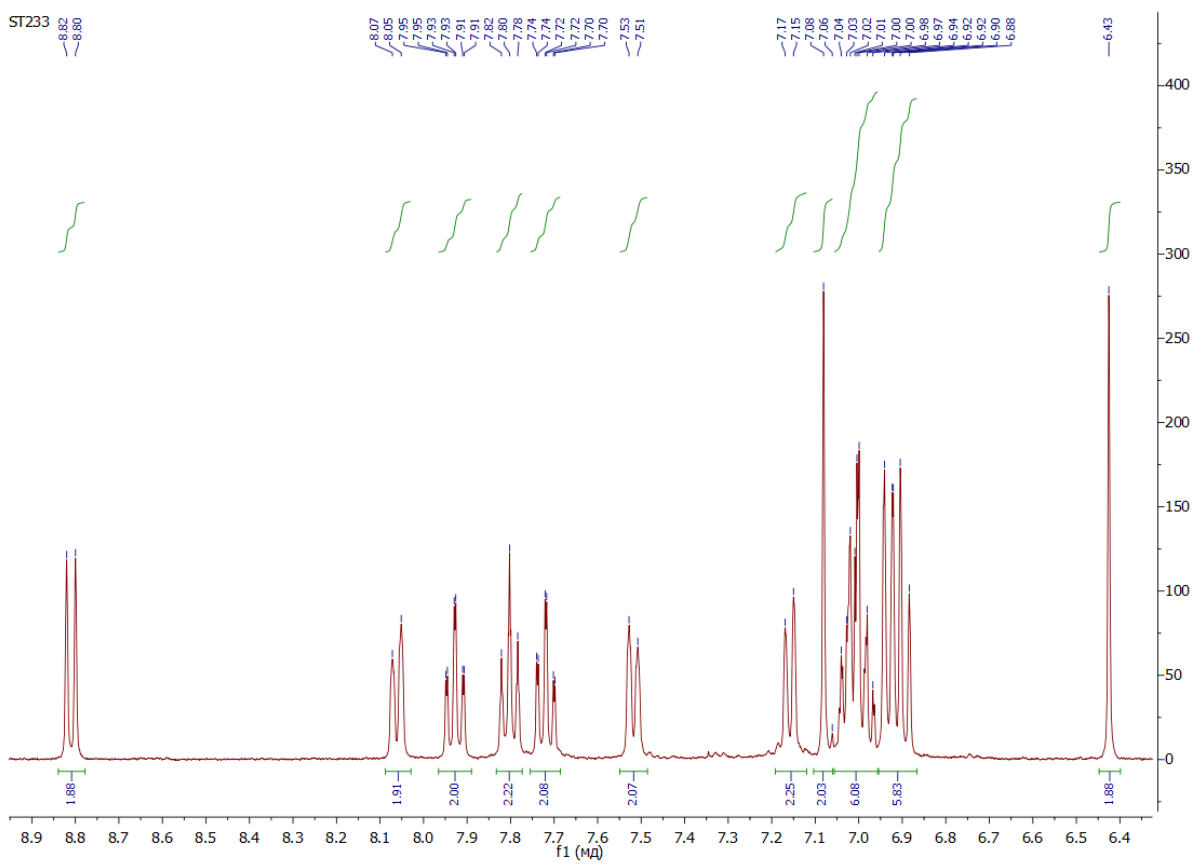


Figure S13. ^1H NMR spectrum of $[\text{Ir}(\text{nbi-2})_2\text{Cl}]_2$ (400 MHz, 298K, CD_2Cl_2).

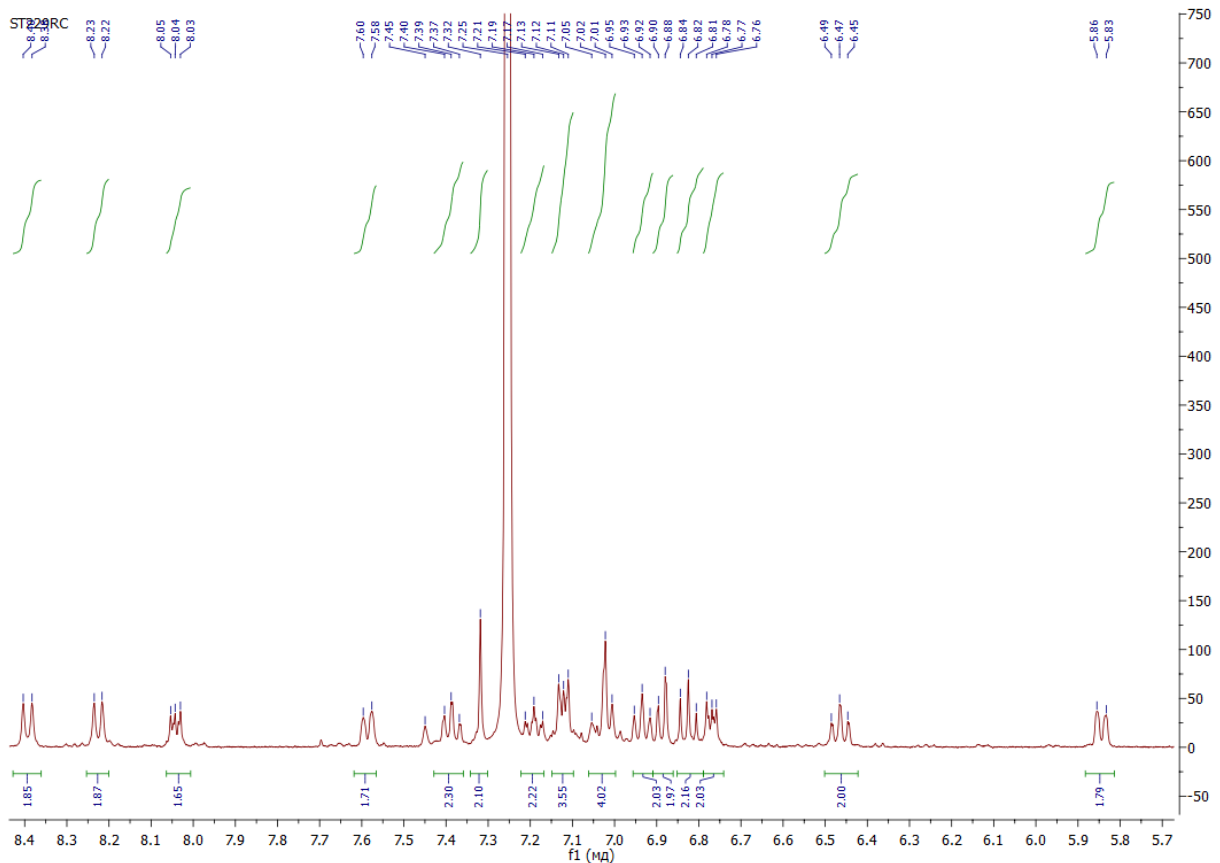


Figure S14. ^1H NMR spectrum of $[\text{Ir}(\text{phbi})_2\text{Cl}]_2$ (400 MHz, 298K, C_6D_6).

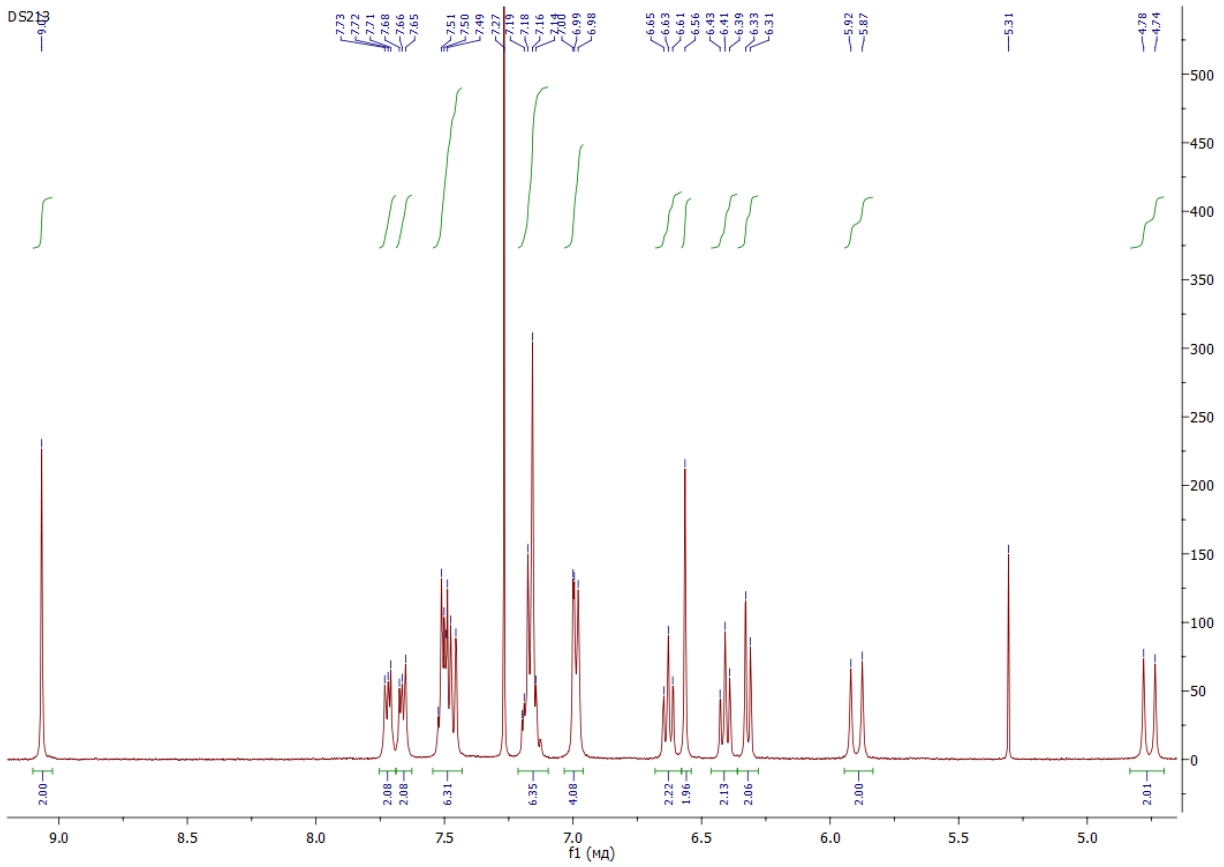


Figure S15. ^1H NMR spectrum of $[\text{Ir}(\text{bni})_2\text{Cl}]_2$ (400 MHz, 298K, CDCl_3).

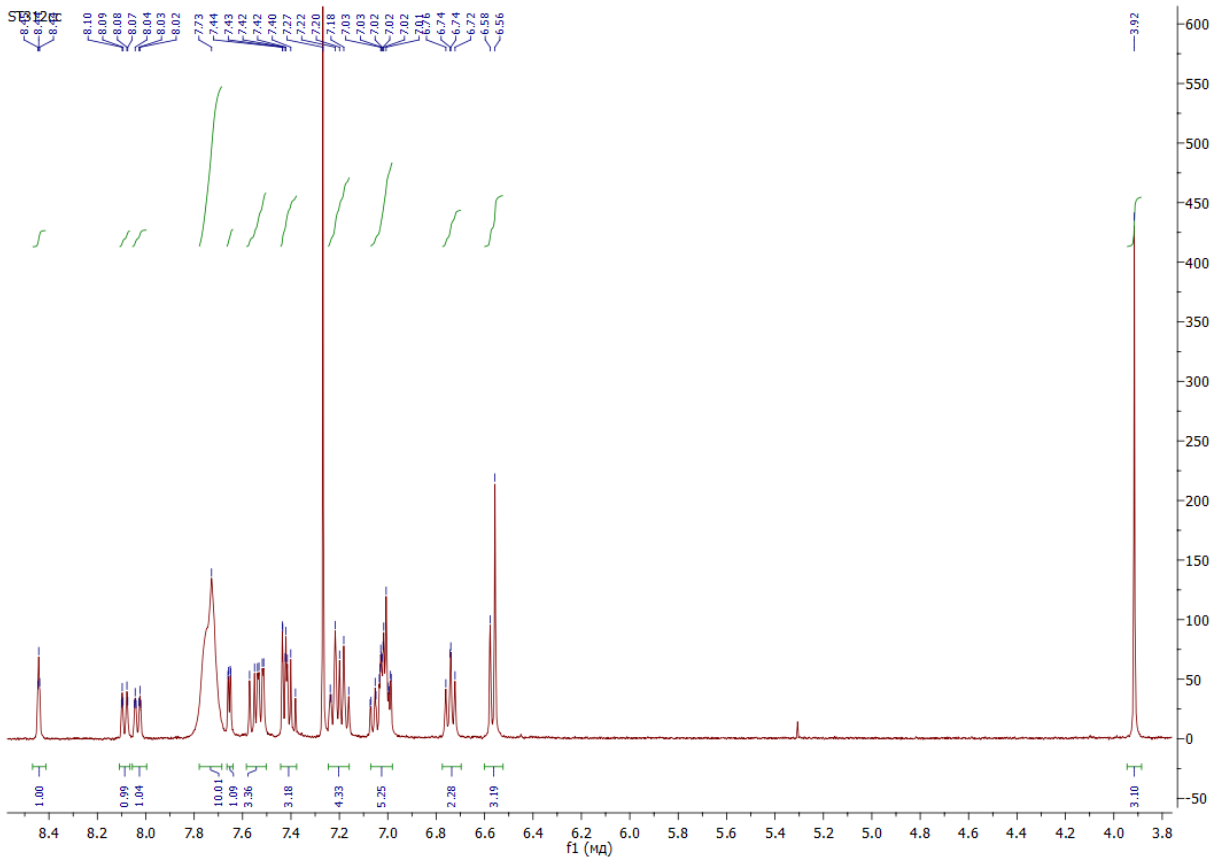


Figure S16. ^1H NMR spectrum of **1** (400 MHz, 298K, CDCl_3).

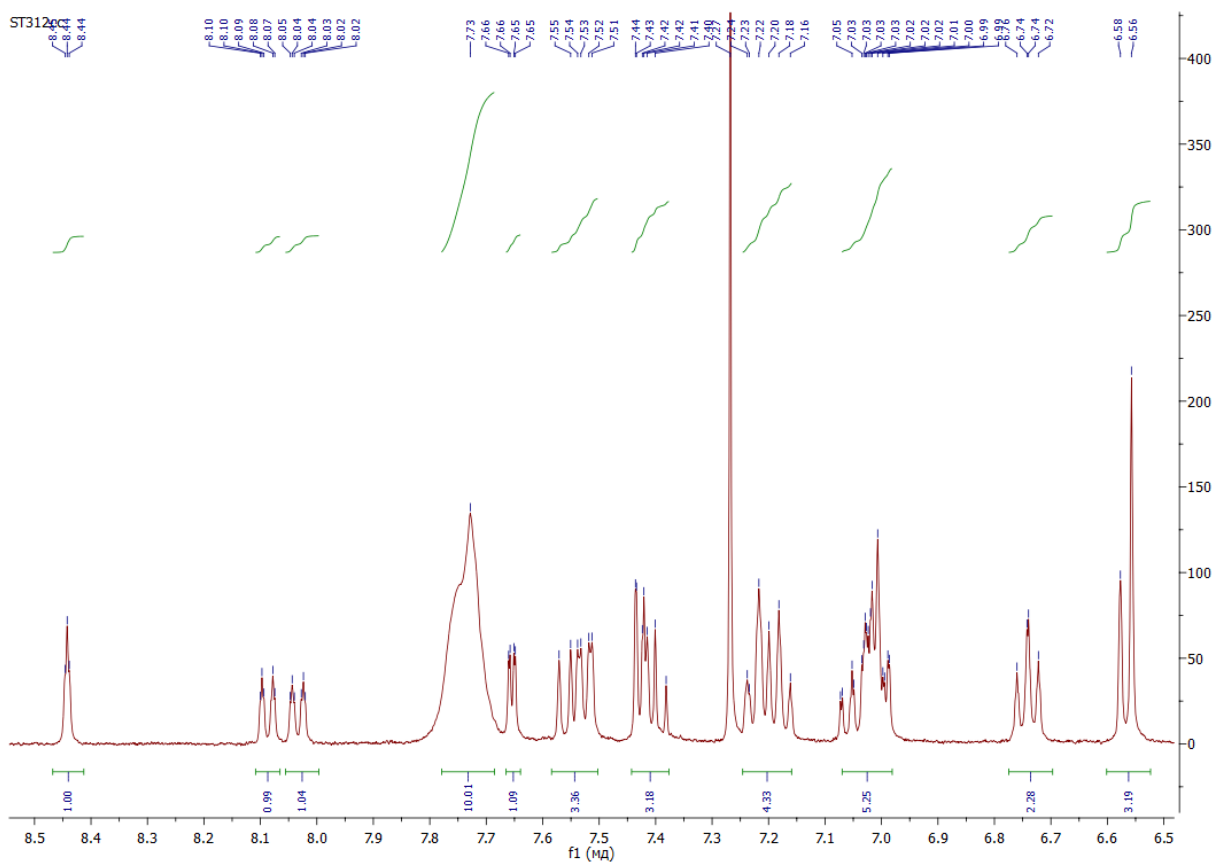


Figure S17. Aromatic region of ^1H NMR spectrum of **1** (400 MHz, 298K, CDCl_3).

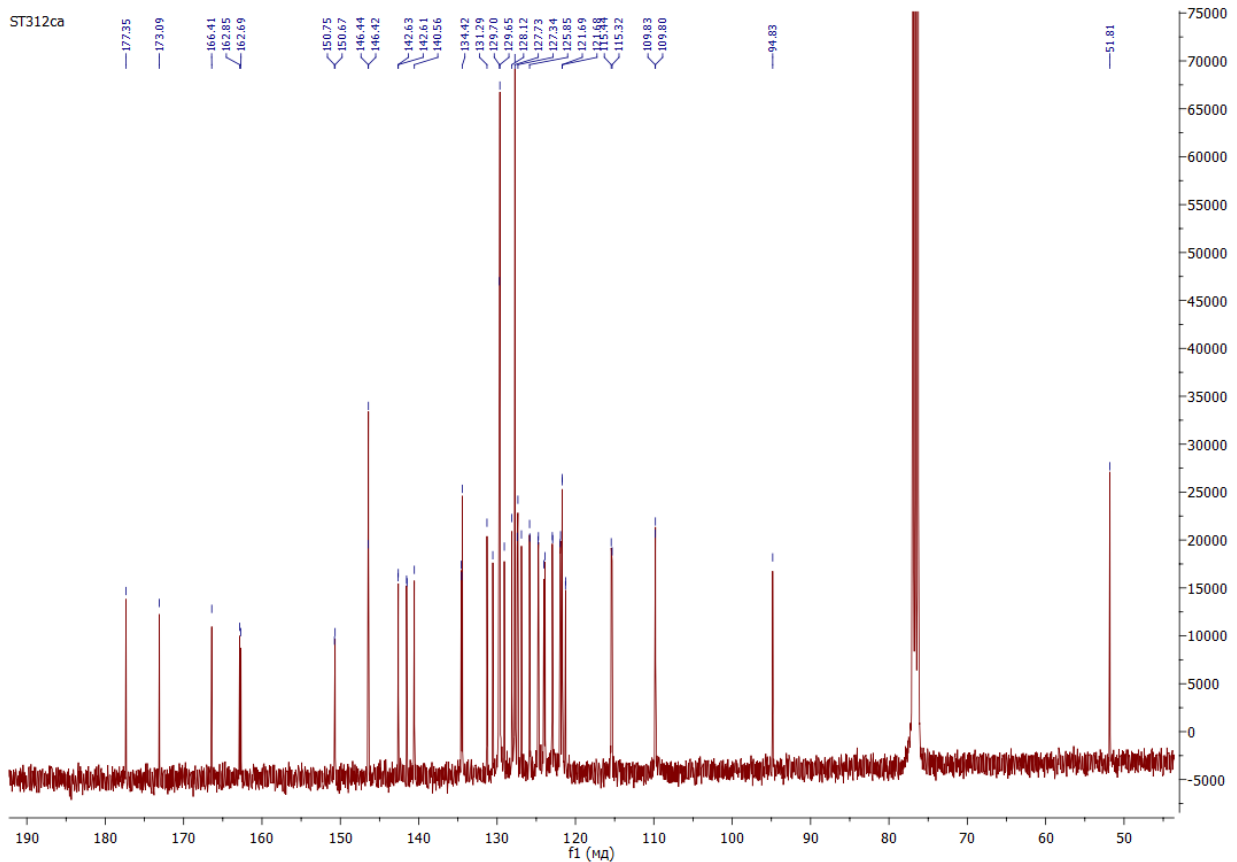


Figure S18. $^{13}\text{C}\{^1\text{H}\}$ NMR spectrum of **1** (101 MHz, 298K, CDCl_3).

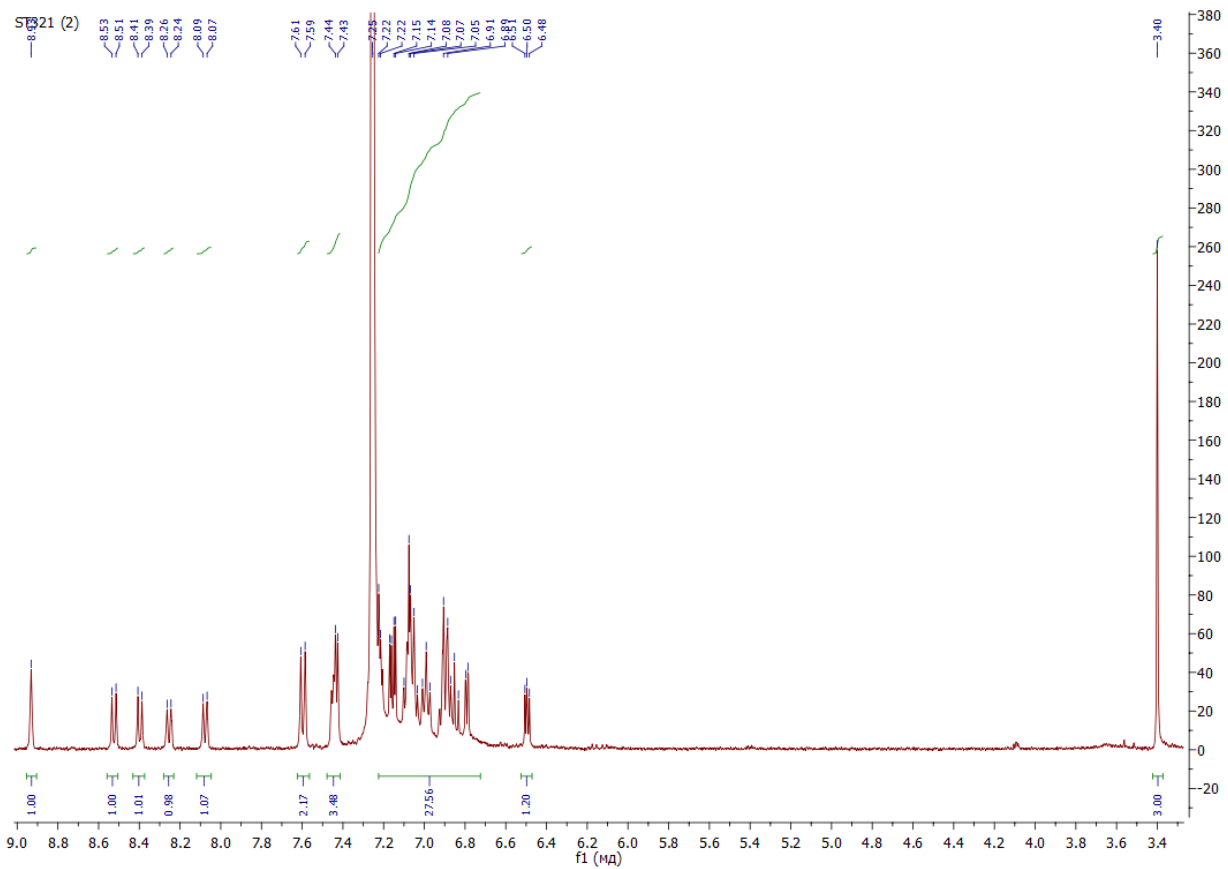


Figure S19. ^1H NMR spectrum of **2** (400 MHz, 298K, C_6D_6).

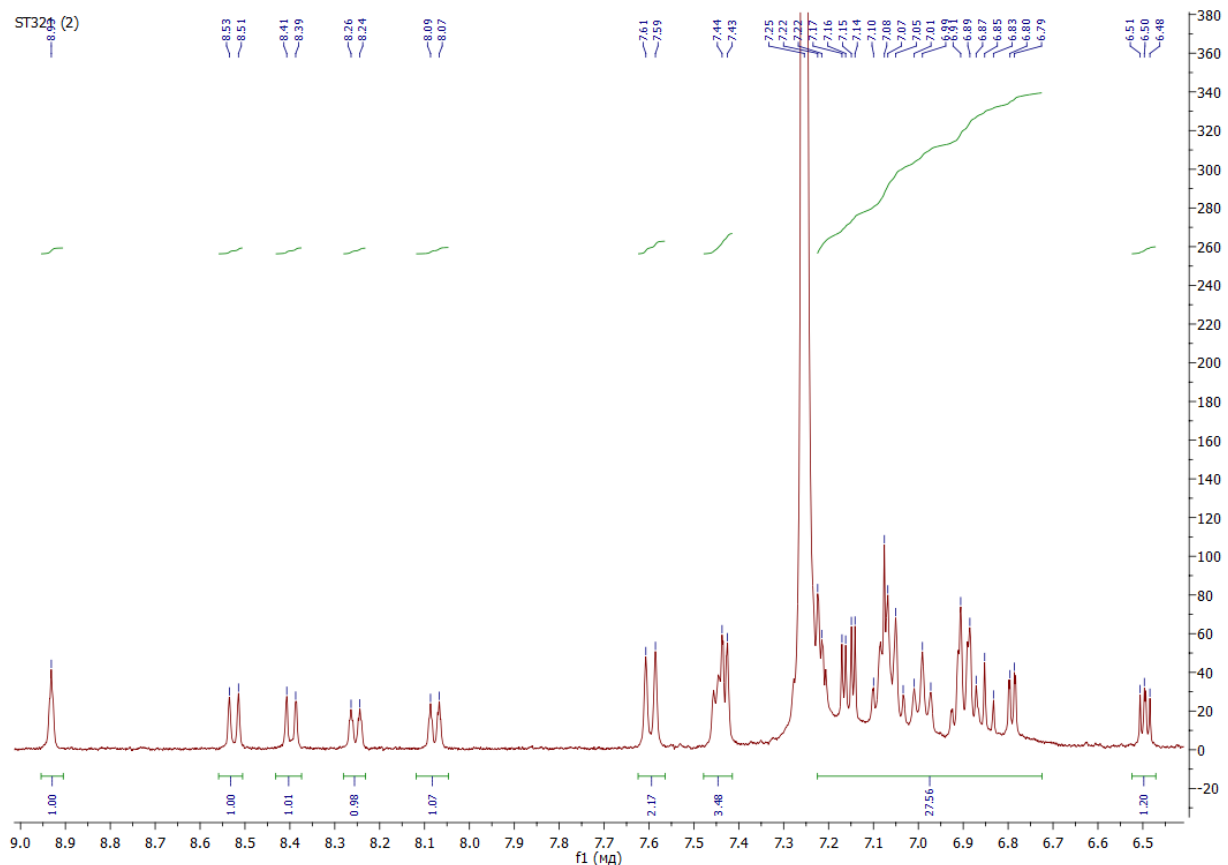


Figure S20. Aromatic region of ^1H NMR spectrum of **2** (400 MHz, 298K, C_6D_6).

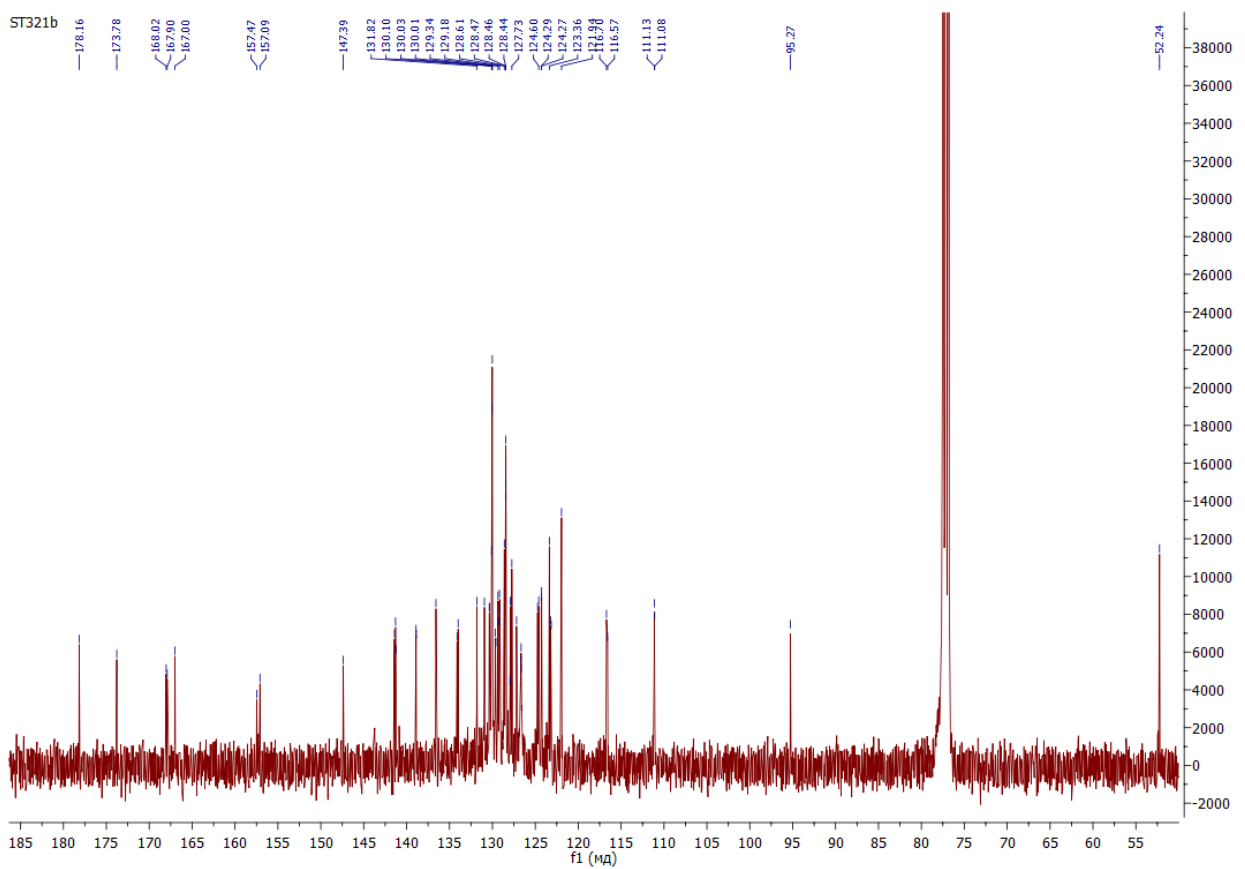


Figure S21. $^{13}\text{C}\{\text{H}\}$ NMR spectrum of **2** (101 MHz, 298K, CDCl_3).

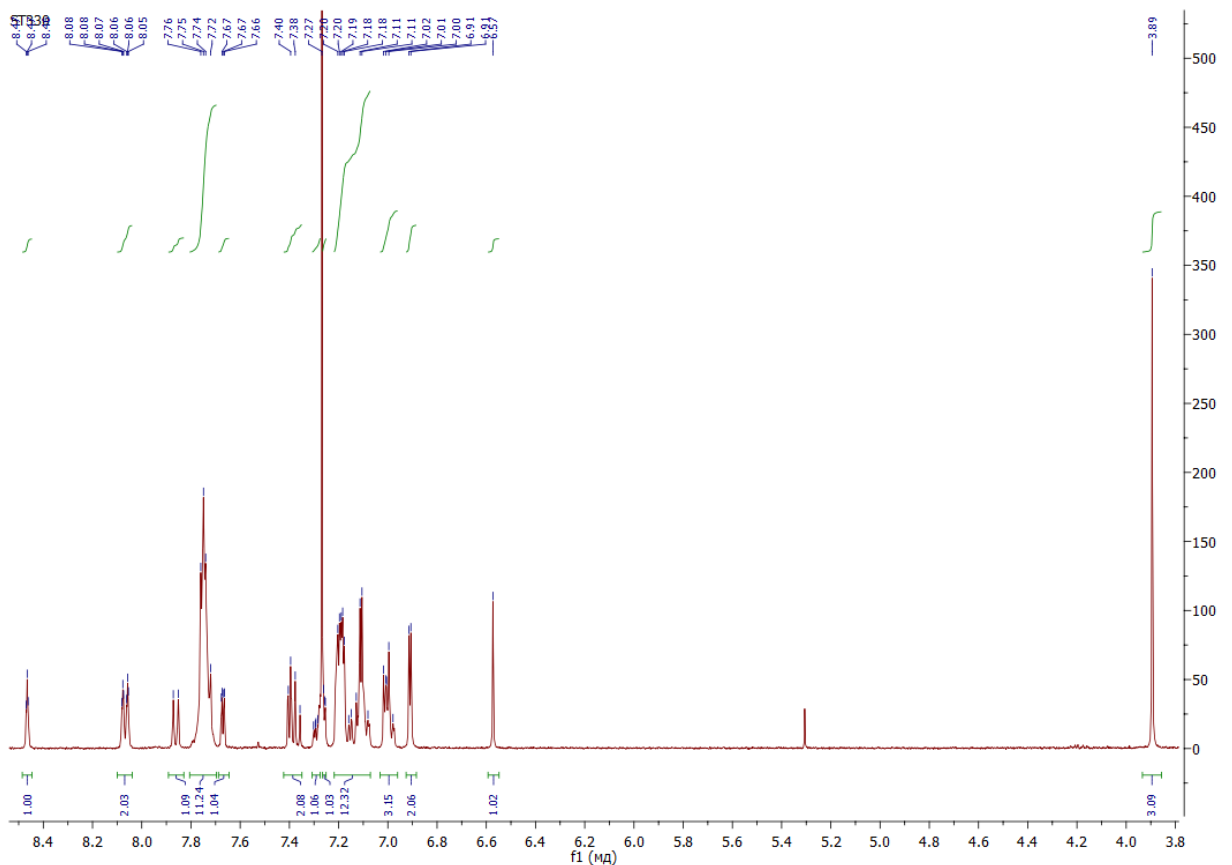


Figure S22. ^1H NMR spectrum of **3** (400 MHz, 298K, CDCl_3).

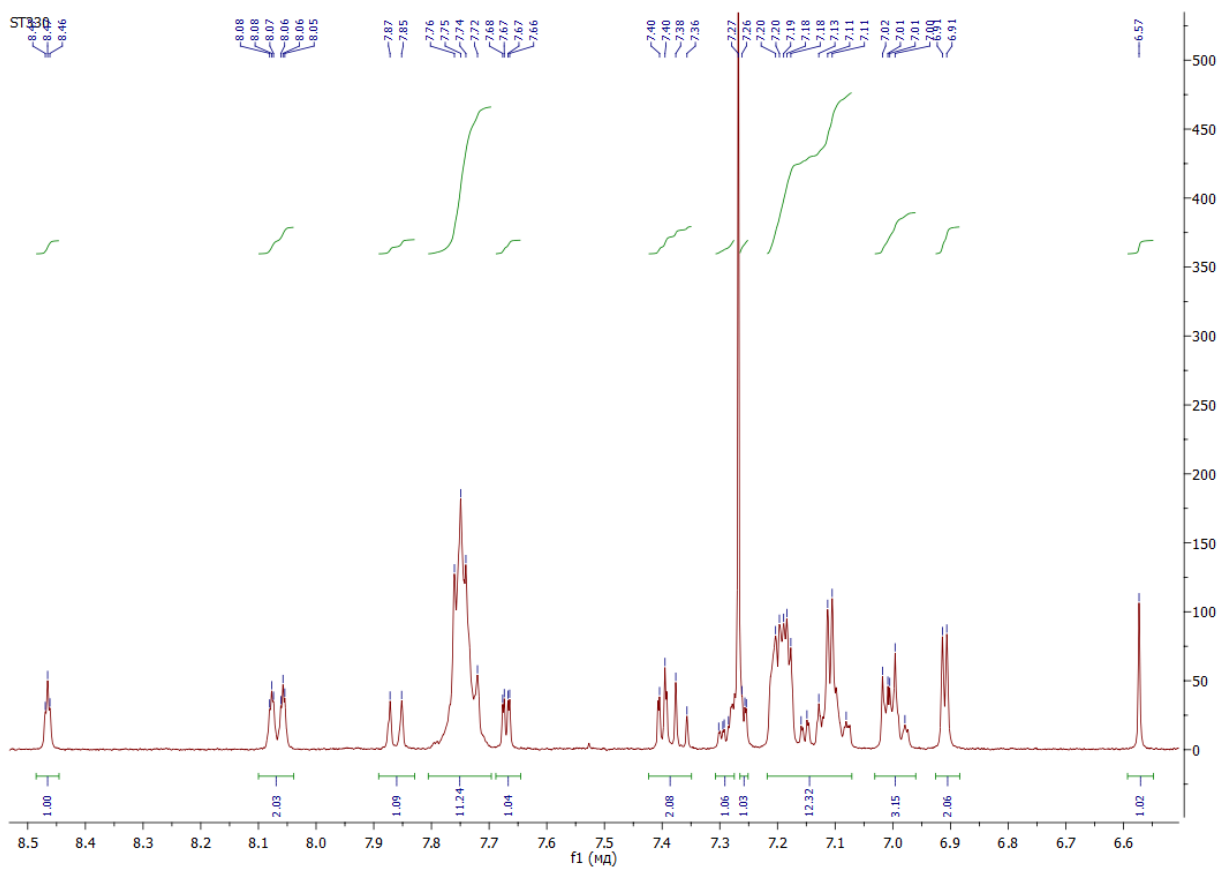


Figure S23. Aromatic region of ^1H NMR spectrum of **3** (400 MHz, 298K, CDCl_3).

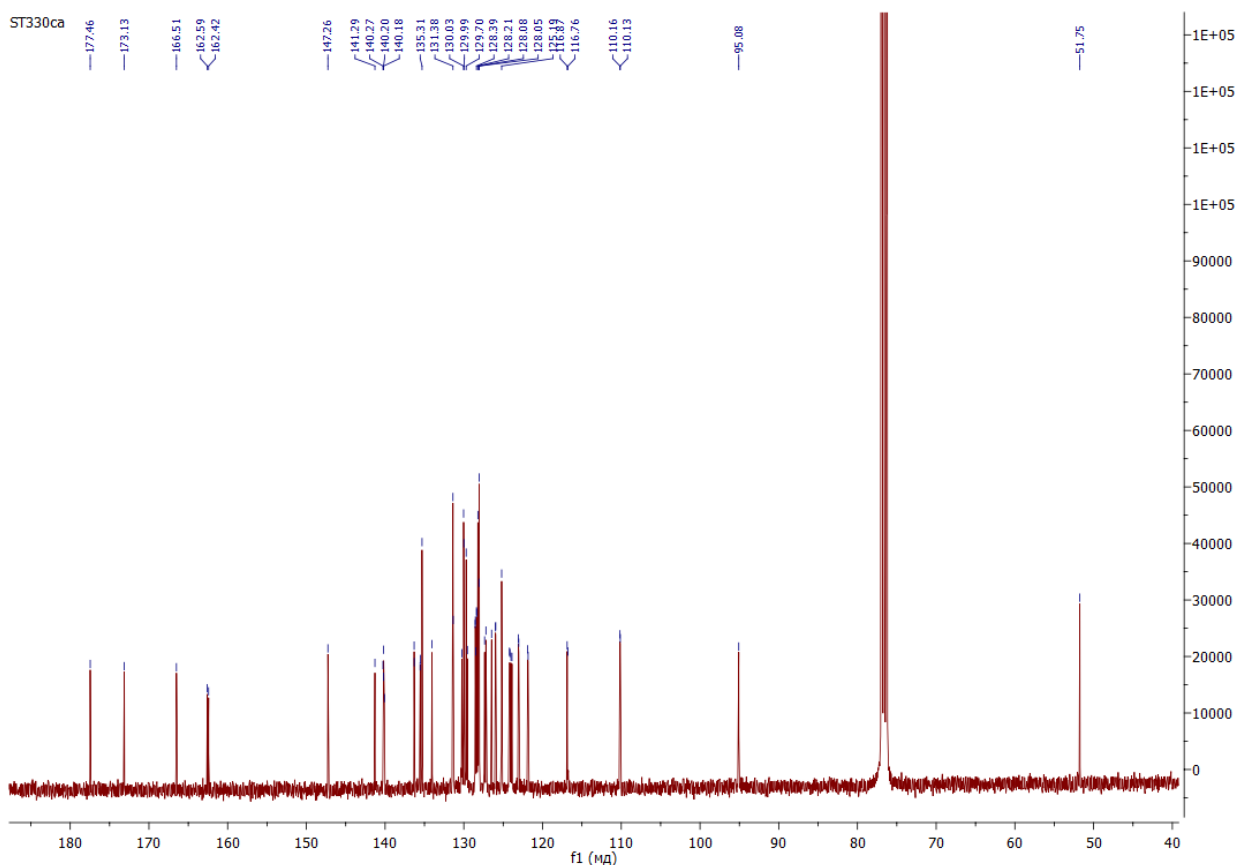


Figure S24. $^{13}\text{C}\{^1\text{H}\}$ NMR spectrum of **3** (101 MHz, 298K, CDCl_3).

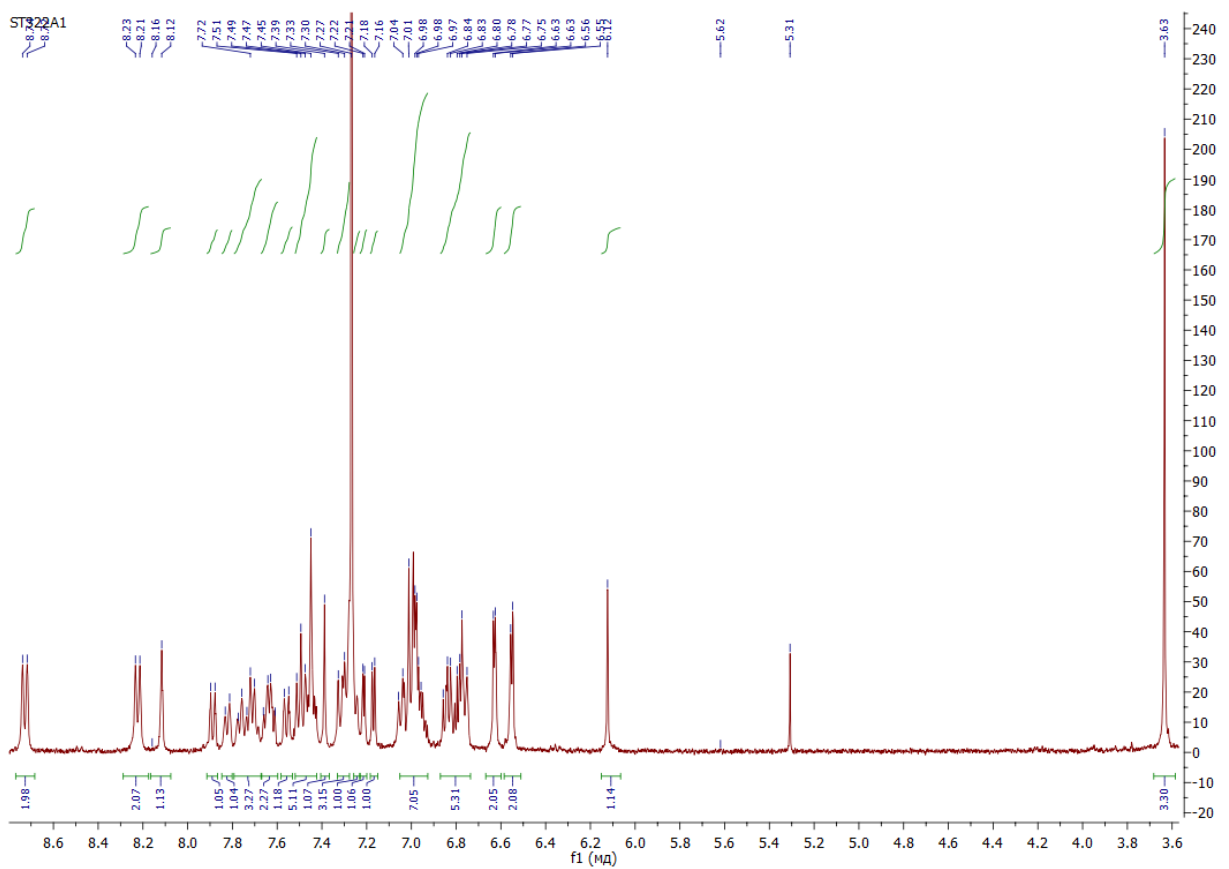


Figure S25. ^1H NMR spectrum of **4** (400 MHz, 298K, CDCl_3).

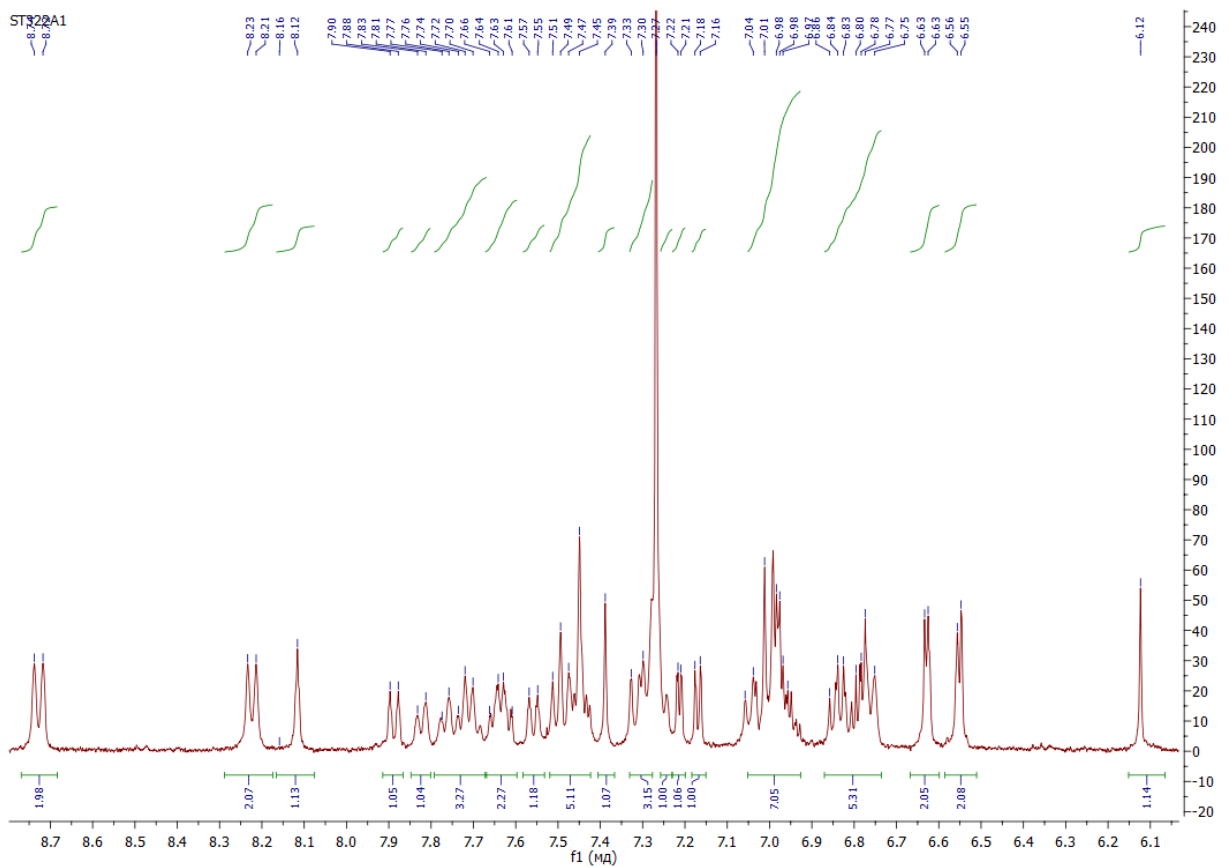


Figure S26. Aromatic region of ^1H NMR spectrum of **4** (400 MHz, 298K, CDCl_3).

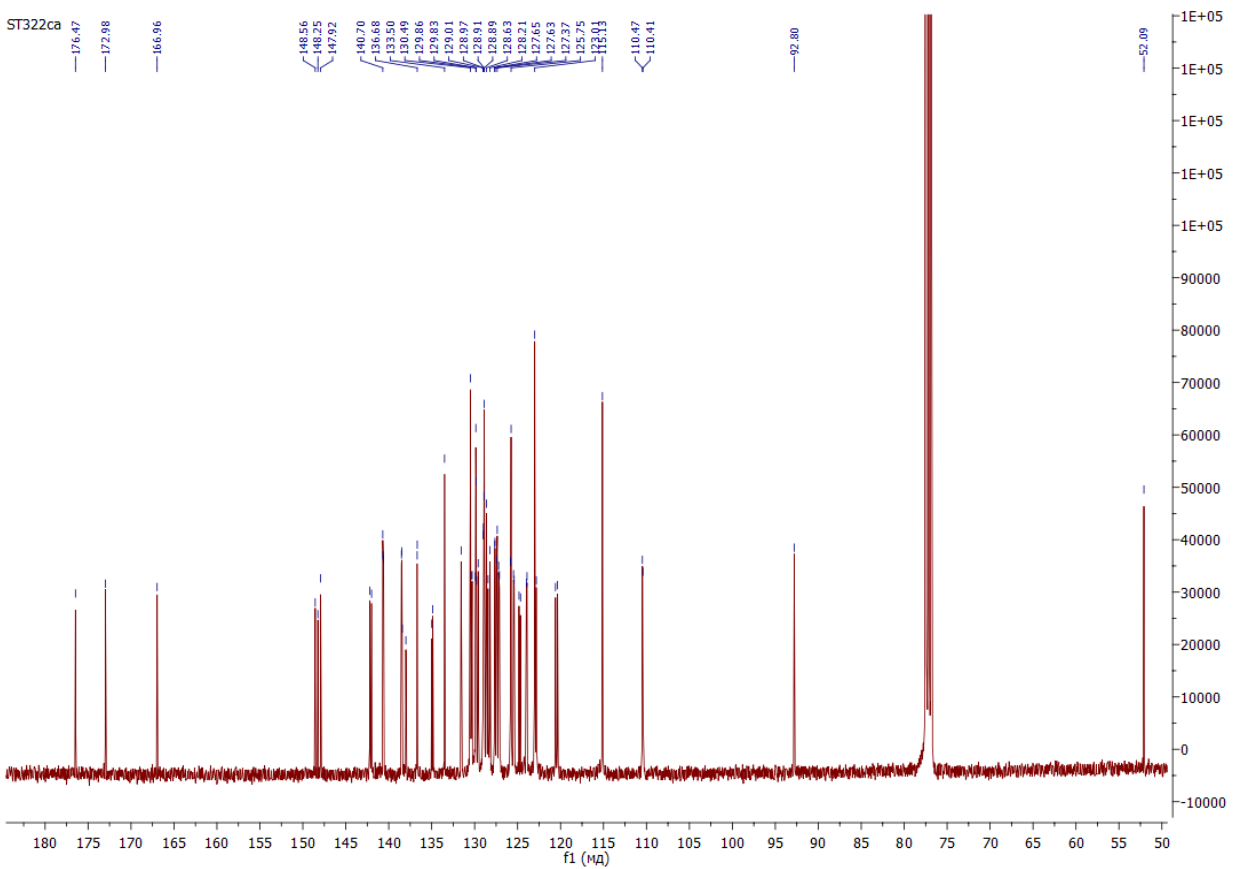


Figure S27. $^{13}\text{C}\{\text{H}\}$ NMR spectrum of **4** (101 MHz, 298K, CDCl_3).

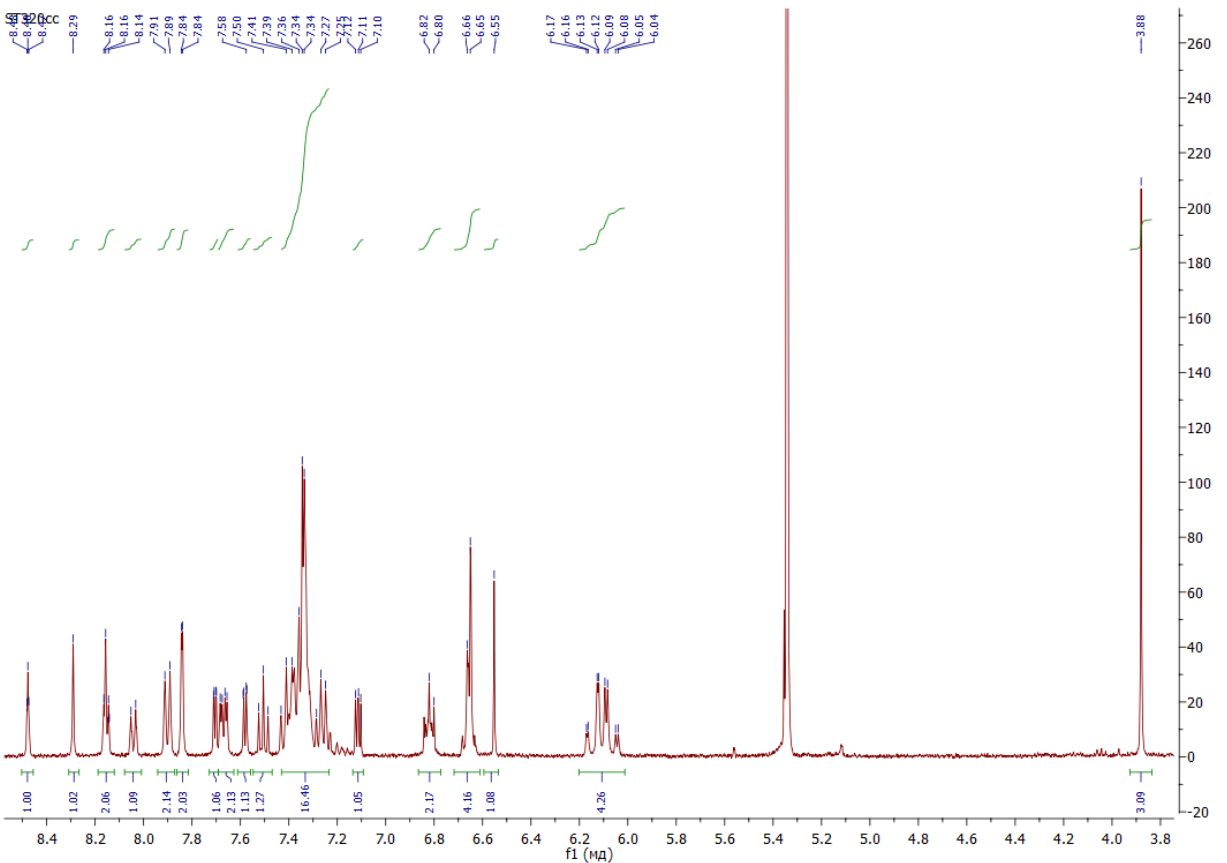


Figure S28. ^1H NMR spectrum of **5** (400 MHz, 298K, CD_2Cl_2).

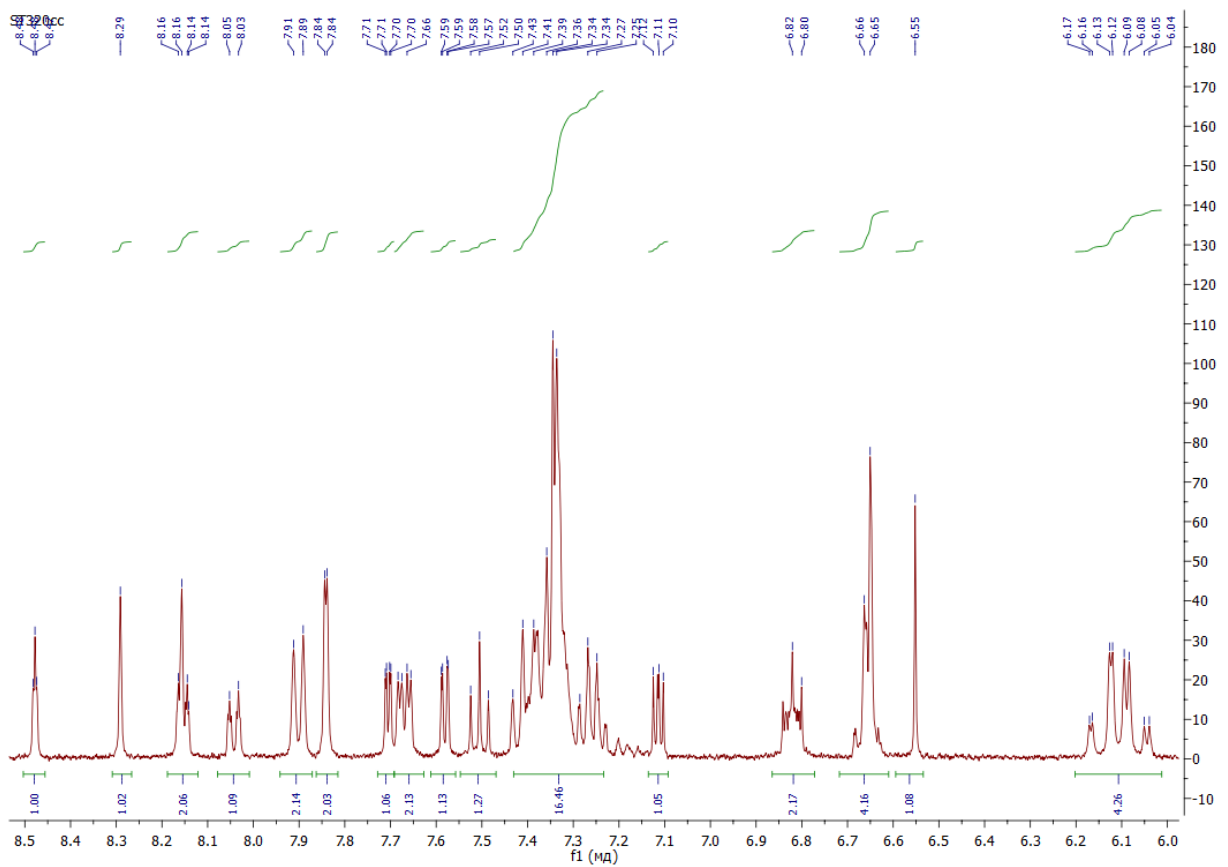


Figure S29. Aromatic region of ^1H NMR spectrum of **5** (400 MHz, 298K, CD_2Cl_2).

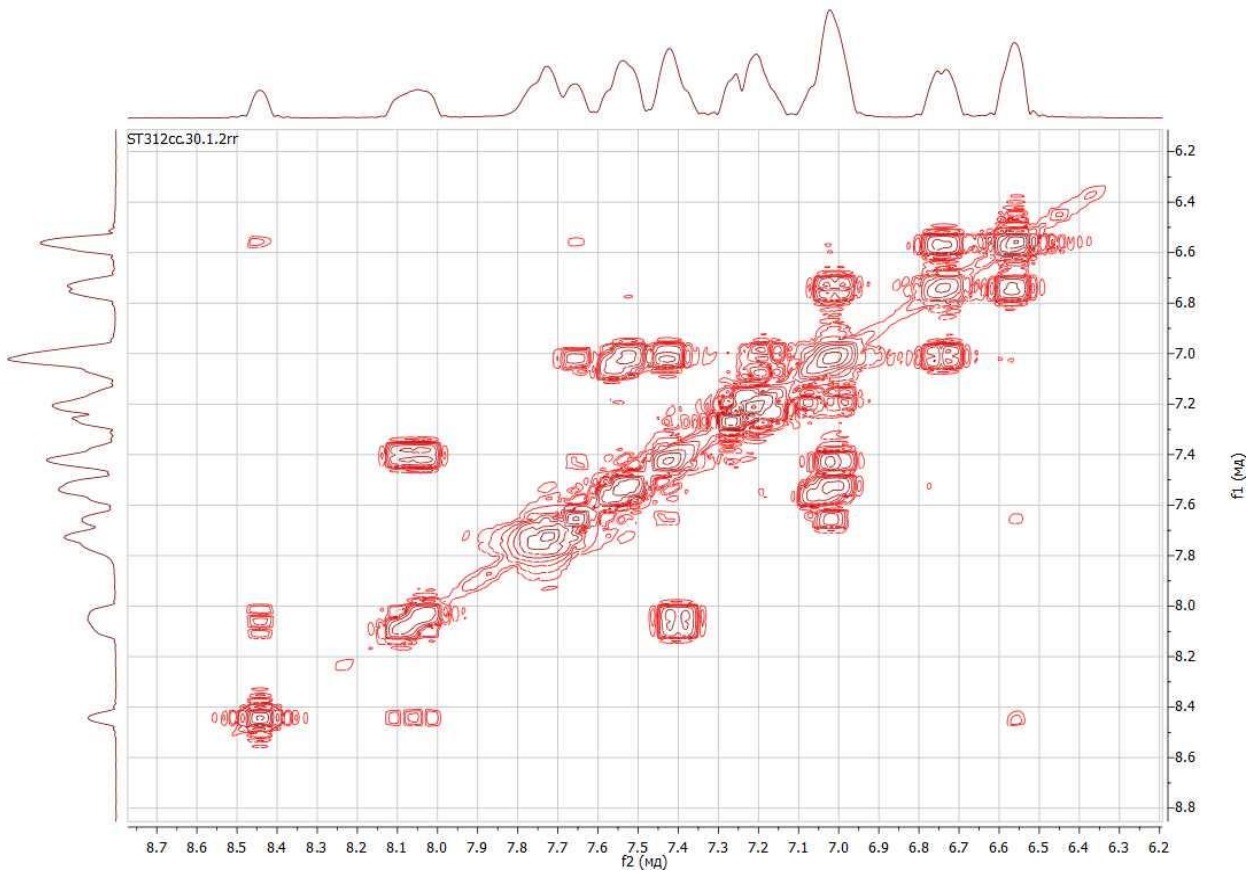
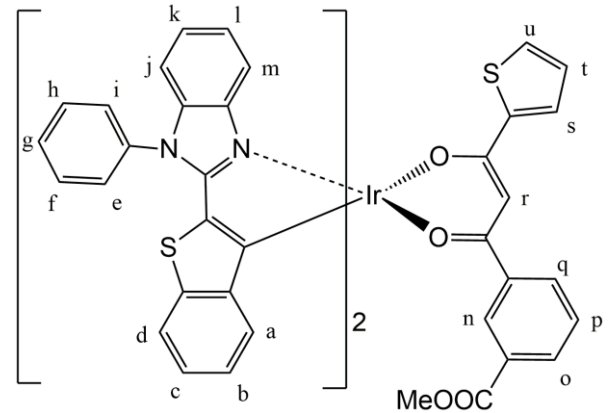


Figure S30. Aromatic region of COSY ^1H , ^1H NMR spectrum of **1**

Assignment:

- 8.44 (t, $J = 1.5$ Hz, 1H)
- 8.09 (dt, $J = 7.7, 1.5$ Hz, 1H)
- 8.06 – 8.00 (m, 1H)
- 7.78 – 7.69 (m, 10H)
signals
- 7.65 (dd, $J = 3.7, 1.0$ Hz, 1H)
- 7.58 – 7.50 (m, 3H)
- 7.44 – 7.38 (m, 3H)
- 7.25 – 7.16 (m, 4H)
- 7.07 – 6.98 (m, 5H)
- 6.77 – 6.70 (m, 2H)
- 6.59 – 6.53 (m, 3H)
- 3.92 (s, 3 H) COOCH_3

n	
q/o	
o/q	
10 residual	
s	
m,d,d'	
u,p,m'	
k,k',j,j'	
l,l',t,c,c'	
b,b'	
a,a',r	



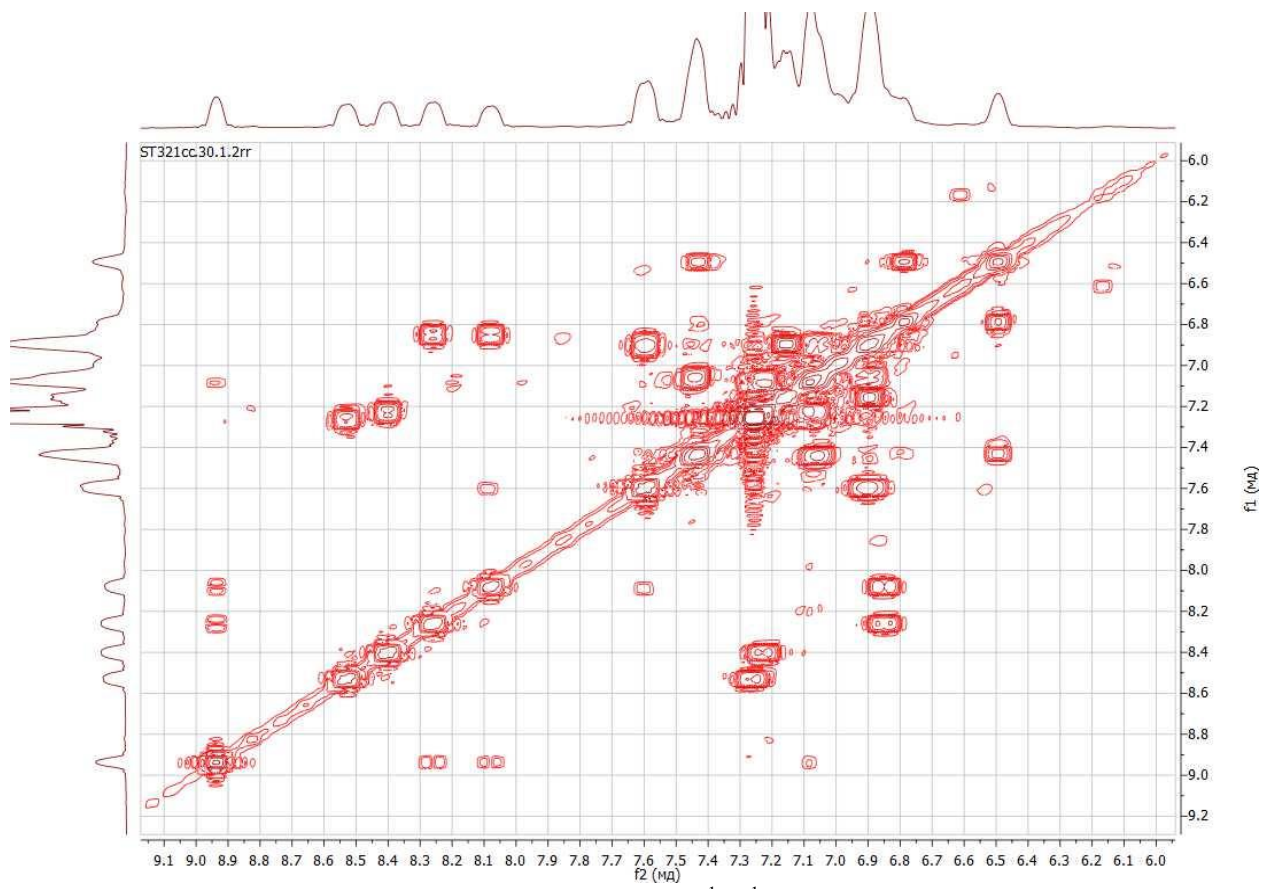
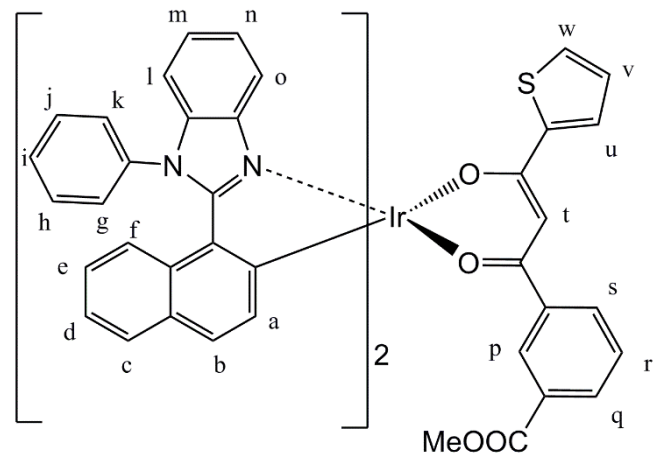


Figure S31. Aromatic region of COSY ^1H , ^1H NMR spectrum of **2**

Assignment:

- 8.93 (t, $J = 1.4$ Hz, 1H)
- 8.52 (d, $J = 8.1$ Hz, 1H)
- 8.43 – 8.37 (m, 1H)
- 8.25 (dt, $J = 7.8, 1.5$ Hz, 1H)
- 8.08 (dt, $J = 7.7, 1.4$ Hz, 1H)
- 7.60 (d, $J = 8.5$ Hz, 2H)
- 7.48 – 7.41 (m, 3H)
- residual signal**
- 7.22 – 6.72 (m, 27H)
- signals**
- 6.52 – 6.48 (m, 1H)
- 3.40 (s, 3H)

p	o/o'
o'/o	o'/o
q/s	q/s
s/q	s/q
u/s	u/s
w/u,	$\text{w}/\text{u},$
residual	
v	COOCH_3



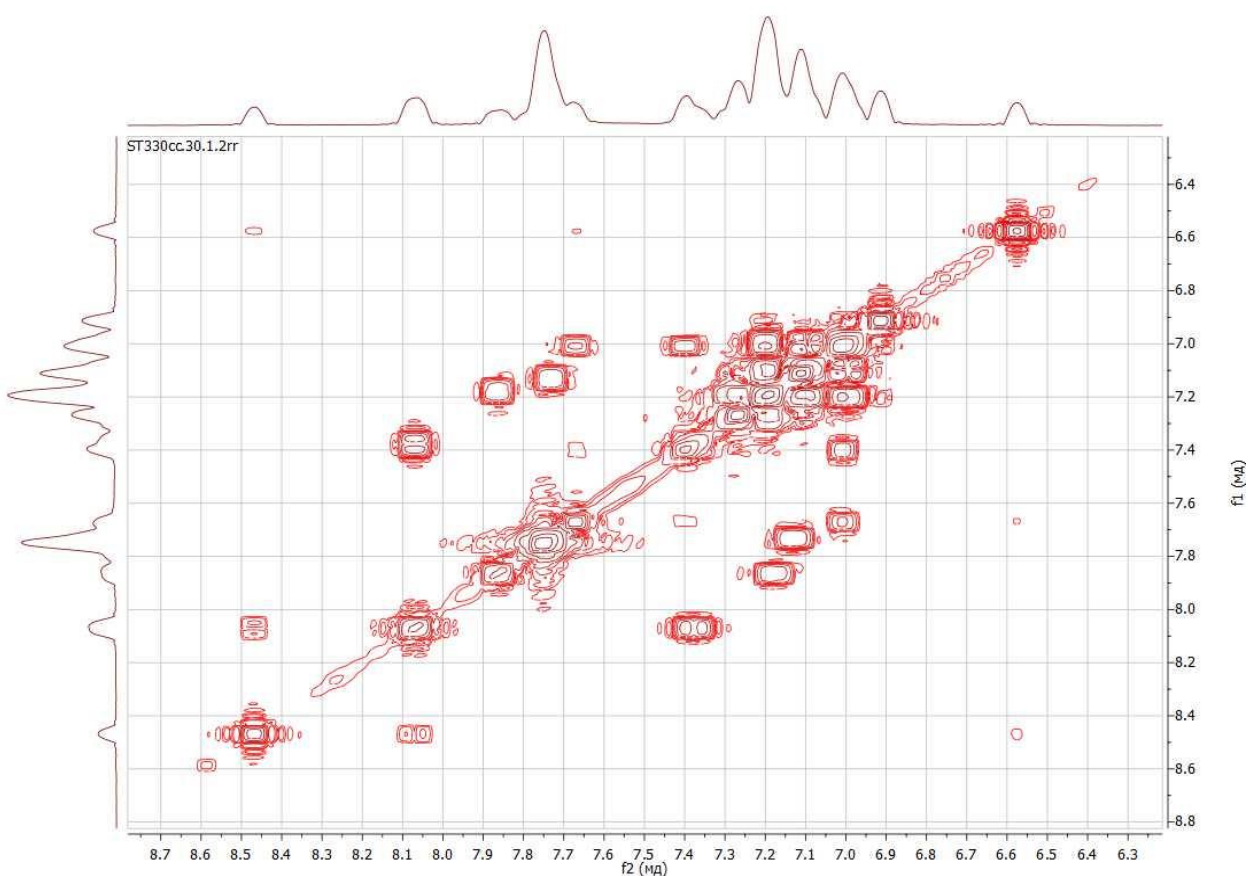
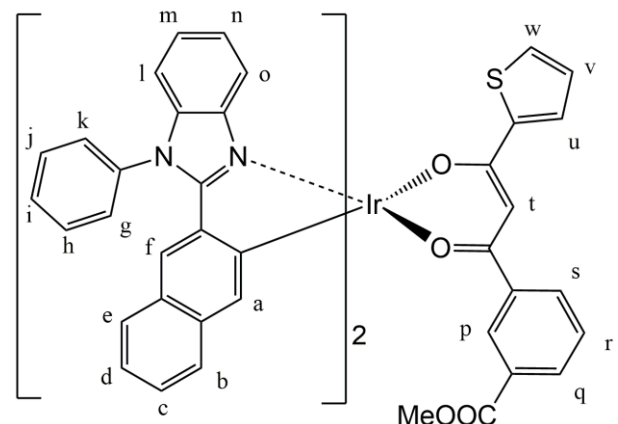


Figure S32. Aromatic region of COSY ^1H , ^1H NMR spectrum of **3**

Assignment:

8.47 (t, $J = 1.6$ Hz, 1H)
 8.10 – 8.04 (m, 2H)
 7.88 – 7.84 (m, 1H),
 7.81 – 7.70 (m, 11H)
 7.67 (dd, $J = 3.7, 1.1$ Hz, 1H)
 7.42 – 7.35 (m, 2H)
 7.31 – 7.27 (m, 1H)
 7.27 – 7.24 (m, 1H),
 7.22 – 7.07 (m, 12H),
 f,f',m,m',d,d',n,n',e,e',b,b'
 7.03 – 6.96 (m, 3H)
 6.93 – 6.88 (m, 2H),
 6.57 (s, 1H)
 3.89 (s, 3 H) COOCH_3

p
q,s
o
g-k,g'-k',o'
u/w
w/u,r
l
l'
c, c'v
a,a'
t



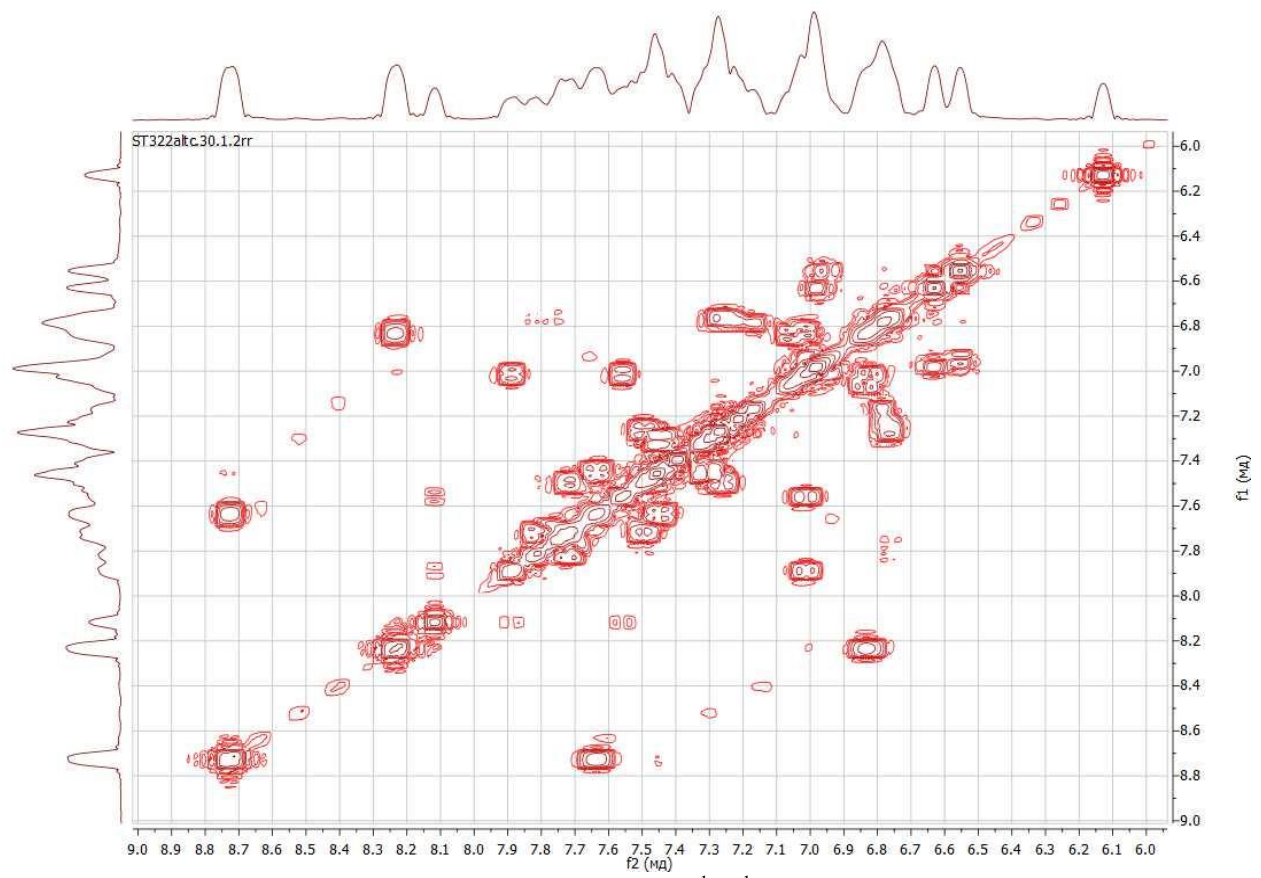


Figure S33. Aromatic region of COSY ^1H , ^1H NMR spectrum of **4**

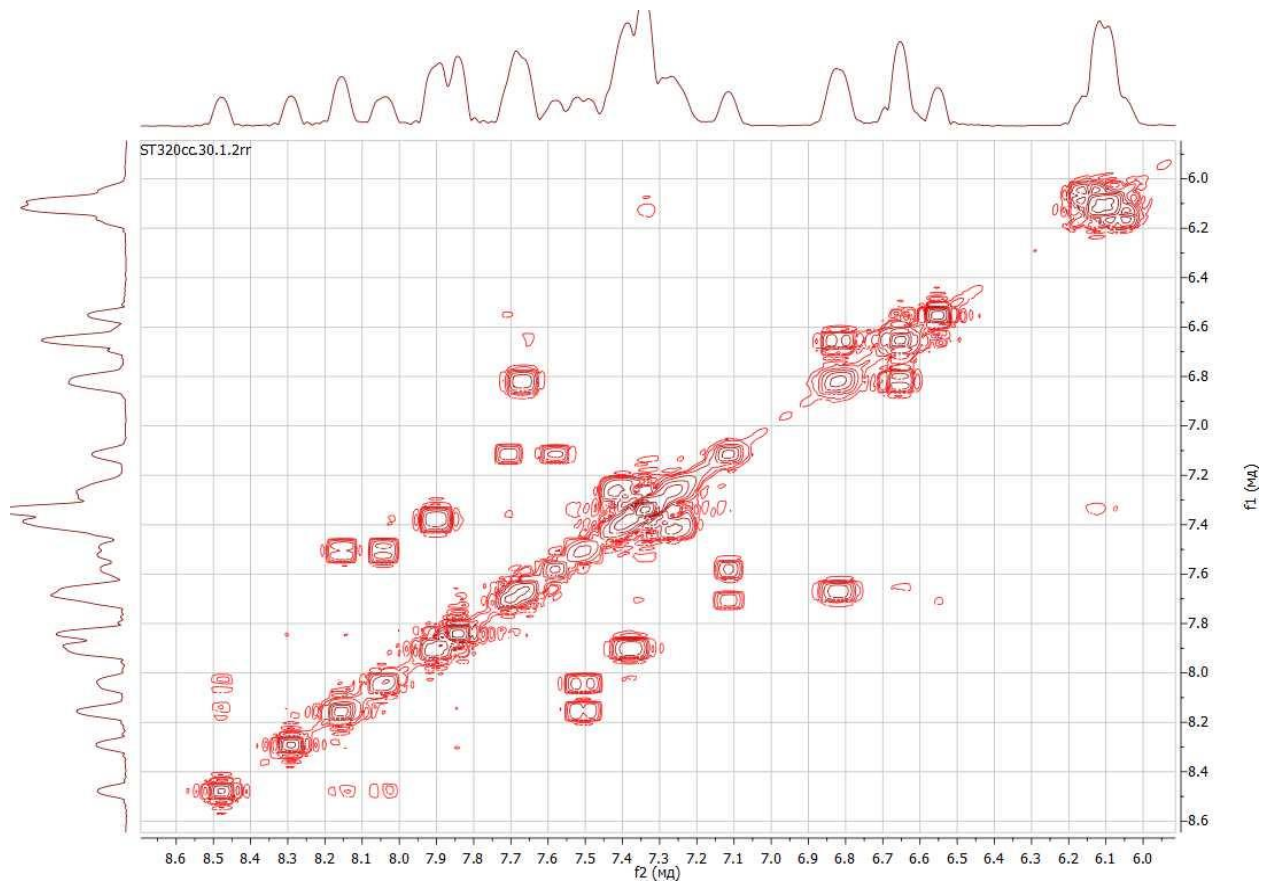


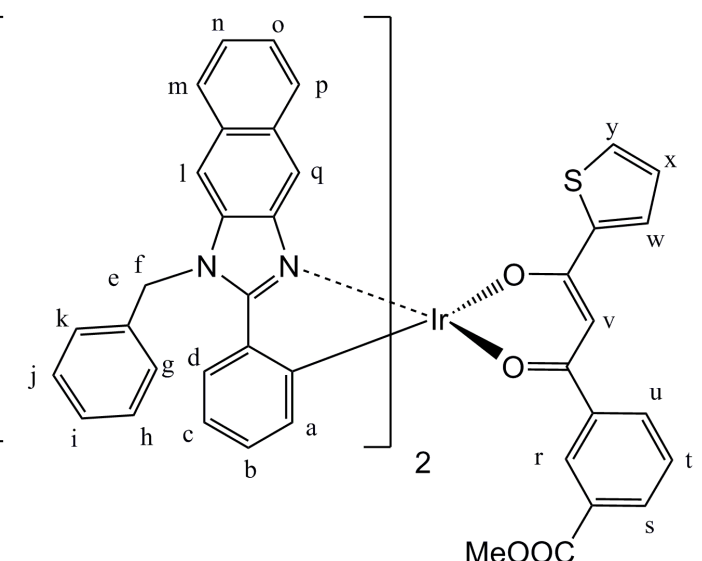
Figure S34. Aromatic region of COSY ^1H , ^1H NMR spectrum of **5**

Assignment:

- 8.48 (t, $J = 1.6$ Hz, 1H)
- 8.29 (s, 1H)
- 8.19 – 8.12 (m, 2H)
- 7.90 (d, $J = 8.4$ Hz, 2H)
- residual signal**
- 7.86 – 7.82 (m, 2H)
- 7.71 (dd, $J = 3.8, 1.1$ Hz, 1H)
- 7.69 – 7.63 (m, 2H)
- 7.58 (dd, $J = 5.0, 1.1$ Hz, 1H)
- 7.51 (t, $J = 7.8$ Hz, 1H)
- 7.36 (d, $J = 4.8$ Hz, 1 H)
- 7.45 – 7.22 (m, 16H); **16 residual signals**
- 7.11 (dd, $J = 5.0, 3.8$ Hz, 1H)
- 6.86 – 6.77 (m, 2H)
- 6.72 – 6.61 (m, 4H)
- a,a',b,b'**
- 6.55 (s, 1H)
- 6.20 – 6.01 (m, 4H)
- 3.88 (s, 3H) COOCH_3

r
q
q';s/u
a
l,l'
w/y
d,d'
y/w
t
w/y
x
c,c'

v
e,e',f,f'



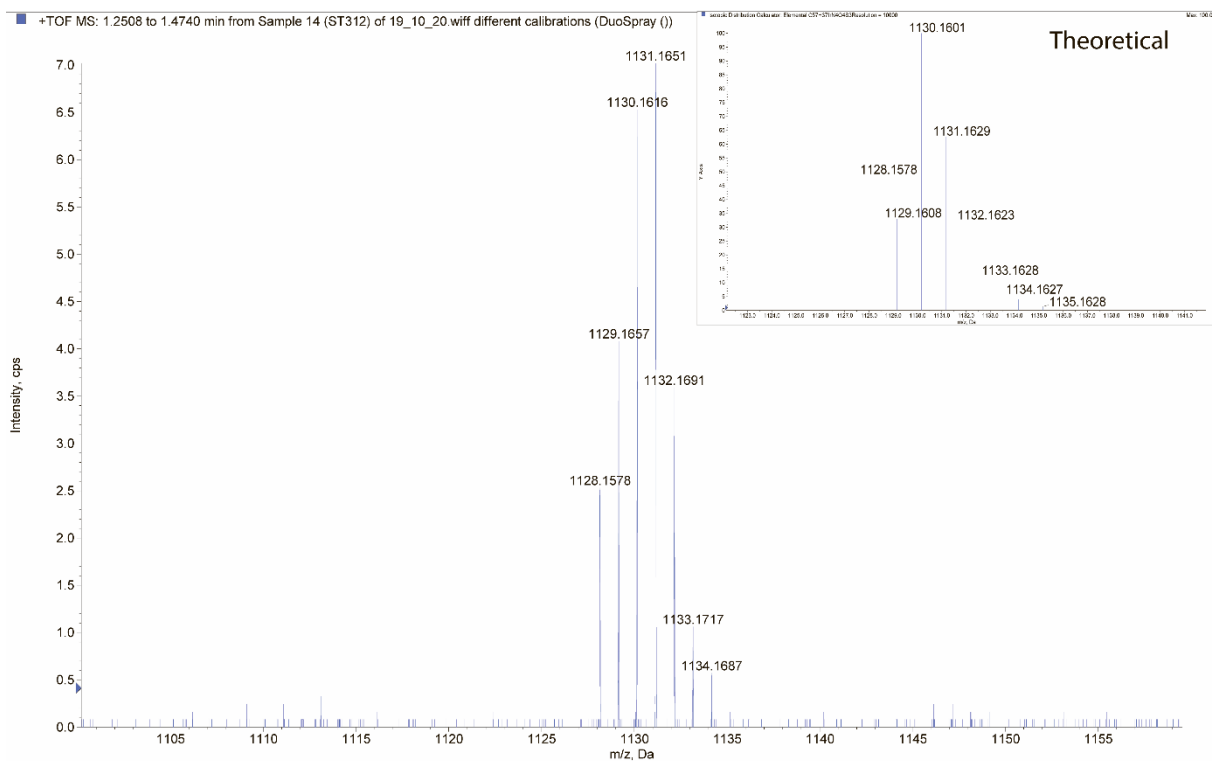


Figure S35. High resolution mass spectrum of **1**.

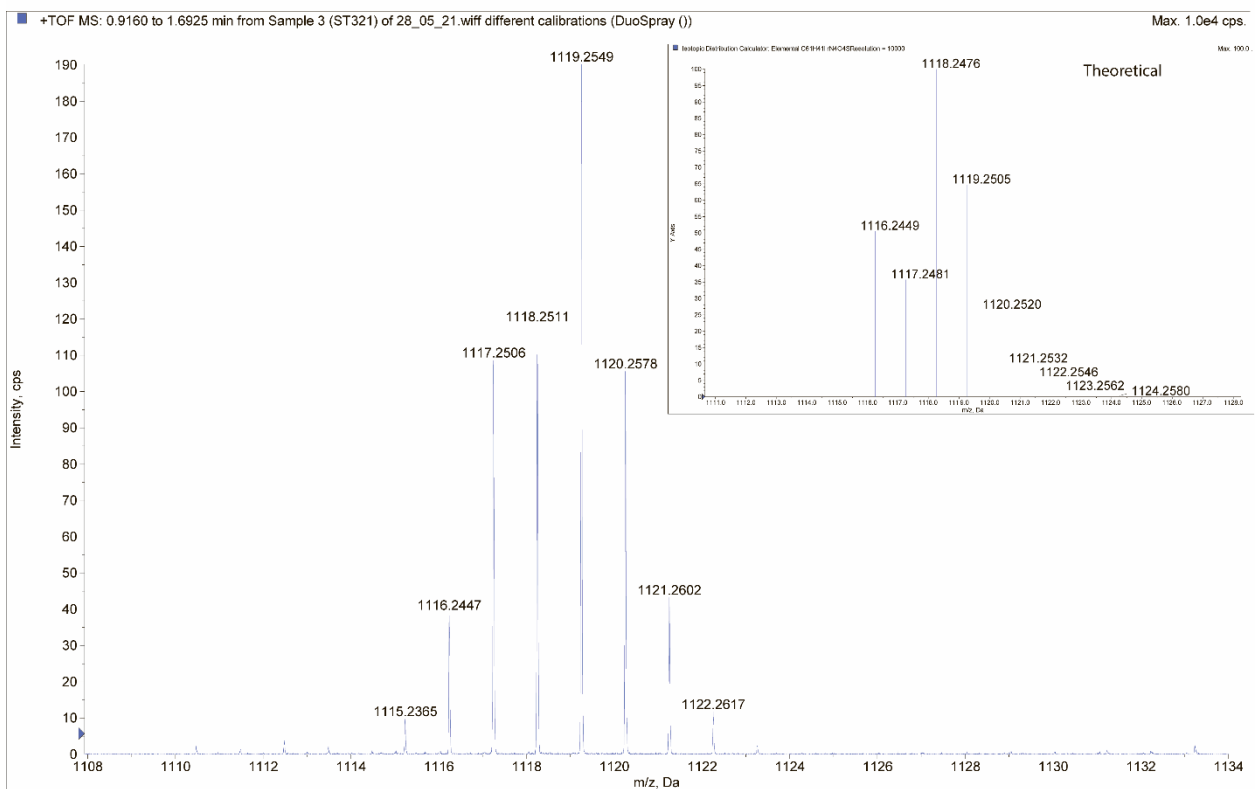


Figure S36. High resolution mass spectrum of **2**.

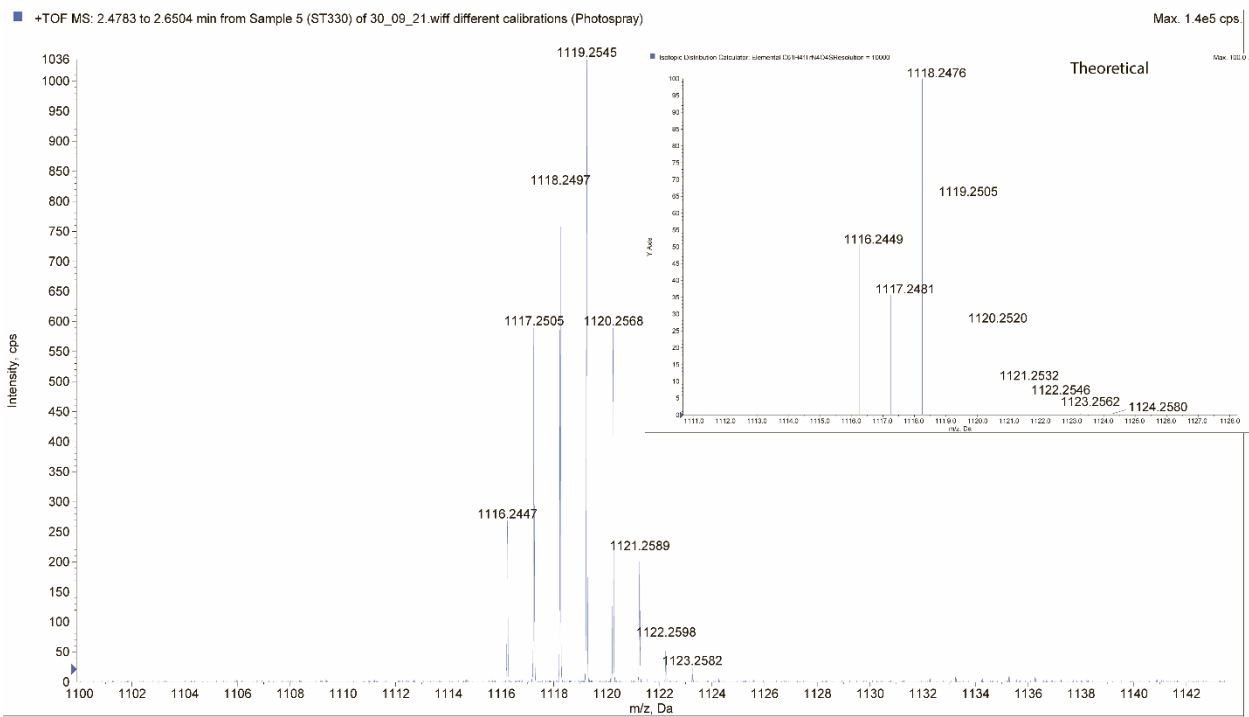


Figure S37. High resolution mass spectrum of 3.

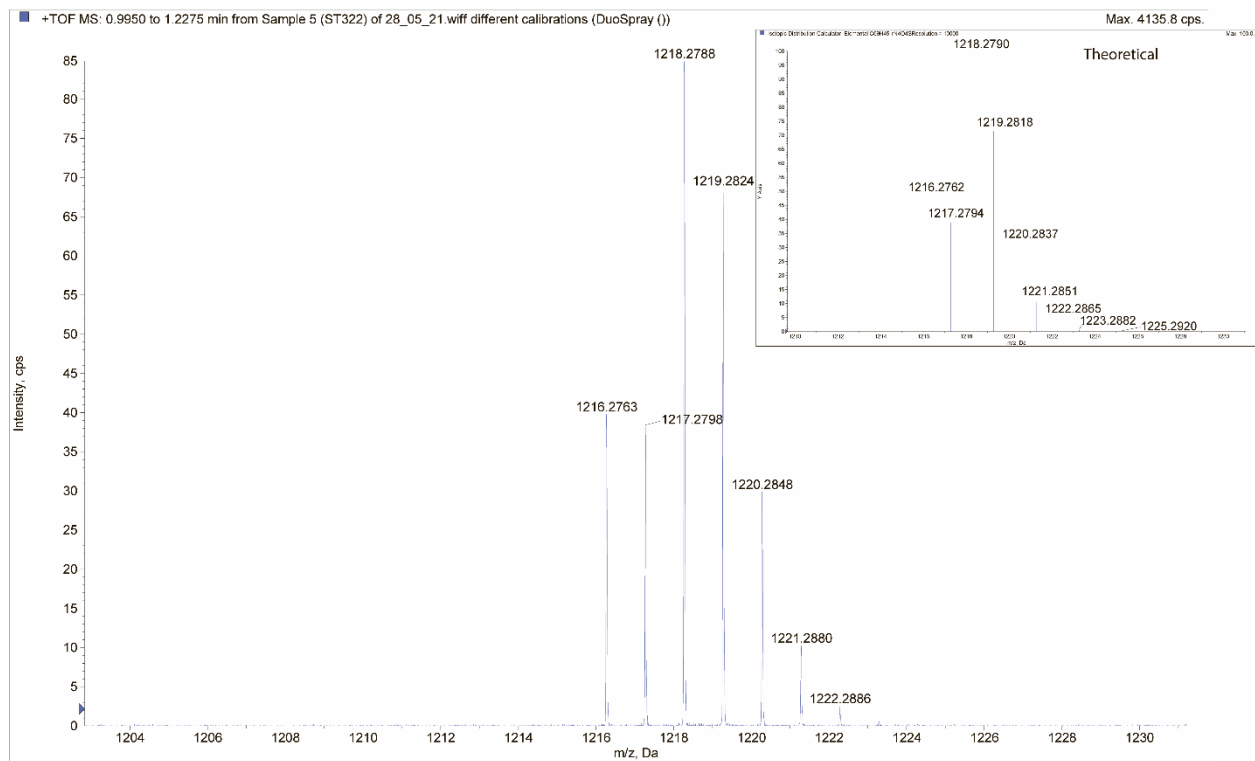


Figure S38. High resolution mass spectrum of 4.

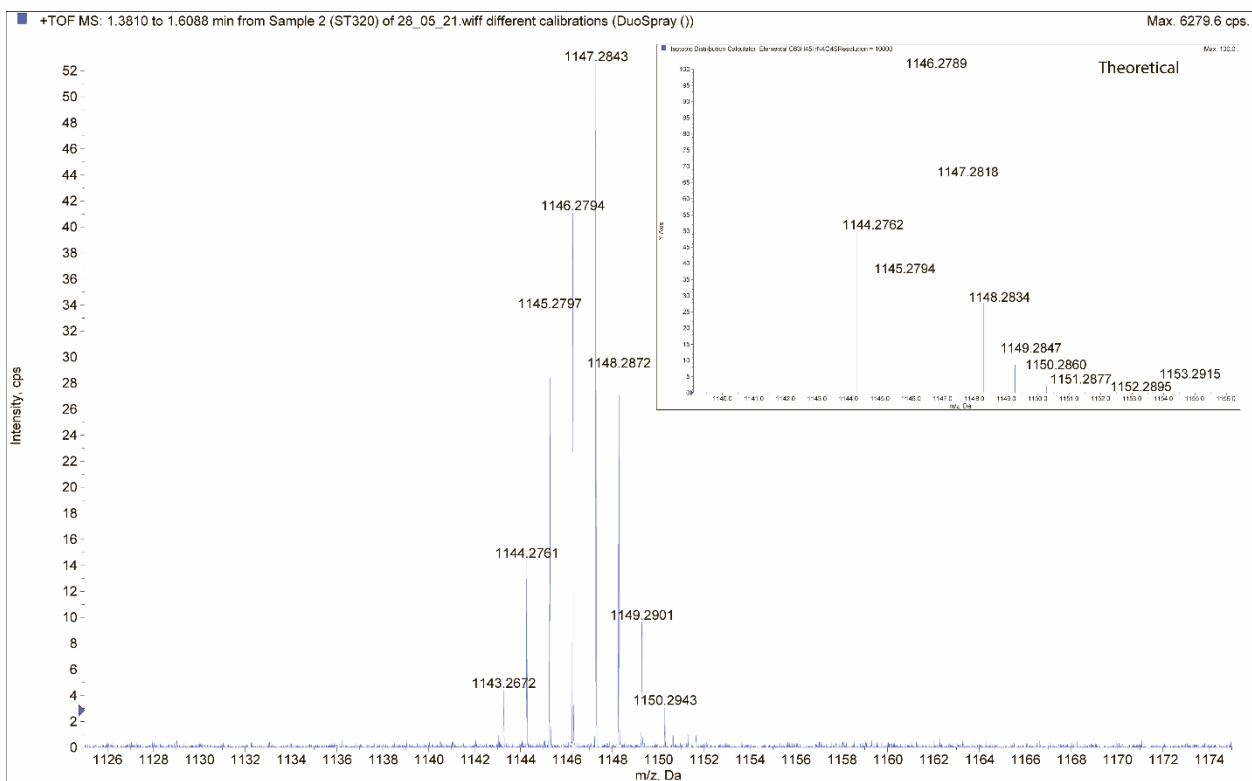


Figure S39. High resolution mass spectrum of **5**.

Table S1. Complex species (with their relative masses) in mass spectra of **1 – 5**.

	$\text{Ir}(\text{C}^{\Delta}\text{N})_2^+$	$\text{Ir}(\text{C}^{\Delta}\text{N})_2(\text{CH}_3\text{CN})^+$	$\text{Ir}(\text{C}^{\Delta}\text{N})_2(\text{CH}_3\text{CN})_2^+$	$\text{Ir}(\text{C}^{\Delta}\text{N})_2(\text{O}^{\Delta}\text{O})^+$
1	843.1224	884.1488	925.1753	1130.1616*
2	831.2094	872.2360	-	1118.2511*
3	831.2101	-	-	1118.2476*
4	931.2402	972.2665	1013.2933	1218.2788
5	859.2404	900.2667	-	1146.2794*

*The $[\text{Ir}(\text{C}^{\Delta}\text{N})_2(\text{O}^{\Delta}\text{O})^+]$ peak is superimposed to $[\text{Ir}(\text{C}^{\Delta}\text{N})_2(\text{O}^{\Delta}\text{O}) \cdot \text{H}^+]$

2. X-ray data.

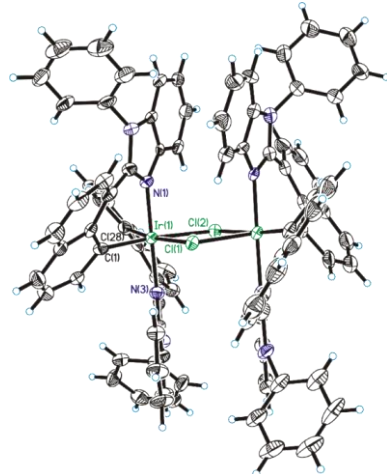


Figure S40. Molecular structure of $[\text{Ir}(\text{nbi-1})_2\text{Cl}]_2$ with 6-membered metallacycles. Displacement ellipsoids are shown at 50% probability level. Nbi-1 – 2-(1-naphthyl)-1-phenyl-benzimidazole.

Table S2. Details of the X-ray crystal data collection and structure refinement for dimeric compounds and a byproduct of the cycloiridation of **phbi**

	$[\text{Ir}(\text{btbi})_2\text{Cl}]_2$	$[\text{Ir}(\text{nbi-2})_2\text{Cl}]_2$	$[\text{Ir}(\text{phbi})_2\text{Cl}]_2$ tolu/MeCN	$[\text{Ir}(\text{phbi})_2\text{Cl}]_2$ MeCN	$[\text{Ir}(\text{phbi})_2\text{Cl}]_2$ tolu/DCM	$[\text{Ir}(\text{nbi})_2\text{Cl}]_2$	$\text{Ir}(\text{phbi})\text{-byprod}$
Empirical formula	$\text{C}_{84}\text{H}_{52}\text{Ir}_2\text{N}_8\text{Cl}_2\text{S}_4 \cdot 4 \text{CH}_2\text{Cl}_2 + \text{solvent}$	$\text{C}_{92}\text{H}_{60}\text{Cl}_2\text{Ir}_2\text{N}_8 \cdot 2 \text{CH}_2\text{Cl}_2 + \text{solvent}$	$\text{C}_{108}\text{H}_{68}\text{Cl}_2\text{Ir}_2\text{N}_8 \cdot 4 \text{C}_7\text{H}_8 \cdot 3.75 \text{CH}_3\text{CN}$	$\text{C}_{108}\text{H}_{68}\text{Cl}_2\text{Ir}_2\text{N}_8 + \text{solvent}$	$\text{C}_{108}\text{H}_{68}\text{Cl}_2\text{Ir}_2\text{N}_8 \cdot 0.71 \text{CH}_2\text{Cl}_2 + \text{solvent}$	$\text{C}_{96}\text{H}_{68}\text{Ir}_2\text{N}_8\text{Cl}_2 \cdot 7 \text{CHCl}_3$	$\text{C}_{81}\text{H}_{52}\text{Ir}_2\text{N}_6\text{Cl}_4 \cdot 3 \text{CHCl}_3$
M_w	2096.58	1902.63	2455.49	1933.00	2053.59	2624.46	1993.59
Temperature (K)	100	100	100	150	300	100	150
Size (mm)	0.22 x 0.10 x 0.02	0.18 x 0.12 x 0.03	0.20 x 0.20 x 0.17	0.22 x 0.20 x 0.04	0.04 x 0.04 x 0.03	0.22 x 0.16 x 0.07	0.10 x 0.08 x 0.03
Cryst. system	monoclinic	triclinic	triclinic	monoclinic	orthorhombic	monoclinic	monoclinic
Space group	P2 ₁ /n	P-1	P-1	P2 ₁ /c	Fddd	P2/n	P2 ₁ /n
a (Å)	15.4885(6)	15.3068(14)	17.2379(10)	22.7610(10)	16.251(3)	17.1401(6)	19.5439(6)
b (Å)	18.8194(8)	20.1424(17)	17.7094(11)	18.6141(8)	35.942(6)	11.0817(4)	17.4940(6)
c (Å)	28.3873(12)	26.750(2)	19.7481(12)	25.9710(11)	37.688(6)	26.8175(10)	22.5983(7)
α (°)		92.839(3)	112.254(2)				
β (°)	100.212(2)	102.348(3)	90.911(2)	110.7000(210)		94.5540(10)	98.7730(10)
γ (°)		97.433(3)	93.085(2)				
V (Å ³)	8143.4(6)	7963.4(12)	5567.1(6)	10292.9(8)	22013(6)	5077.7(3)	7636.0(4)
Z	4	4	2	4	8	2	4
ρ_{cald} (g·cm ⁻³)	1.710	1.587	1.465	1.247	1.239	1.717	1.734
Abs coeff (mm ⁻¹)	3.749	3.594	2.497	2.681	2.578	3.276	3.988
$F(000)$	4128	3760	2485	3840	8157	2588	3904
θ range (deg)	1.72 < θ < 28.00	1.84 < θ < 27.00	2.10 < θ < 29.00	1.84 < θ < 25.65	2.13 < θ < 25.05	2.29 < θ < 28.29	1.90 < θ < 28.31
no. of collected/unique rflns	140524/19650	180454/34655	220131/29585	53307/19333	79219/4887	91811/12590	142791/18981
Completeness to θ (%)	99.9	99.6	100	99.3	99.9	99.7	99.9
no. of data/restraints/params	19650/0/1009	34655/6/1975	29585/13/1418	19333/317/1057	4887/2/250	12590/0/632	18981/0/946
Goodness of fit on F^2	1.018	1.045	1.036	1.043	1.071	1.025	1.063
Final R indices ($I > 2\sigma(I)$)	$R_1 = 0.038$, $wR_2 = 0.0780$	$R_1 = 0.0407$, $wR_2 = 0.0877$	$R_1 = 0.0201$, $wR_2 = 0.0482$	$R_1 = 0.0363$, $wR_2 = 0.0856$	$R_1 = 0.0427$, $wR_2 = 0.1021$	$R_1 = 0.0309$, $wR_2 = 0.0565$	$R_1 = 0.0349$, $wR_2 = 0.0727$
R indices (all data)	$R_1 = 0.0617$, $wR_2 = 0.0872$	$R_1 = 0.0510$, $wR_2 = 0.0916$	$R_1 = 0.0235$, $wR_2 = 0.0501$	$R_1 = 0.0549$, $wR_2 = 0.0924$	$R_1 = 0.0546$, $wR_2 = 0.1072$	$R_1 = 0.0408$, $wR_2 = 0.0593$	$R_1 = 0.0477$, $wR_2 = 0.0771$
Largest diff peak/hole (e·Å ⁻³)	1.06/-1.05	2.00/-2.57	1.02/-0.92	0.80/-0.92	0.58/-0.62	1.36/-1.55	1.75/-1.19

Table S3. Details of the X-ray crystal data collection and structure refinement for complexes **1 – 5**.

	1	2	3	4	5
Empirical formula	C ₅₇ H ₃₇ IrN ₄ O ₄ S ₃ · 1.4 CH ₂ Cl ₂	C ₆₁ H ₄₀ IrN ₄ O ₄ S· solvent	C ₆₁ H ₄₁ IrN ₄ O ₄ S· 1.25 CH ₂ Cl ₂	C ₆₉ H ₄₅ IrN ₄ O ₄ S· 0.73 CH ₃ CN	C ₆₃ H ₄₅ IrN ₄ O ₄ S· solvent
M _w	1249.18	1117.25	1224.39	1248.45	1146.32
Temperature (K)	100	150	100	150	100
Size (mm)	0.30 x 0.20 x 0.05	0.28 x 0.02 x 0.02	0.31 x 0.22 x 0.01	0.36 x 0.13 x 0.10	0.20 x 0.10 x 0.01
Cryst. system	triclinic	monoclinic	orthorhombic	monoclinic	monoclinic
Space group	P-1	C2/c	Pbca	P2 ₁ /n	P2 ₁ /n
a (Å)	10.4137(4)	25.8571(14)	18.7713(15)	15.4518(6)	10.6807(6)
b (Å)	15.4601(7)	15.6822(9)	21.0313(17)	20.9908(9)	26.4091(14)
c (Å)	17.0359(7)	18.7424(19)	27.802(2)	18.0568(6)	18.1462(10)
α(°)	87.025(2)				
β (°)	74.0030(10)	126.9190(10)		97.6220(10)	99.722(2)
γ(°)	77.2810(10)				
V (Å ³)	2571.71(19)	6076.1(8)	10975.6(15)	5804.9(4)	5044.9(5)
Z	2	4	8	4	4
ρ _{cald} (g·cm ⁻³)	1.613	1.221	1.482	1.429	1.509
Abs coeff (mm ⁻¹)	2.916	2.276	2.644	2.391	2.743
F(000)	1246	2236	4900	2513	2304
θ range (deg)	2.08 < θ < 26.38	1.97 < θ < 25.05	1.63 < θ < 25.05	1.63 < θ < 26.40	1.38 < θ < 25.70
no. of collected/unique rflns	26981/10302	14698/5337	356673/9707	61714/11836	76761/9574
Completeness to θ (%)	97.9	99.3	99.9	99.3	100
no. of data/restraints/params	10302/49/700	5337/130/330	9707/47/695	11836/72/770	9574/12/623
Goodness of fit on F ²	1.068	1.028	1.187	1.067	1.048
Final R indices (I > 2σ(I))	R ₁ = 0.0350, wR ₂ = 0.0752	R ₁ = 0.0602, wR ₂ = 0.1607	R ₁ = 0.0572, wR ₂ = 0.1348	R ₁ = 0.0459, wR ₂ = 0.1281	R ₁ = 0.0481, wR ₂ = 0.1132
R indices (all data)	R ₁ = 0.0427, wR ₂ = 0.0777	R ₁ = 0.0798, wR ₂ = 0.1717	R ₁ = 0.0624, wR ₂ = 0.1376	R ₁ = 0.0553, wR ₂ = 0.1352	R ₁ = 0.0711, wR ₂ = 0.1235
Largest diff peak/hole (e/Å ³)	1.07/-1.03	2.24/-0.87	1.82/-1.70	1.56/-1.24	1.13 /-1.67

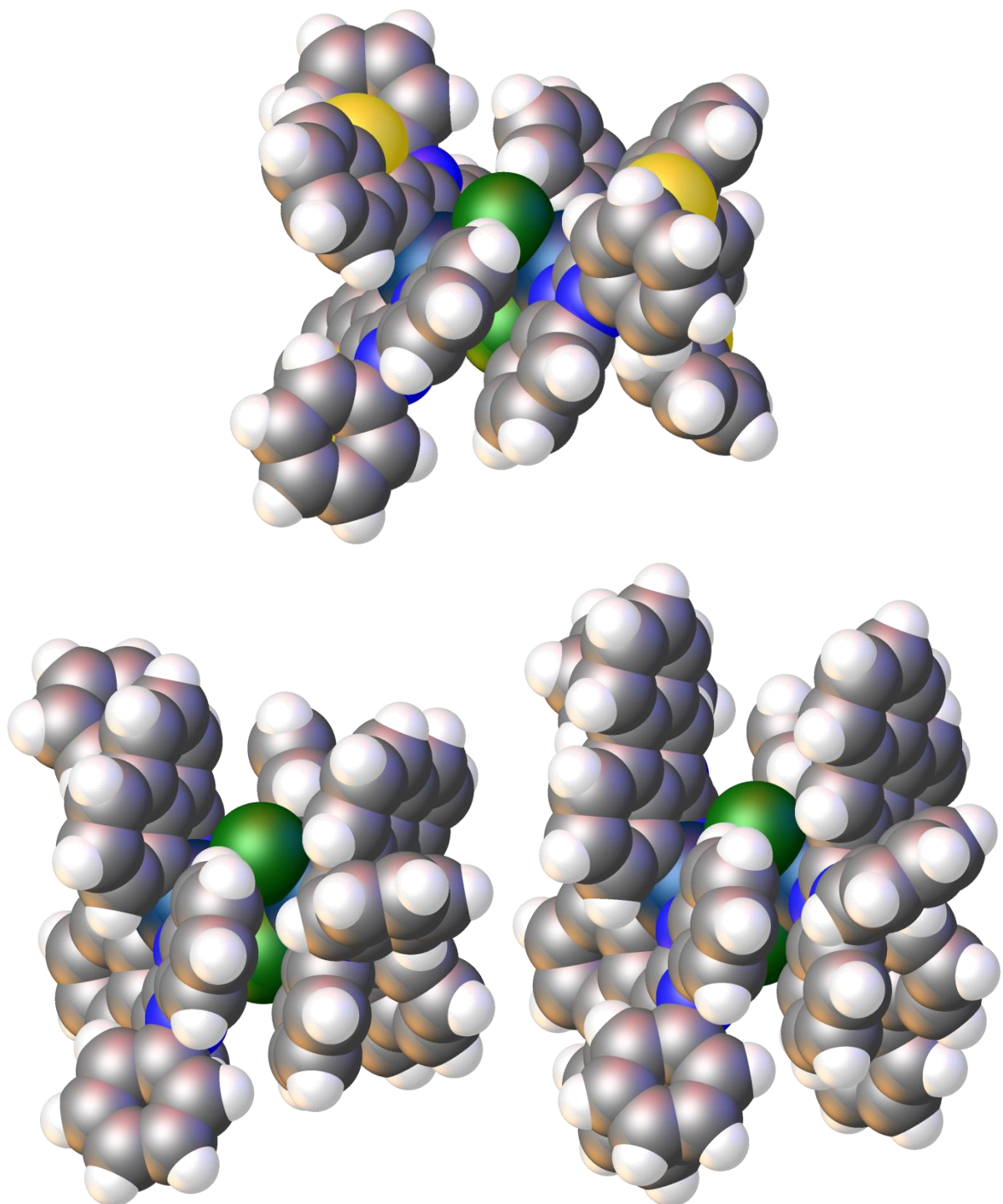


Figure S41. The steric accessibility of chlorides in $[\text{Ir}(\text{btbi})_2\text{Cl}]_2$ (upper), $[\text{Ir}(\text{nbi}-1)_2\text{Cl}]_2$ (lower left) and $[\text{Ir}(\text{phbi})_2\text{Cl}]_2$ (lower right).

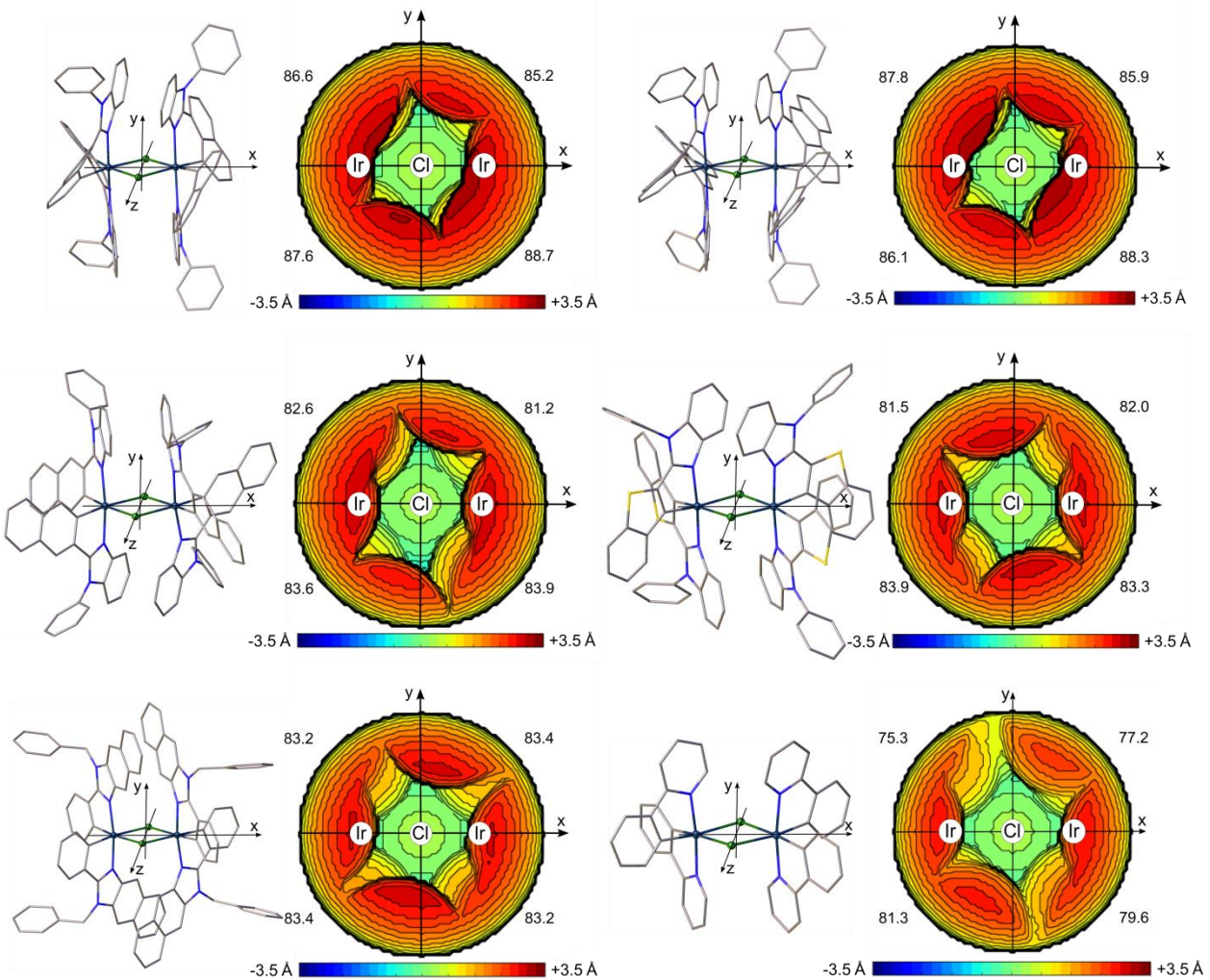


Figure S42. The steric quadrant maps¹ based on the obtained crystal structures of dimeric chlorides and on the structure of $[\text{Ir}(\text{ppy})_2\text{Cl}]_2$.

As evidenced by the steric quadrant maps (Fig. S42), the buried volume (V_{bur}) values in the ppy-based dimer vary within the range 75.3 – 81.3%. Three benzimidazole-based dimers containing five-membered metallacycles possess somewhat larger V_{bur} (81.2 – 83.9%) whereas those having six-membered metallacycles show maximal V_{bur} values in the series (85.2 – 88.7%). The increase in % V_{bur} values reflects the increased steric shielding of the Ir_2Cl_2 cores forming six-membered metallacycles and correlates with the observed decrease in reactivity. Still, the change of % V_{bur} in going from five- to six-membered metallacycles is not so drastic and even just a little to state unambiguously that the steric effects play a key role in determining the reactivity of the dimers. We should suppose that either small changes in steric bulk of the ligands have great effect on the reactivity of the dimers or there are additional factors, for example, differences in solubility of the dimers influencing the rate of their cleavage.

Table S4. Selected bond lengths [Å] and angles [°] in structures of the complexes

	Ir ₁ –C ₁	Ir ₁ –C ₂₂	Ir ₁ –N ₁	Ir ₁ –N ₃	Ir ₁ –O ₄	Ir ₁ –O ₃
Complex 1	1.998(4)	2.013(4)	2.046(3)	2.041(3)	2.114(3)	2.118(3)
	C ₁ –Ir ₁ –C ₂₂	N ₁ –Ir ₁ –C ₂₂	C ₁ –Ir ₁ –N ₃	C ₁ –Ir ₁ –O ₃	C ₂₂ –Ir ₁ –O ₄	N ₁ –Ir ₁ –O ₃
	95.99(15)	100.44(15)	99.77(15)	86.19(13)	89.15(13)	83.97(12)
Complex 2	Ir ₁ –C ₂₄	Ir ₁ –C ₁	Ir ₁ –N ₃	Ir ₁ –N ₁	Ir ₁ –O ₄	Ir ₁ –O ₃
	2.000(7)	2.015(7)	2.030(6)	2.034(6)	2.132(5)	2.132(5)
	C ₁ –Ir ₁ –C ₂₄	N ₁ –Ir ₁ –C ₂₄	C ₁ –Ir ₁ –N ₃	C ₁ –Ir ₁ –O ₃	C ₂₄ –Ir ₁ –O ₄	N ₁ –Ir ₁ –O ₄
Complex 3*	95.6(3)	93.7(3)	98.4(2)	88.1(2)	87.0(2)	96.0(2)
	Ir ₁ –C ₁		Ir ₁ –N ₁			Ir ₁ –O ₃
	1.972(9)		2.047(6)			2.145(6)
	C ₁ –Ir ₁ –C ₁ ¹	N ₁ –Ir ₁ –C ₁ ¹				
Complex 4	92.1(5)	79.1(3)				
	Ir ₁ –C ₁	Ir ₁ –C ₂₈	Ir ₁ –N ₁	Ir ₁ –N ₃	Ir ₁ –O ₃	Ir ₁ –O ₄
	2.015(5)	2.003(5)	2.017(4)	2.015(4)	2.149(4)	2.144(4)
	C ₁ –Ir ₁ –C ₂₈	N ₁ –Ir ₁ –C ₂₈	C ₁ –Ir ₁ –N ₃	C ₁ –Ir ₁ –O ₄	C ₂₈ –Ir ₁ –O ₃	N ₃ –Ir ₁ –O ₃
Complex 5	92.4(2)	92.93(18)	91.43(19)	89.41(19)	90.43(18)	84.04(15)
	Ir ₁ –C ₁	Ir ₁ –C ₂₅	Ir ₁ –N ₁	Ir ₁ –N ₃	Ir ₁ –O ₄	Ir ₁ –O ₃
	1.991(8)	1.995(7)	2.034(6)	2.038(5)	2.155(4)	2.156(5)
	C ₁ –Ir ₁ –C ₂₅	N ₁ –Ir ₁ –C ₂₅	C ₁ –Ir ₁ –N ₃	C ₁ –Ir ₁ –O ₃	C ₂₅ –Ir ₁ –O ₄	N ₁ –Ir ₁ –O ₃
	91.6(3)	94.0(2)	93.2(2)	90.5(2)	90.0(2)	89.67(19)
						91.53(18)

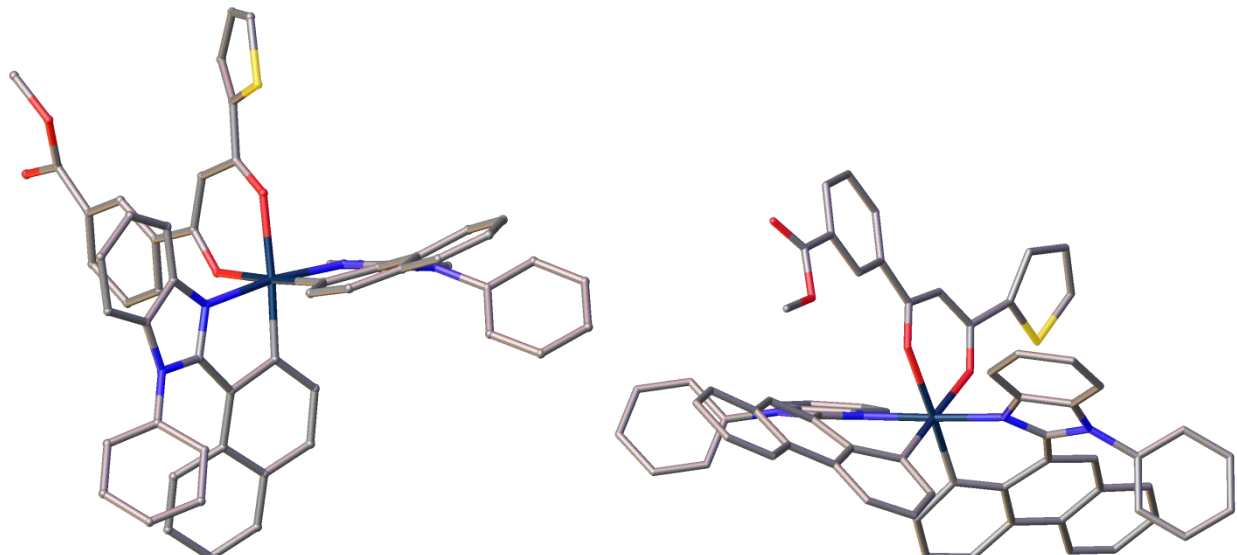


Figure S43. Curvature in cyclometalated ligands in **2**(left) and **4**(right). Minor parts of the disordered groups are not shown.

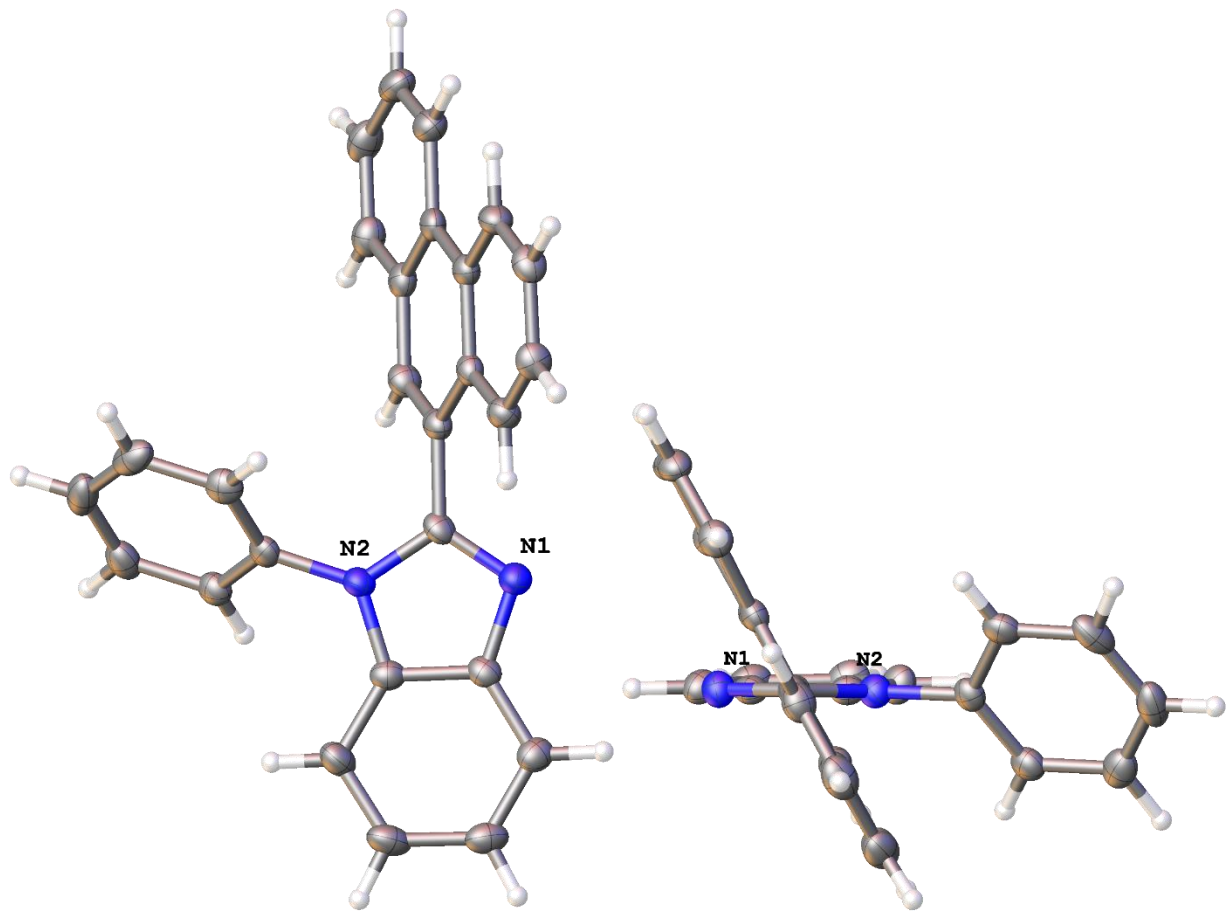


Figure S44. Crystal structure of phbi. Displacement ellipsoids are shown at 50% probability level.

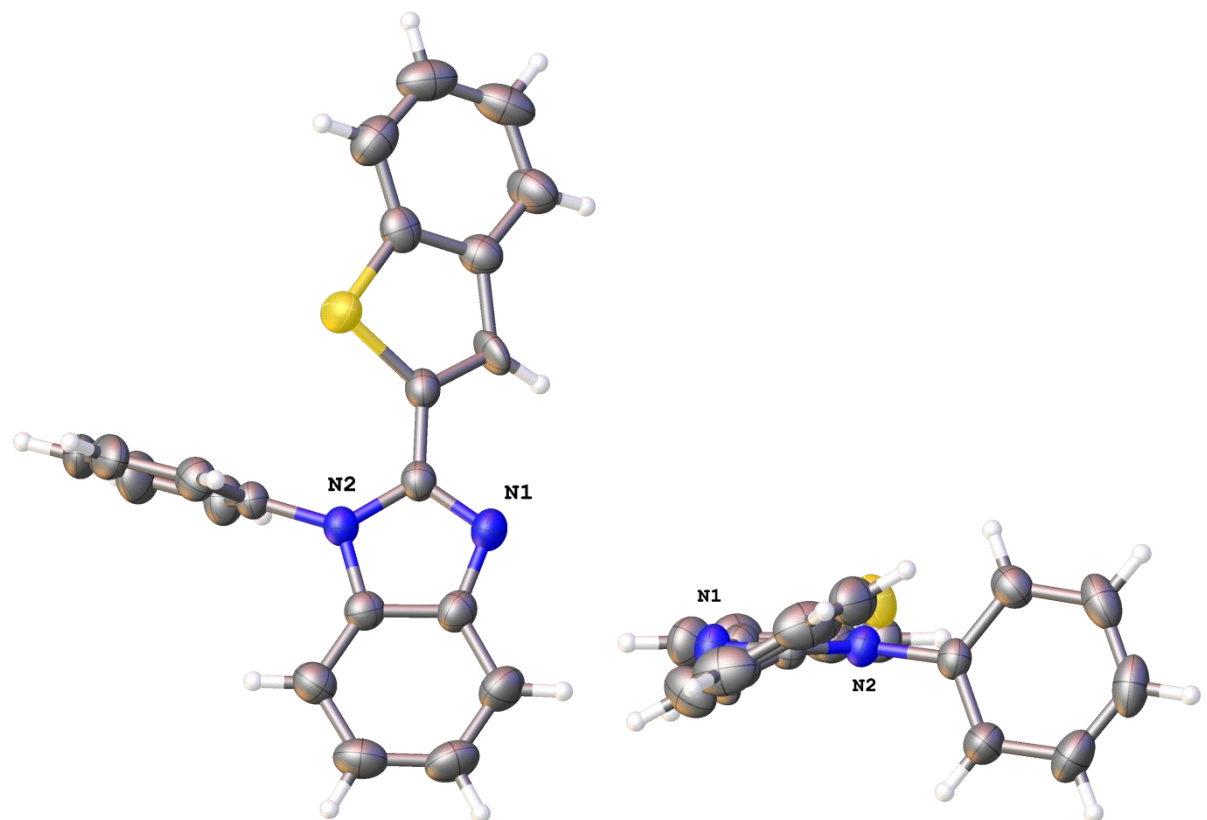


Figure S45. Crystal structure of btbi. Displacement ellipsoids are shown at 50% probability level.

Table S5. Details of the X-ray crystal data collection and structure refinement for btbi and phbi

	btbi	phbi	ρ_{calcd} (g·cm ⁻³)	1.344	1.328
Empirical formula	C ₂₁ H ₁₄ N ₂ S	C ₂₇ H ₁₈ N ₂	Abs coeff (mm ⁻¹)	0.204	0.078
M _w	326.40	370.43	F(000)	680	776
Temperature (K)	300	150	θ range (deg)	2.16 < θ < 30.54	2.04 < θ < 26.45
Size (mm)	0.25 x 0.16 x 0.12	0.33 x 0.23 x 0.15	no. of collected/unique rflns	20708/4906	28963/3719
Cryst. system	monoclinic	monoclinic	Completeness to θ (%)	99.5	97.3
Space group	P2 ₁ /n	P2 ₁ /n	no. of data/restraints/params	4906/8/223	3719/0/334
<i>a</i> (Å)	9.1681(2)	9.1727(6)	Goodness of fit on F^2	1.024	1.152
<i>b</i> (Å)	9.3185(2)	15.2710(9)	Final <i>R</i> indices ($I > 2\sigma(I)$)	$R_1 = 0.0658$, $wR_2 = 0.1697$	$R_1 = 0.0663$, $wR_2 = 0.1148$
<i>c</i> (Å)	18.9846(4)	13.7145(9)	<i>R</i> indices (all data)	$R_1 = 0.0901$, $wR_2 = 0.1863$	$R_1 = 0.0860$, $wR_2 = 0.1211$
α (°)			Largest diff peak/hole (e/Å ³)	0.57/-0.47	0.21/-0.26
β (°)	95.9020(10)	105.267(3)			
γ (°)					
V (Å ³)	1613.31(6)	1853.3(2)			
Z	4	4			

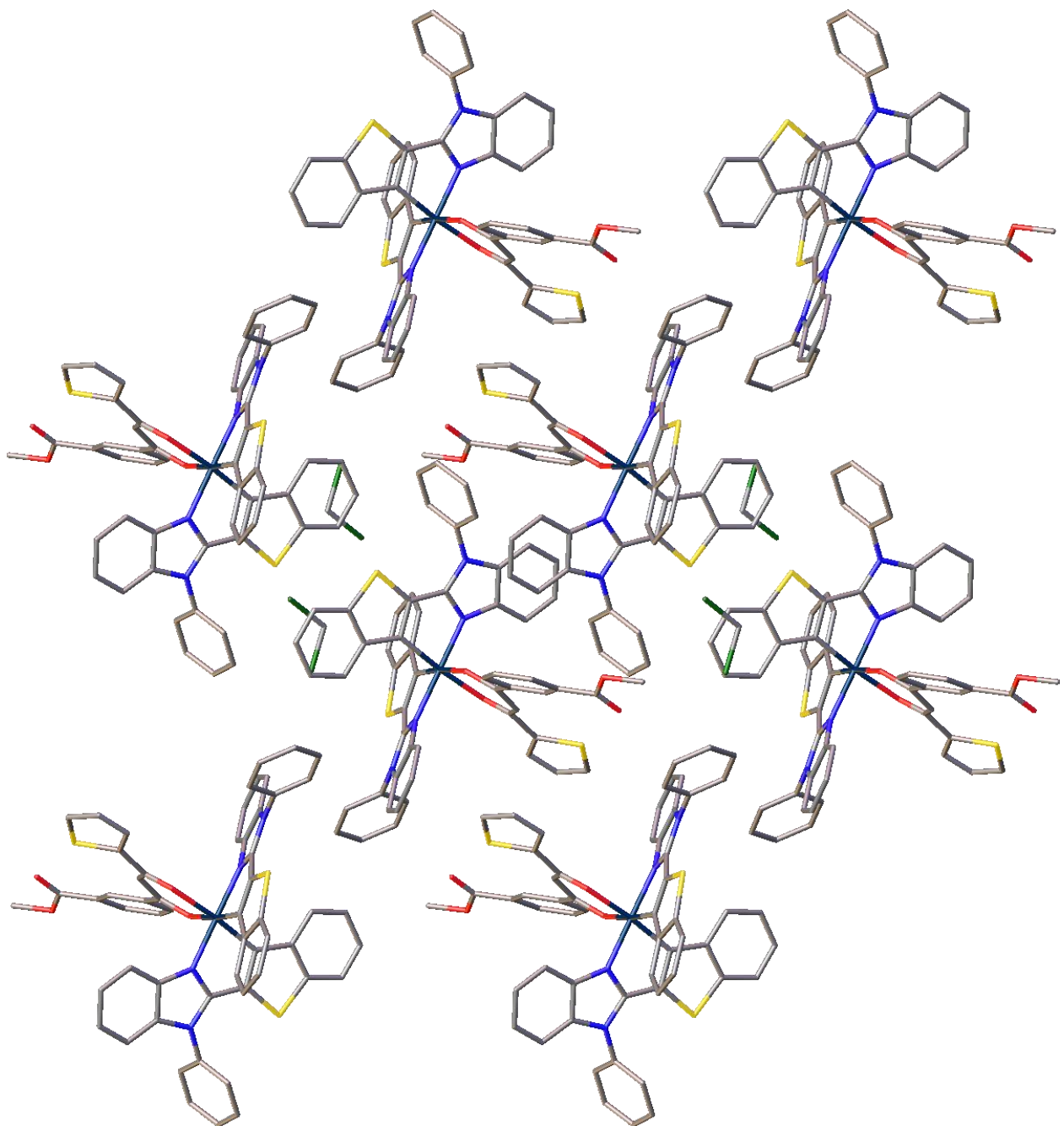


Figure S46. Fragment of the crystal packing of complex **1**. Minor components of disordered groups are not shown.

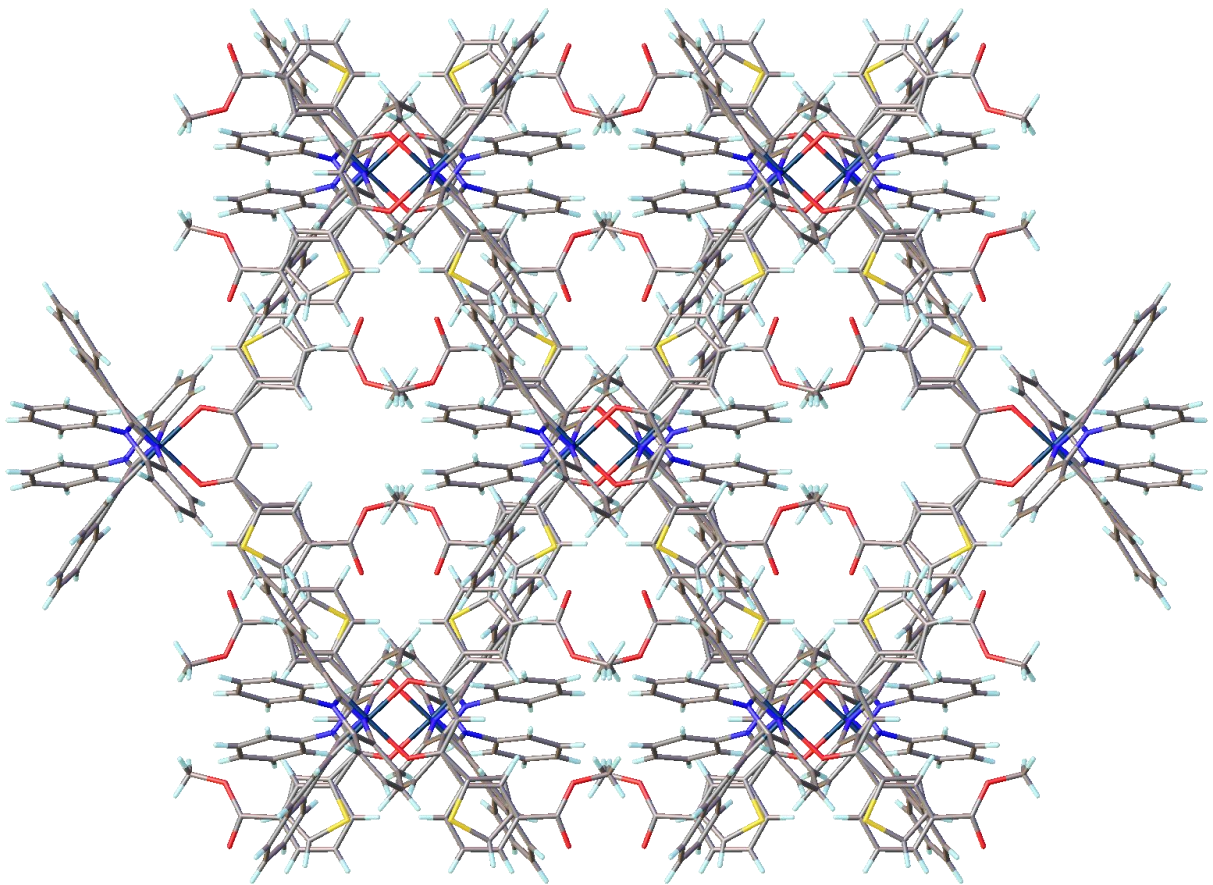


Figure S47. Fragment of the crystal packing of complex 2. Image along 2 axis.

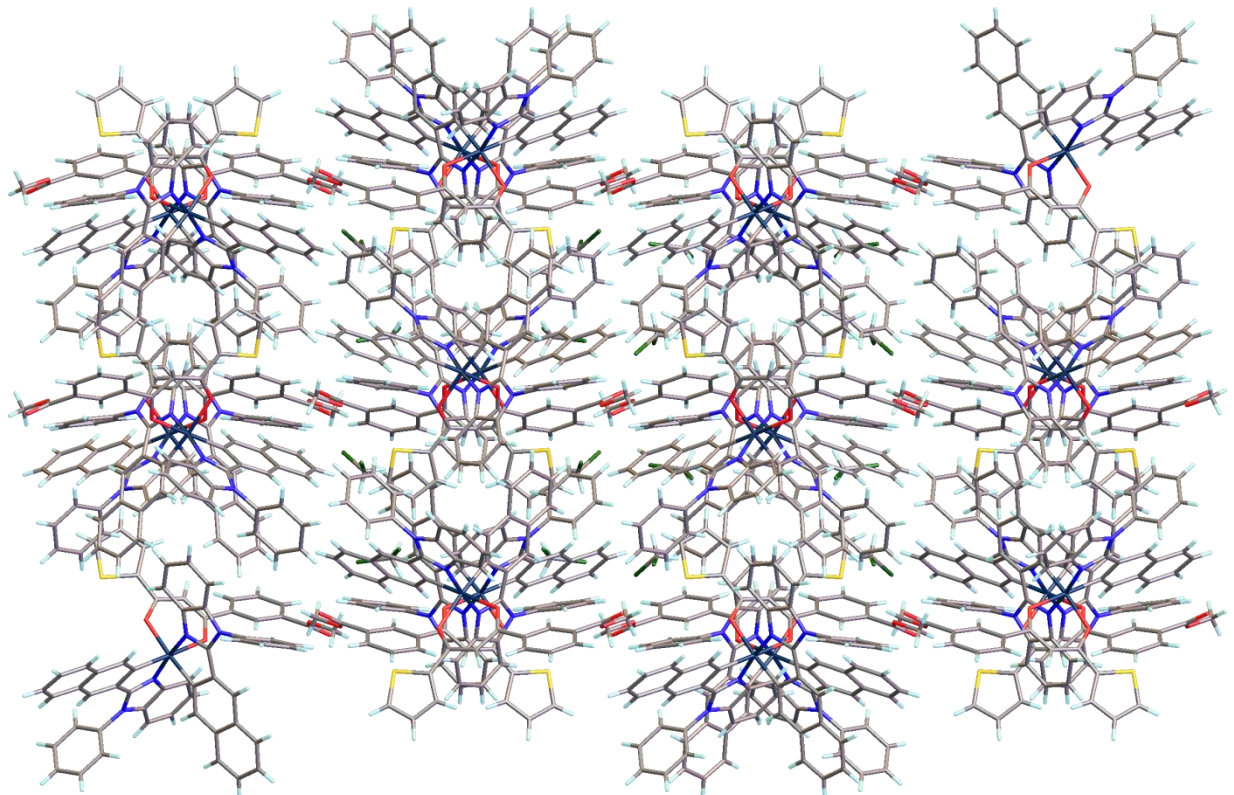


Figure S48. Fragment of the crystal packing of complex 3. Image along a plane. Minor components of disordered groups are not shown.

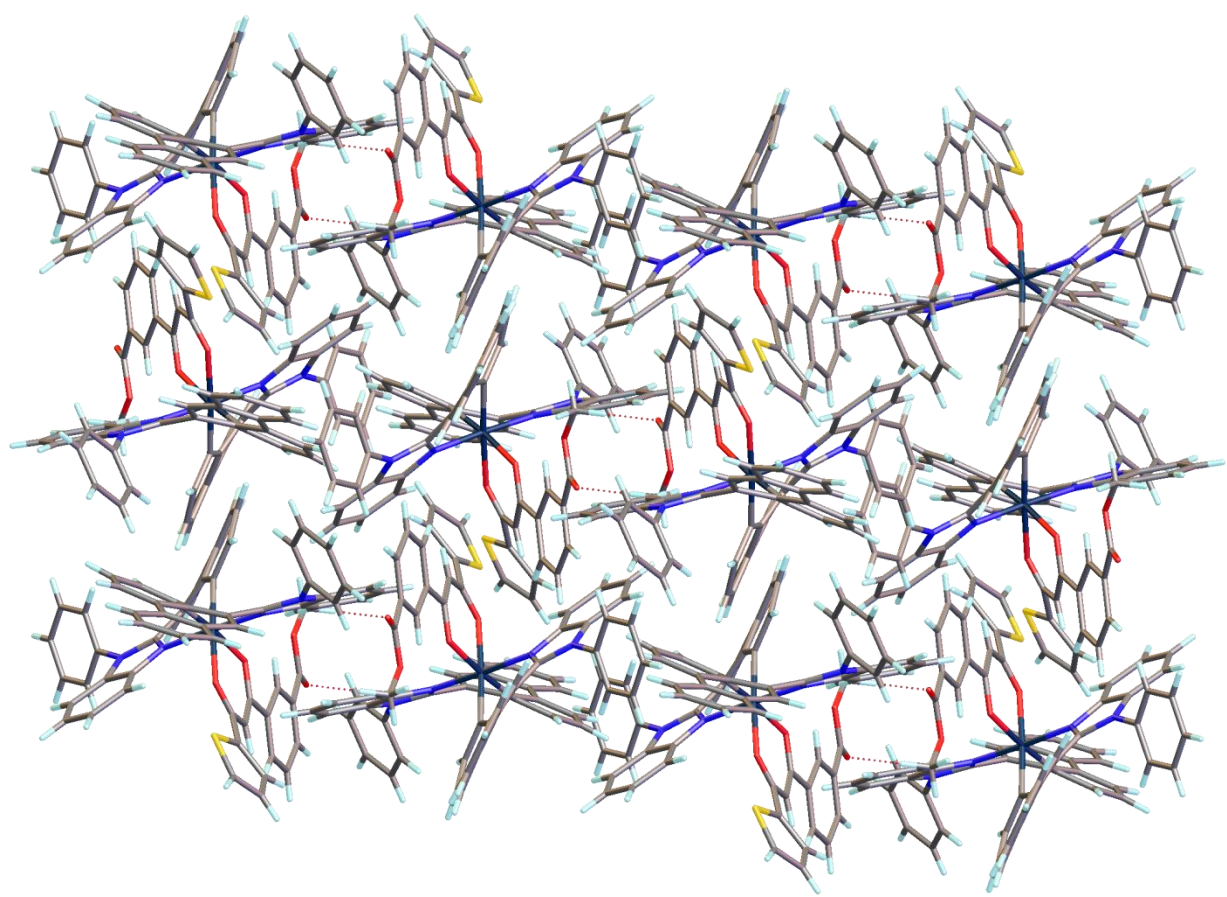


Figure S49. Fragment of the crystal packing of complex **4**. Image along 2_1 axis. Minor components of disordered groups are not shown.

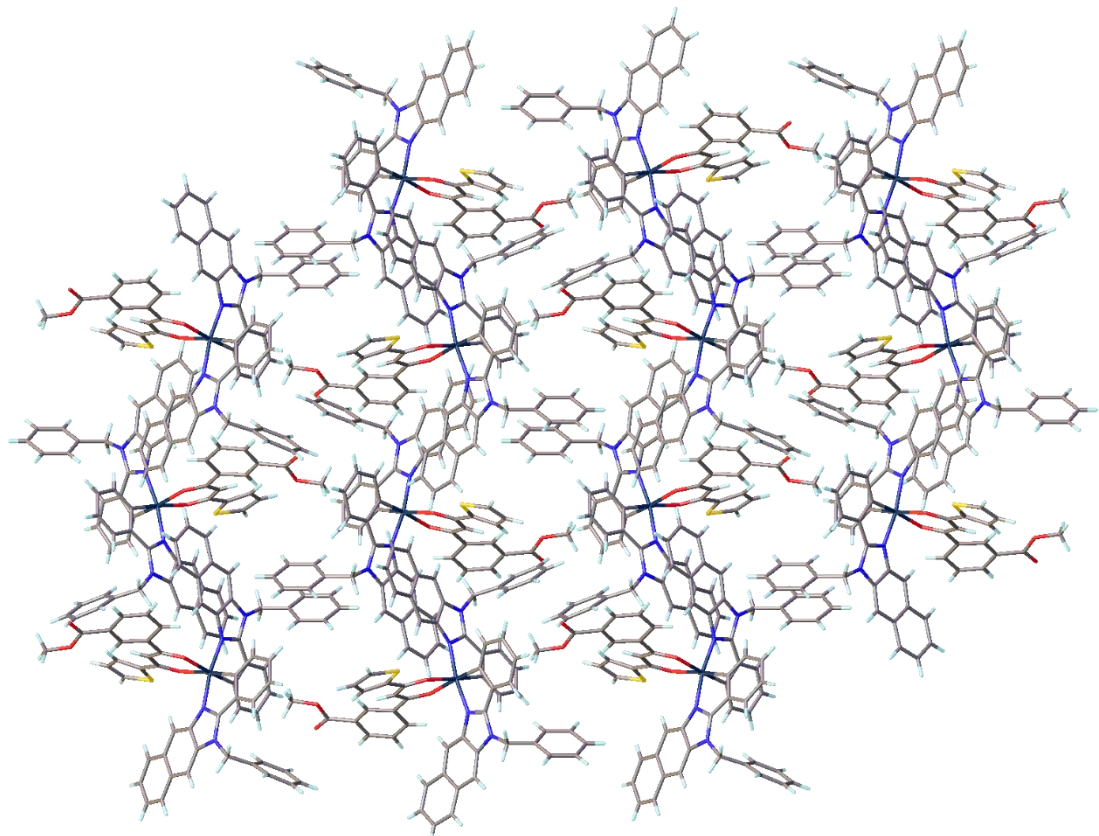


Figure S50. Fragment of the crystal packing of complex **5**. Image along 2_1 axis; minor components of disordered groups are not shown.

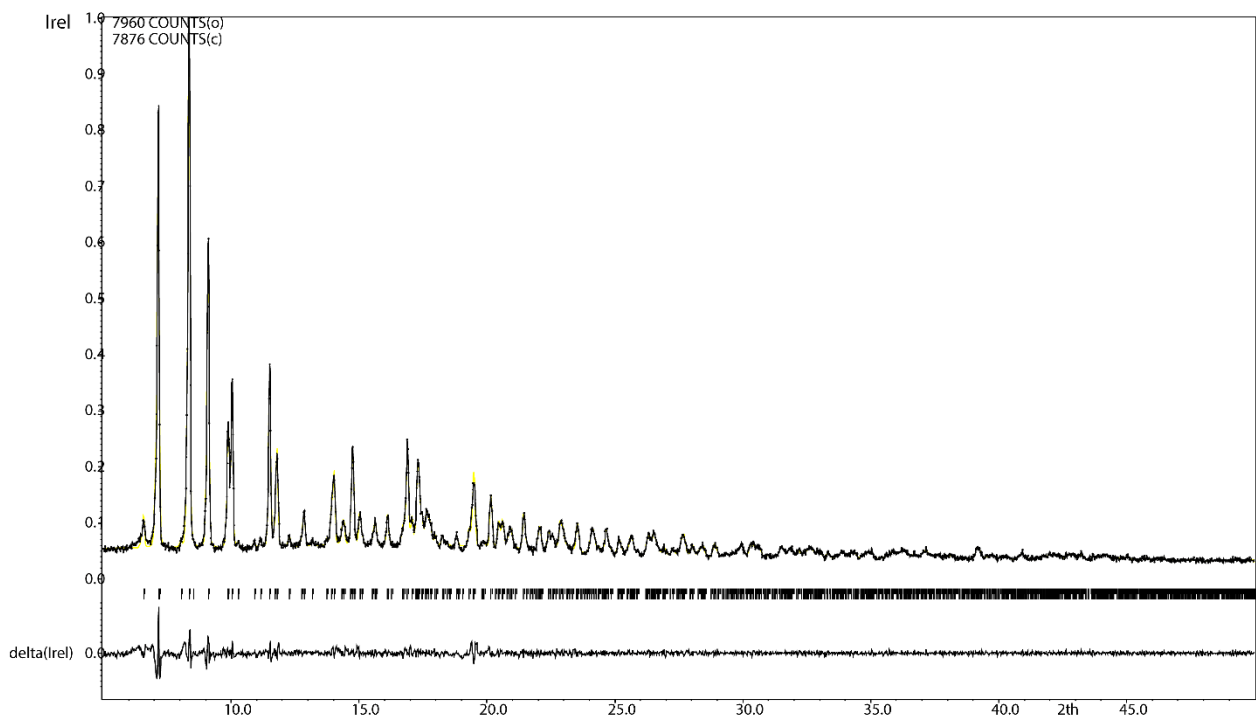


Figure S51. Powder XRD pattern of complex **4** (black line) with the simulated pattern (yellow line). The differential is presented in the bottom.

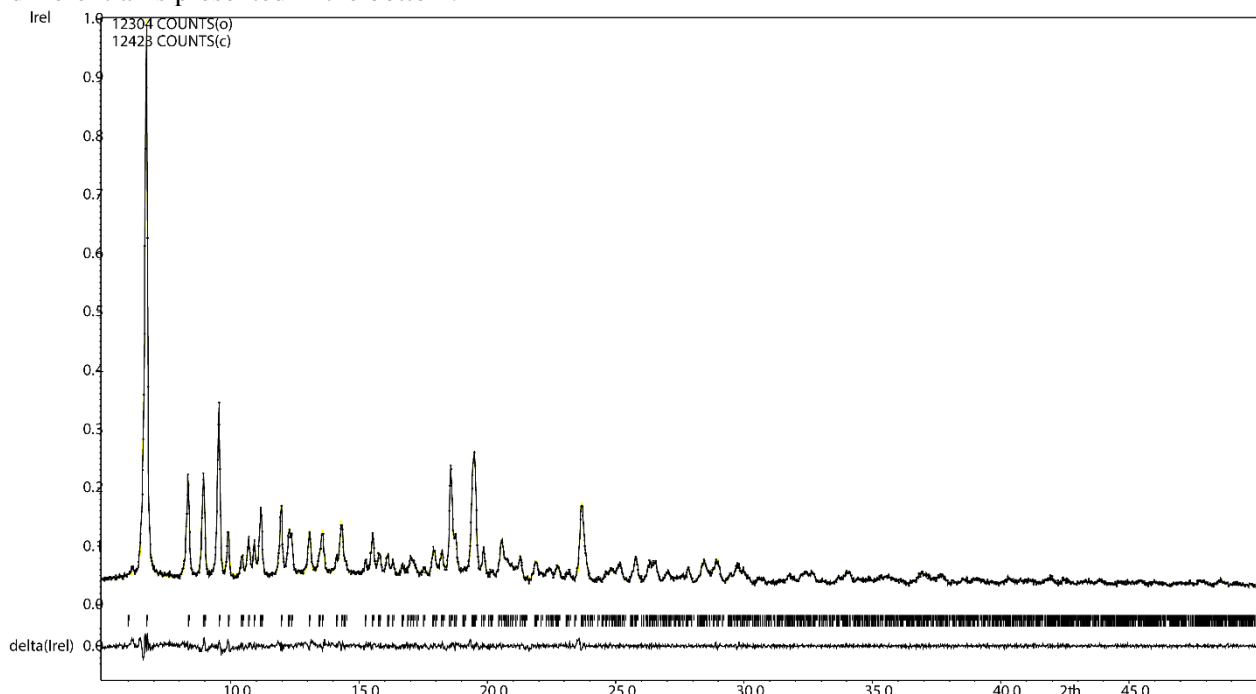


Figure S52. Powder XRD pattern of complex **5** (black line) with the simulated pattern (yellow line). The differential is presented in the bottom.

3. Redox and optical properties.

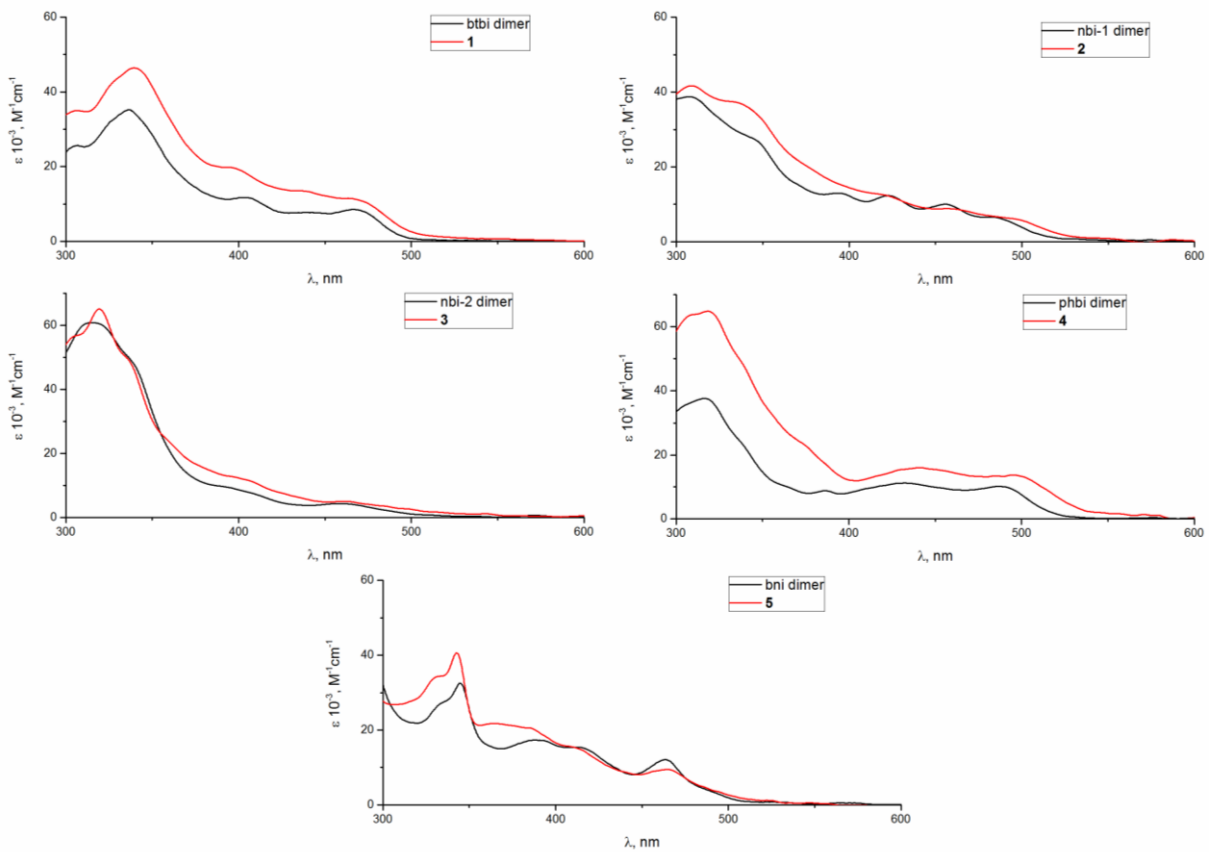


Figure S53. Comparison of absorption spectra of synthesized complexes (red) and corresponding dimeric compounds (black).

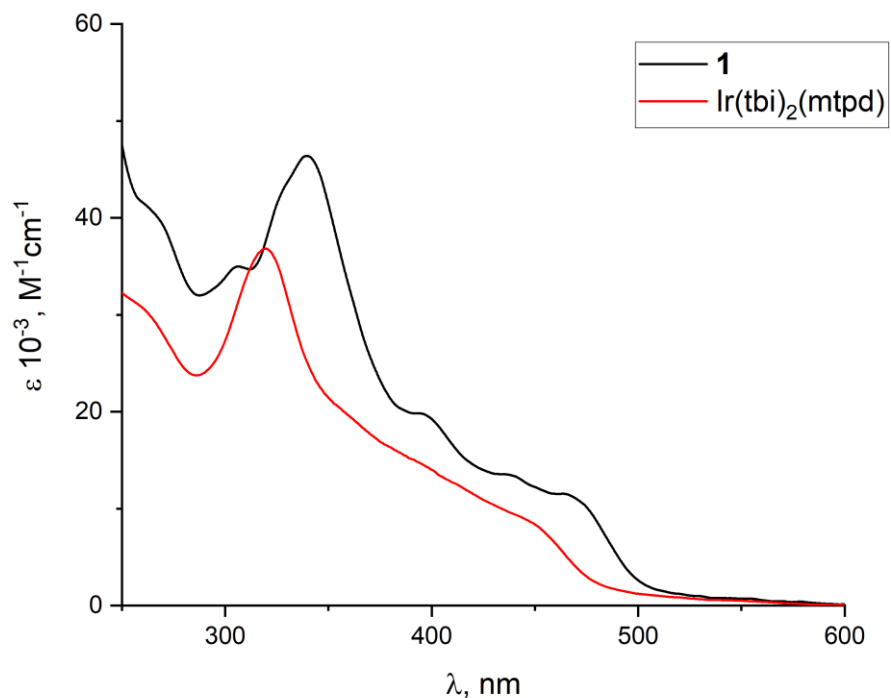


Figure S54. Comparison of absorption spectra of complex **1** with absorption spectra of $\text{Ir}(\text{tbi})_2(\text{mtpd})^2$ (measured in CH_2Cl_2 at 25°C).

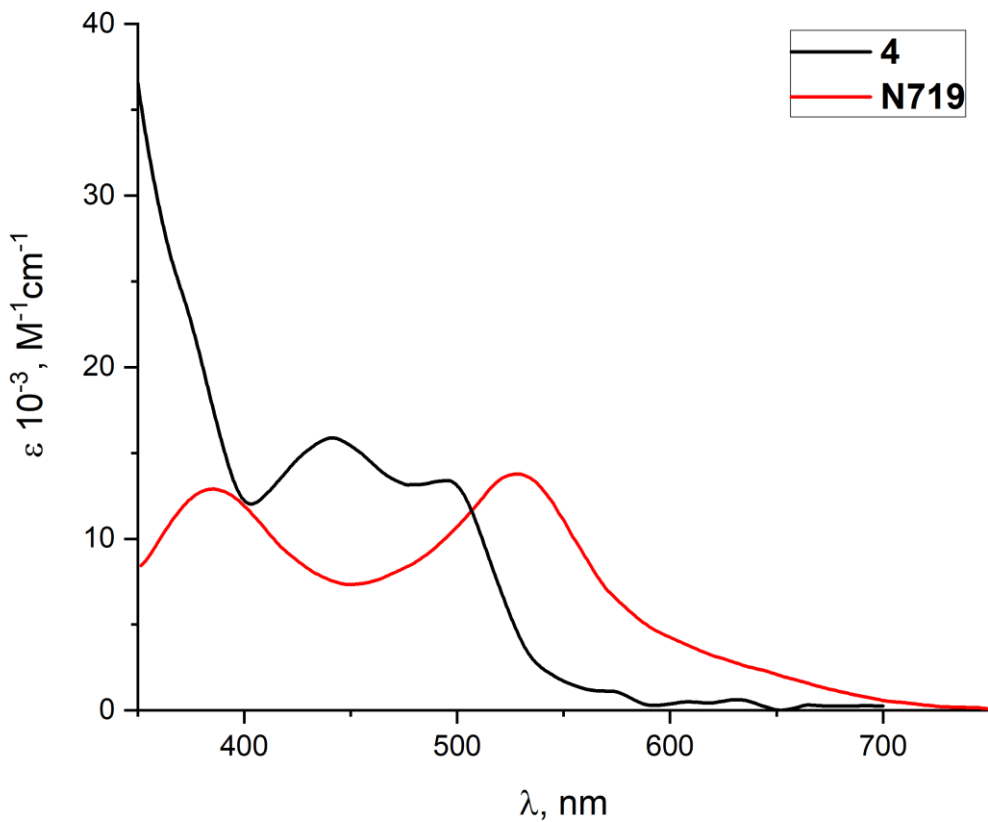


Figure S55. Comparison of absorption spectra of complex **4** with absorption spectra of N719 photosensitizer (measured in CH_2Cl_2 at $25^\circ C$).

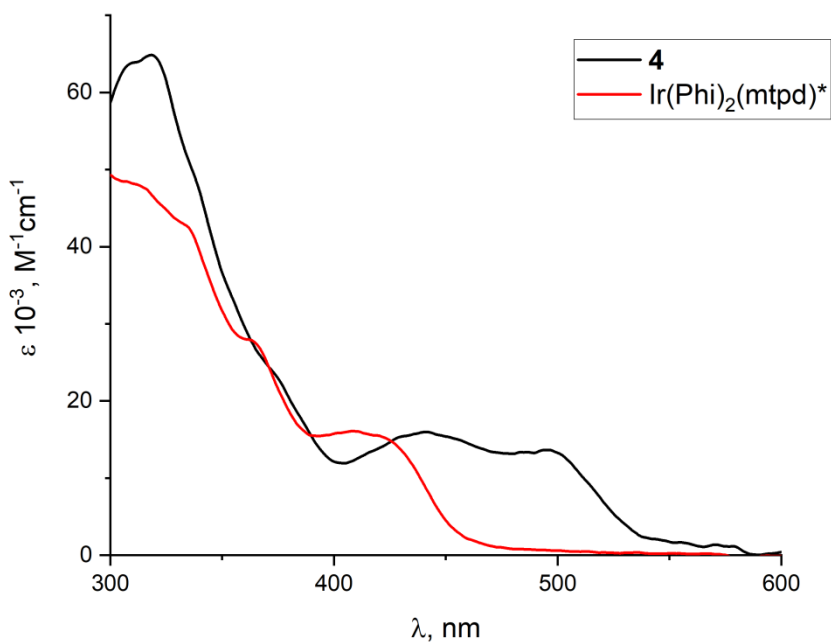


Figure S56. Comparison of absorption spectra of complex **4** with absorption spectra of $Ir(\Phi)_2(mtpd)^3$ (measured in CH_2Cl_2 at $25^\circ C$).

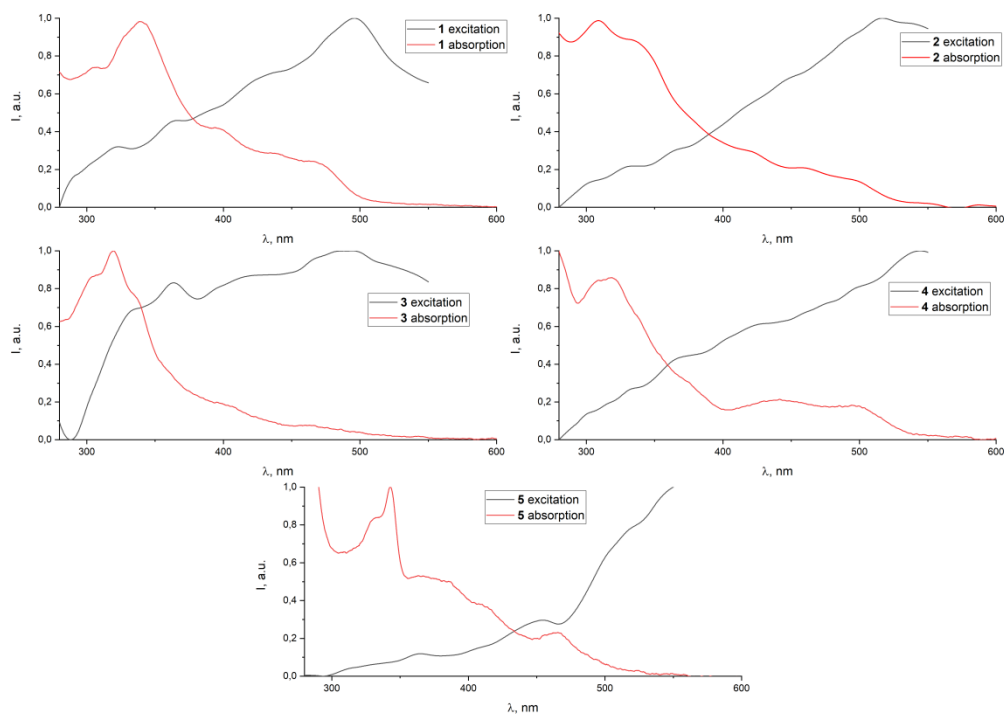


Figure S57. Excitation (—, measured in solid state at 25°C) and absorption (—, measured in CH₂Cl₂ at 25°C) spectra of complexes **1 – 5**.

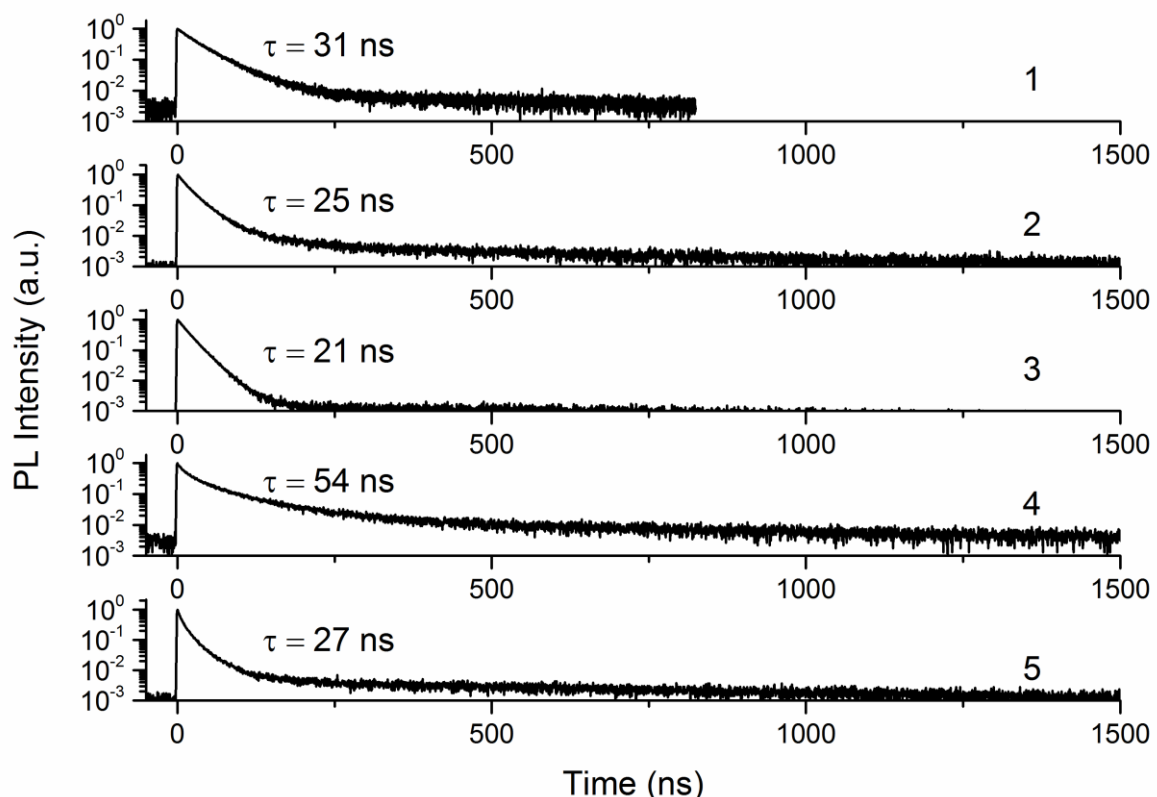


Figure S58. Photoluminescence decay curves of complexes **1 – 5**.

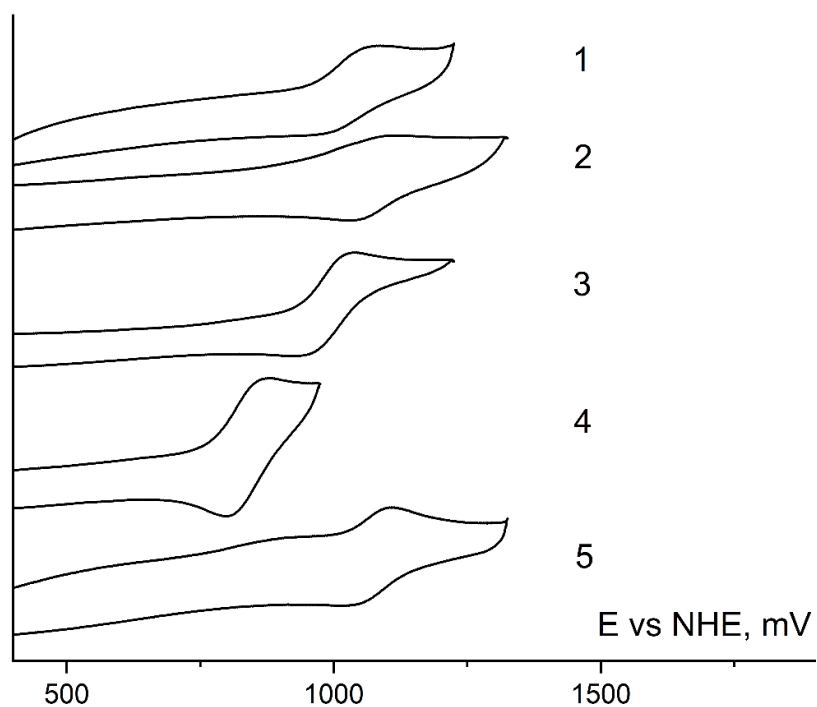


Figure S59. Cyclic voltammetry curves of complexes **1 – 5** measured in Ar-saturated CH₃CN (electrolyte – 0.1 M NBu₄ClO₄) at a scan rate of 100 mV/s.

4. Computational details.

Table S6. Selected bond lengths in optimized structures of **1 – 5** at the ground and triplet excited states.

	1	2	3	4	5
Ir – C1 (S_0 / T_1)	2.0298 / 1.9973	2.0103 / 2.0087	2.0217 / 2.0384	2.0322 / 1.9960	2.0120 / 2.0277
Ir – C2 (S_0 / T_1)	2.0308 / 2.0296	2.0084 / 1.9957	2.0241 / 2.0333	2.0227 / 2.0309	2.0102 / 2.0286
Ir – N1 (S_0 / T_1)	2.0801 / 2.0638	2.0642 / 2.0642	2.0696 / 2.0963	2.0622 / 2.0452	2.0727 / 2.0731
Ir – N2 (S_0 / T_1)	2.0905 / 2.0947	2.0604 / 2.0524	2.0755 / 2.0536	2.0534 / 2.0657	2.0733 / 2.0664
Ir – O1 (S_0 / T_1)	2.1792 / 2.1923	2.1898 / 2.1991	2.1930 / 2.1309	2.2200 / 2.2033	2.2000 / 2.1394
Ir – O2 (S_0 / T_1)	2.1785 / 2.1877	2.1840 / 2.1916	2.1984 / 2.1035	2.1806 / 2.1760	2.2027 / 2.1268

Table S7. Composition (%) of frontier molecular orbitals for **1 – 5**.

complex		1	2	3	4	5
HOMO-1	Ir	8	22	43	38	37
	C^N	91	69	35	56	48
	O^O	1	9	22	4	15
	energy, eV	-5.26	-5.31	-5.28	-4.86	-5.21
HOMO	Ir	28	30	42	38	43
	C^N	70	68	55	55	52
	O^O	2	2	3	7	5
	energy, eV	-4.78	-4.95	-4.82	-4.83	-5.02
LUMO	Ir	2	2	2	1	1
	C^N	0	1	2	1	4
	O^O	98	97	96	98	95
	energy, eV	-1.92	-1.91	-1.89	-1.82	-1.88
LUMO+1	Ir	3	3	1	1	1
	C^N	97	97	99	98	99
	O^O	0	0	0	1	0
	energy, eV	-1.55	-1.70	-1.62	-1.79	-1.74

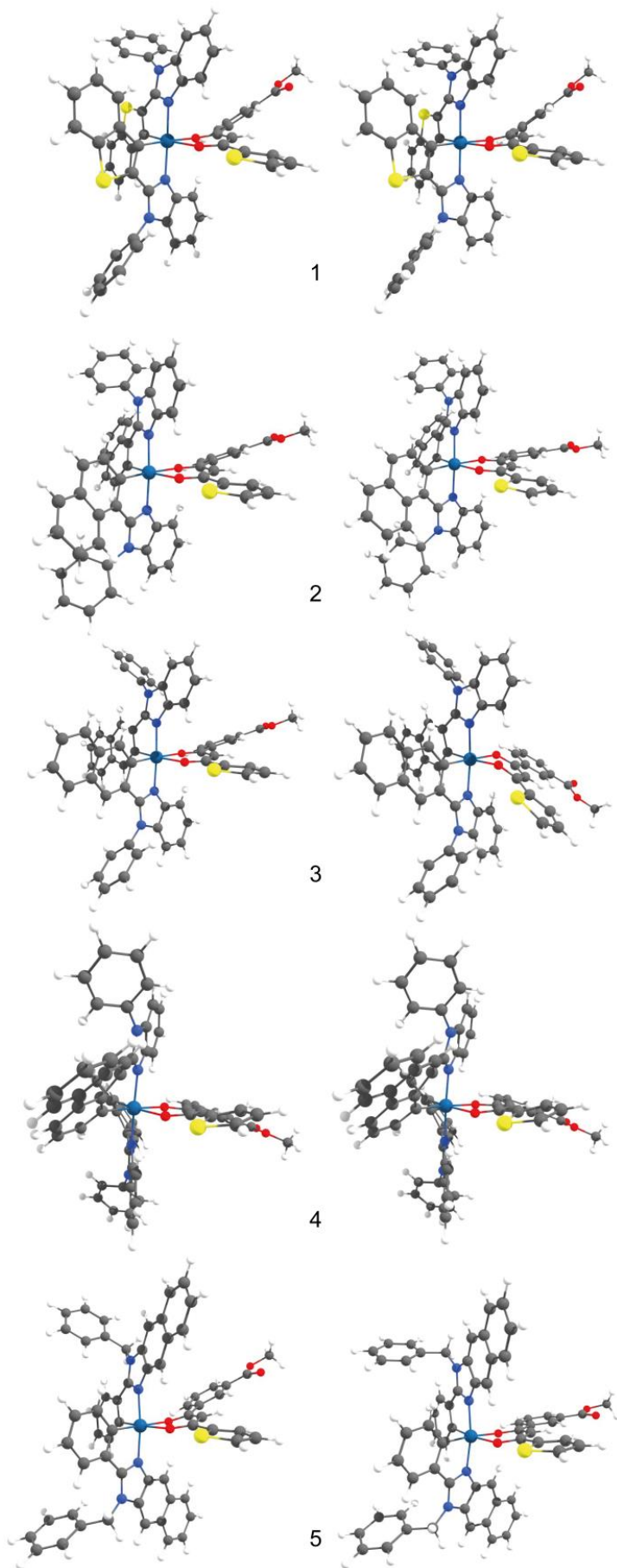


Figure S60. Optimized geometries of S_0 (left) and T_1 (right) states of complexes **1 – 5**.

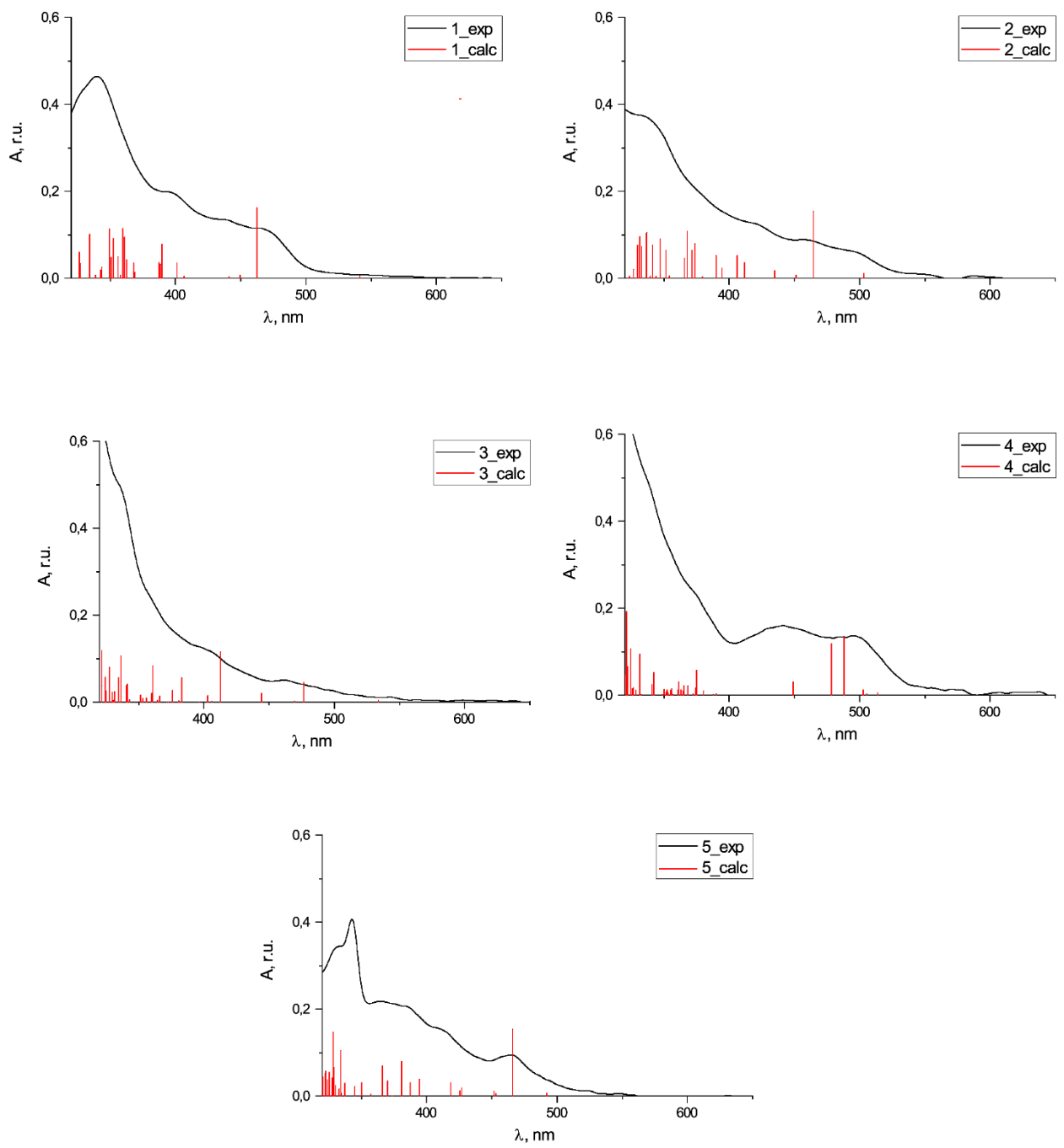


Figure S61. TDDFT electronic spectra (red) and experimental (black) UV-vis spectra of complexes **1–5**.

Table S8. TDDFT singlet excited states for **1 – 5**.

Compound	State	λ / nm (f)	Dominant monoexcitations
1	S ₁	541 (0.005)	H → L (99%), MLCT ^{O^O} +LL'CT
	S ₂	462 (0.16)	H → L+1 (93%), MLCT ^{C^N} + ILCT ^{C^N}
	S ₃	450 (0.007)	H → L+2 (92%), MLCT ^{C^N} + ILCT ^{C^N}
	S ₄	441 (0.003)	H-1 → L (93%), MLCT ^{O^O} +LL'CT
	S ₅	407 (0.003)	H → L+3 (96%), MLCT ^{O^O} +LL'CT
2	S ₁	503 (0.011)	H → L (97%), MLCT ^{O^O} +LL'CT
	S ₂	465 (0.15)	H → L+1 (94%), MLCT ^{C^N} + ILCT ^{C^N}
	S ₃	452 (0.006)	H → L+2 (93%), MLCT ^{C^N} + ILCT ^{C^N}
	S ₄	435 (0.02)	H-1 → L (93%), MLCT ^{O^O} +LL'CT
	S ₅	412 (0.04)	H-1 → L+2 (52%), H-1 → L+1 (19%), H-2 → L+2 (15%), MLCT ^{C^N} + ILCT ^{C^N}
3	S ₁	534 (0.003)	H → L (98%), MLCT ^{O^O} +LL'CT
	S ₂	477 (0.05)	H → L+1 (96%), MLCT ^{C^N} + ILCT ^{C^N}
	S ₃	469 (0.001)	H → L+2 (96%), MLCT ^{C^N} + ILCT ^{C^N}
	S ₄	444 (0.02)	H-1 → L (93%), MLCT ^{O^O} +LL'CT+ILCT ^{O^O}
	S ₅	413 (0.11)	H-2 → L (89%), MLCT ^{O^O} +LL'CT
4	S ₁	514 (0.006)	H → L (77%), H-1 → L (19%), MLCT ^{O^O} +LL'CT
	S ₂	505 (0.002)	H-1 → L (78%), H → L (18%), MLCT ^{O^O} +LL'CT
	S ₃	503 (0.012)	H → L+1 (64%), H-1 → L+1 (28%), MLCT ^{C^N} + ILCT ^{C^N}
	S ₄	488 (0.14)	H-1 → L+1 (63%), H → L+1 (25%), MLCT ^{C^N} + ILCT ^{C^N}
	S ₅	478 (0.12)	H → L+2 (63%), H-1 → L+2 (27%), MLCT ^{C^N} + ILCT ^{C^N}
5	S ₁	492 (0.007)	H → L (95%), MLCT ^{O^O} +LL'CT
	S ₂	466 (0.15)	H → L+1 (95%), MLCT ^{C^N} + ILCT ^{C^N}
	S ₃	453 (0.005)	H → L+2 (87%), MLCT ^{C^N} + ILCT ^{C^N}
	S ₄	452 (0.011)	H-1 → L (90%), MLCT ^{O^O} +LL'CT
	S ₅	427 (0.02)	H-1 → L+1 (83%), MLCT ^{C^N} + ILCT ^{C^N}

Only the first five singlet states in the visible spectral range are included. H = HOMO, L = LUMO. For the most intensive transitions ($f > 0.05$) the type of transition is also presented.

MLCT^{C^N} – metal to cyclometalated ligand charge transfer, ILCT^{C^N} – intraligand charge transfer in the cyclometalated ligand, MLCT^{O^O} – metal to diketonate ligand charge transfer, LL'CT – ligand to ligand charge transfer

Table S9. Calculated emission wavelength for complexes **1 – 5** from the triplet excited state (calculated as $\lambda = hc/\Delta E$, where ΔE is $E(T_1) - E(S_0$ in T_1 geometry)

complex	1	2	3	4	5
λ , nm	754	754	811	819	693

5. Photovoltaic measurements.

ST312H.1.fid

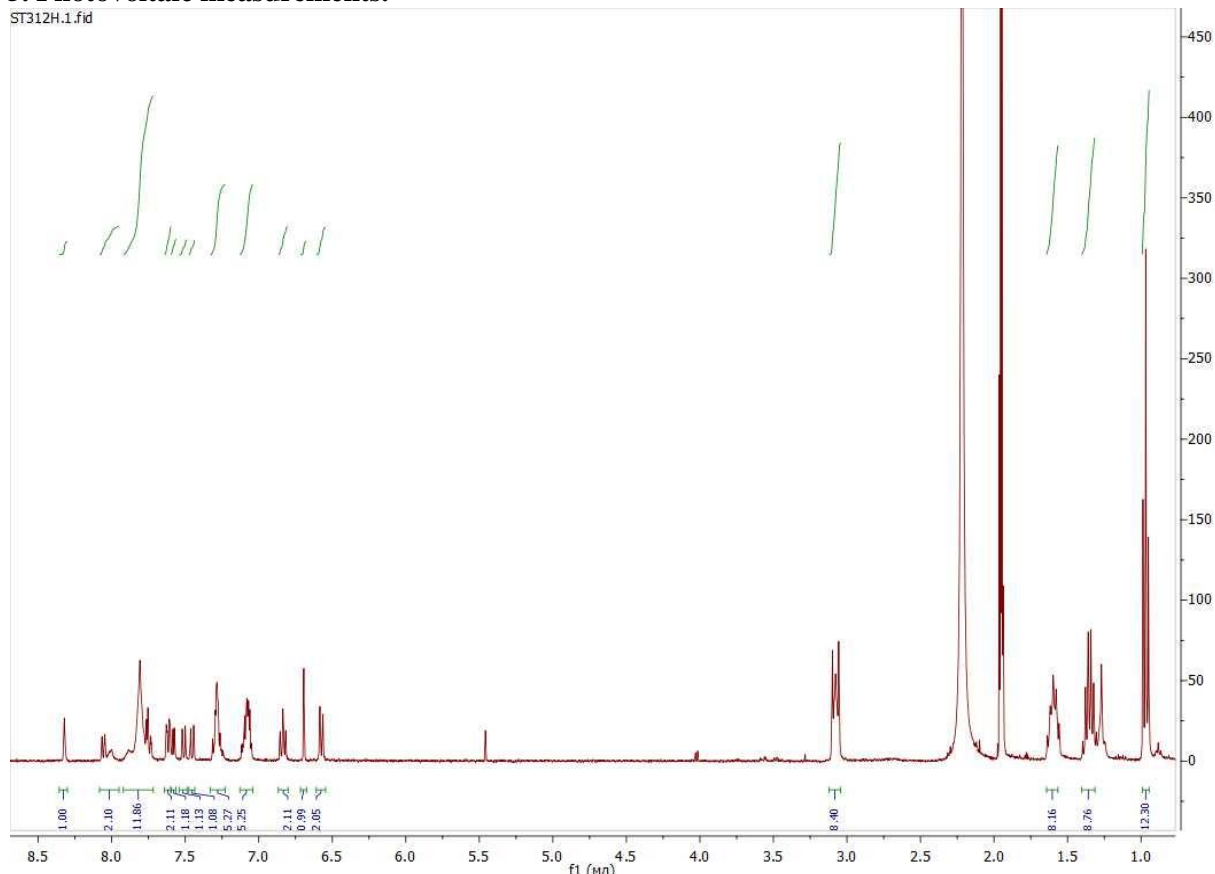


Figure S62. ¹H NMR spectrum of **1H** (400 MHz, 298K, CD₃CN).

ST321H.1.fid

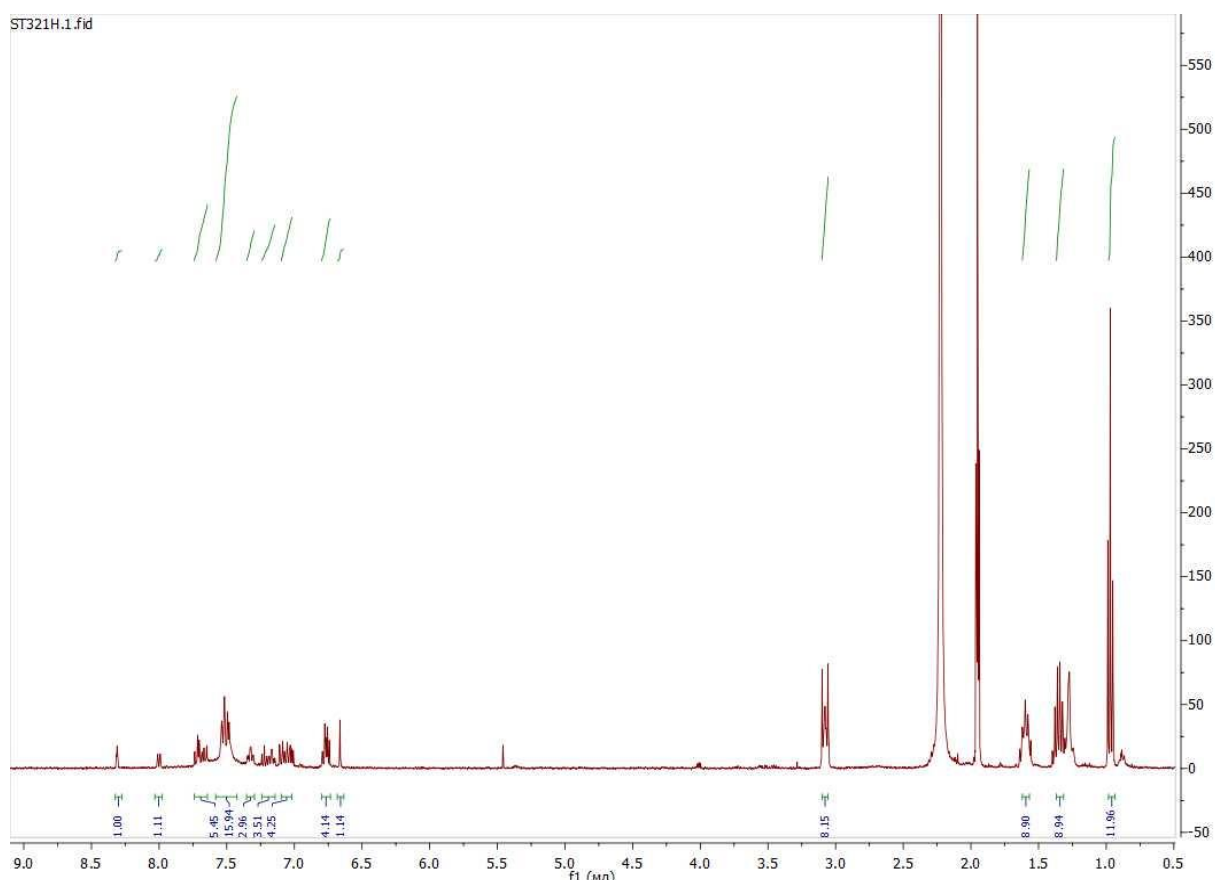


Figure S63. ¹H NMR spectrum of **2H** (400 MHz, 298K, CD₃CN).

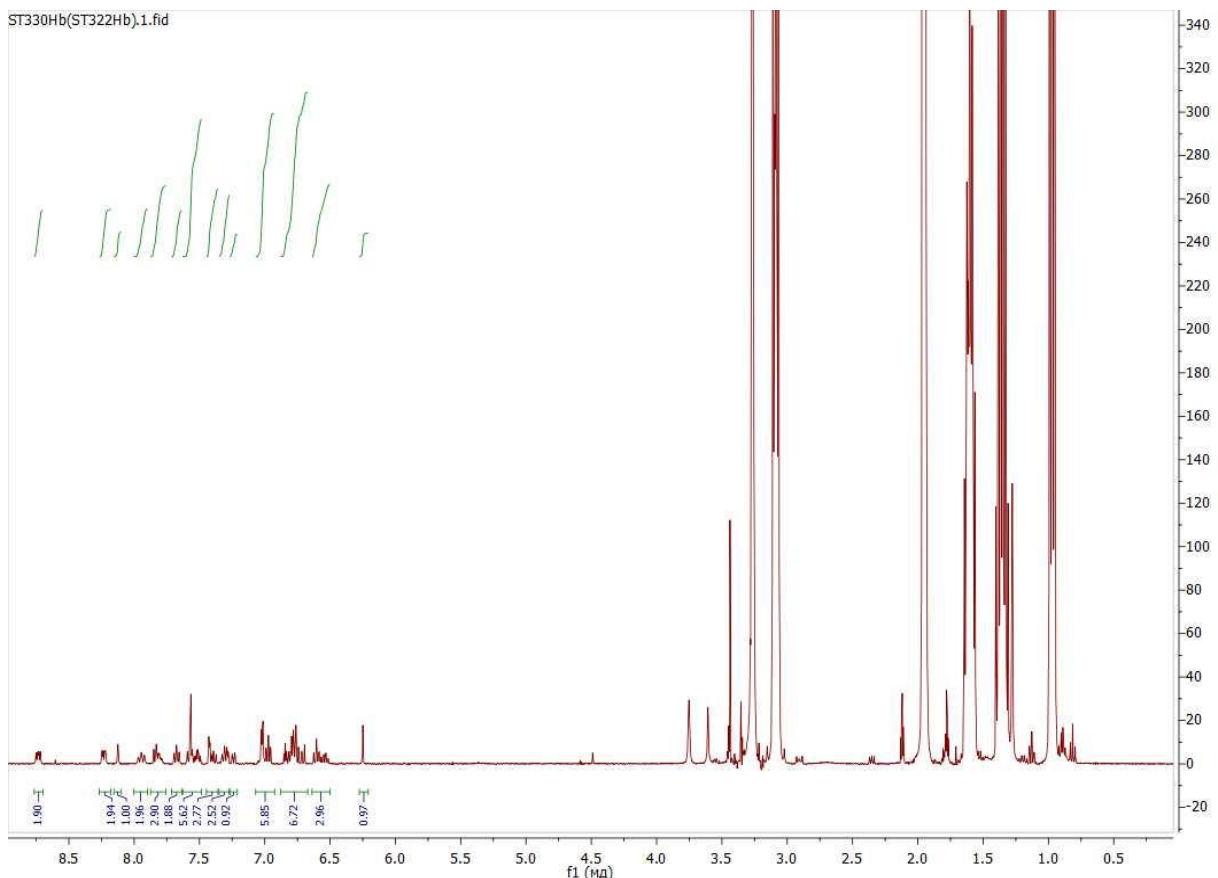


Figure S64. ^1H NMR spectrum of **4H** (400 MHz, 298K, CD_3CN). An excess of NBu_4OH was added to the sample to achieve its dissolving for NMR measurements.

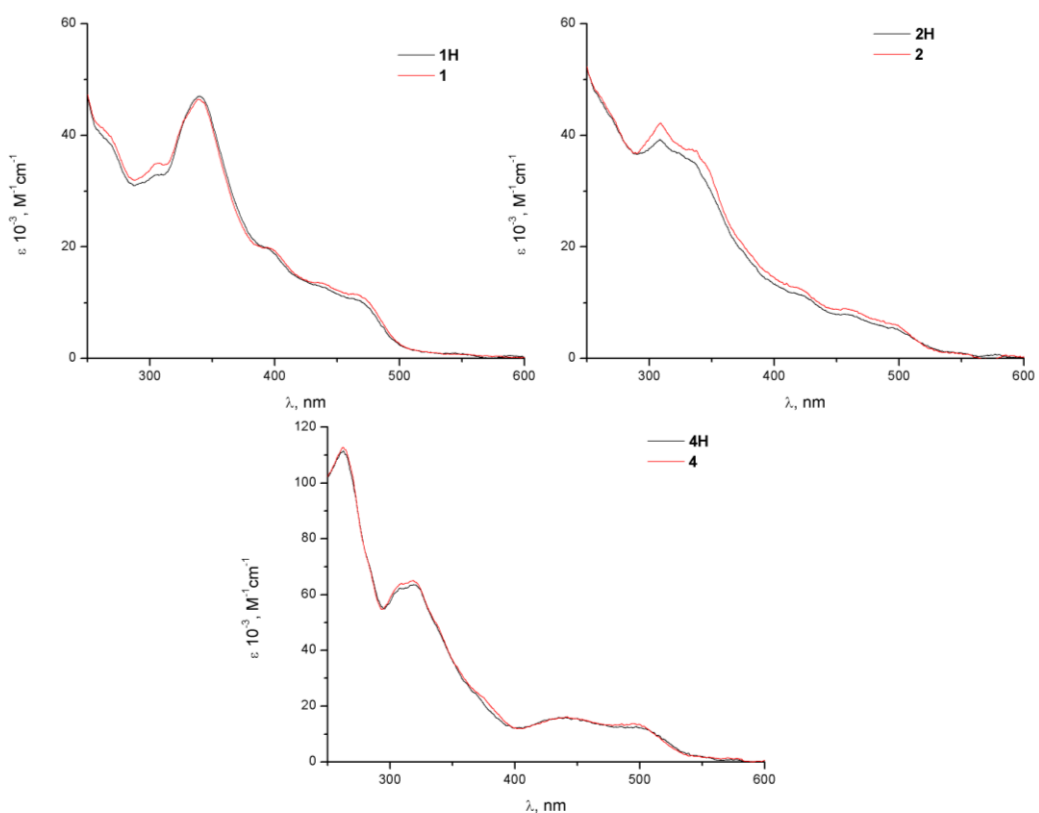


Figure S65. Comparison of absorption spectra of the complexes **1**, **2**, **4** (red lines) with spectra of corresponding hydrolysed complexes **1H**, **2H**, **4H** (black lines).

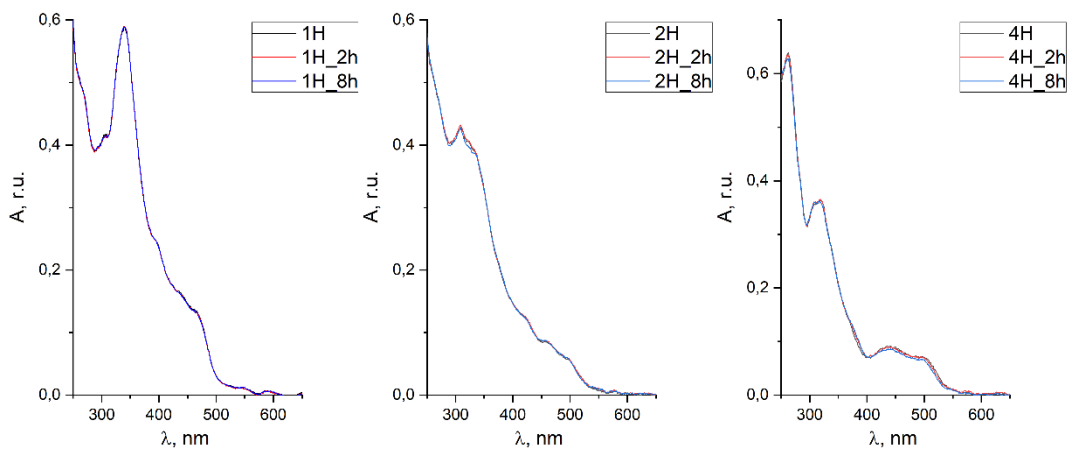


Figure S66. Photostability test of the hydrolysed complexes **1H**, **2H** and **4H**. The absorption spectra were recorded after 2 hours and 8 hours exposure of the solutions to the UV-light.

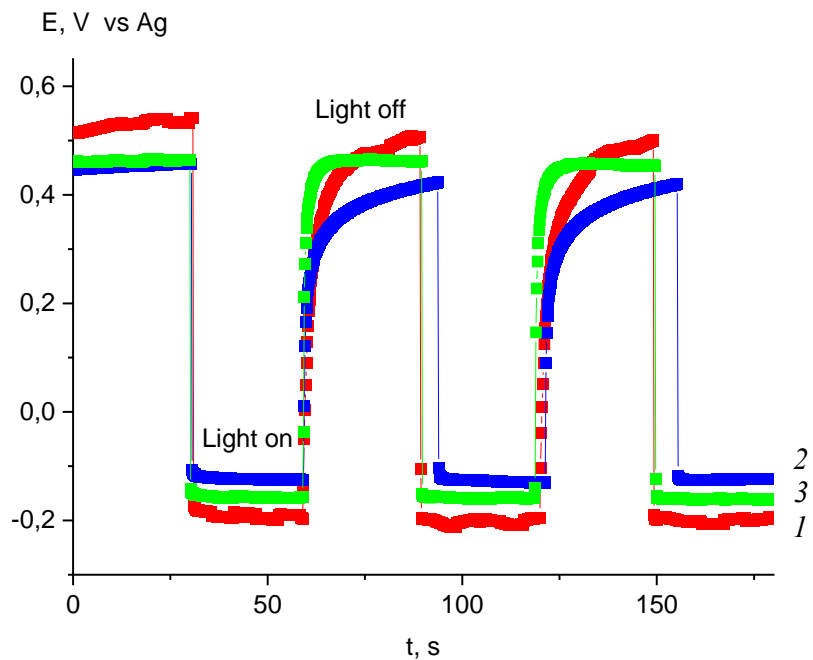


Figure S67. Time dependence of photopotential for TiO_2 photoanodes sensitized by complex **1H** (1), complex **2H** (2) and complex **4H** (3) in the dark, and on exposure to AM 1.5 G simulated solar light (100 mW cm^{-2}).

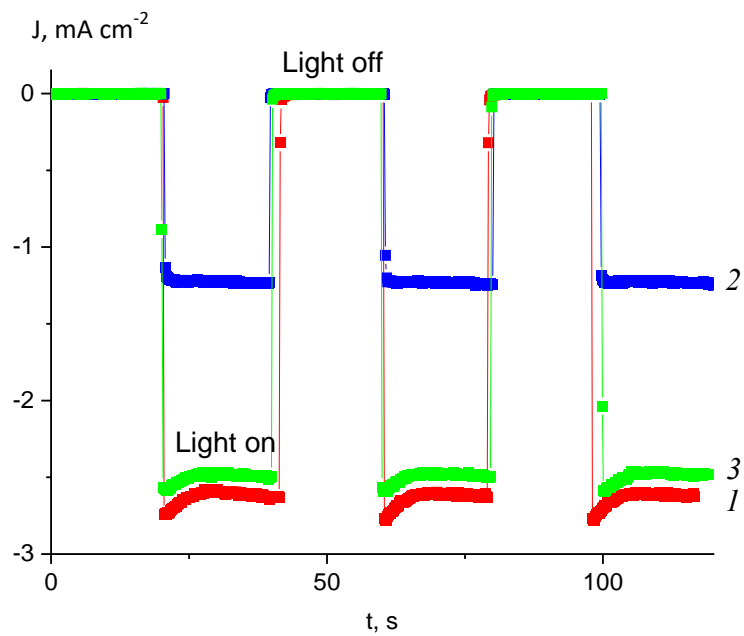


Figure S68. Time dependence of photocurrent at short-circuit for TiO_2 photoanodes sensitized by complex **1H** (1), complex **2H** (2) and complex **4H** (3) in the dark, and on exposure to AM 1.5 G simulated solar light (100 mW cm^{-2}).

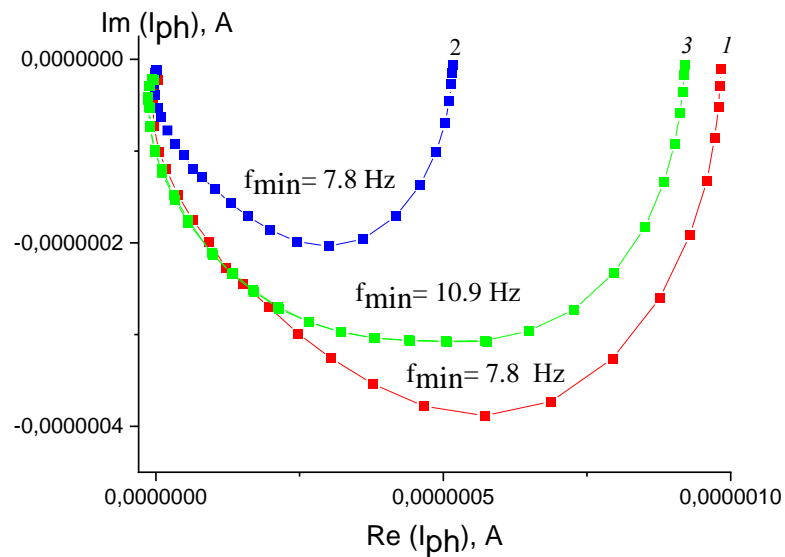


Figure S69. Intensity-modulated photocurrent spectrum (IMPS) for a TiO_2 photoanodes sensitized by complex **1H** (1), complex **2H** (2) and complex **4H** (3). Illumination by monochromatic light (453 nm) at the power of 14 mW.

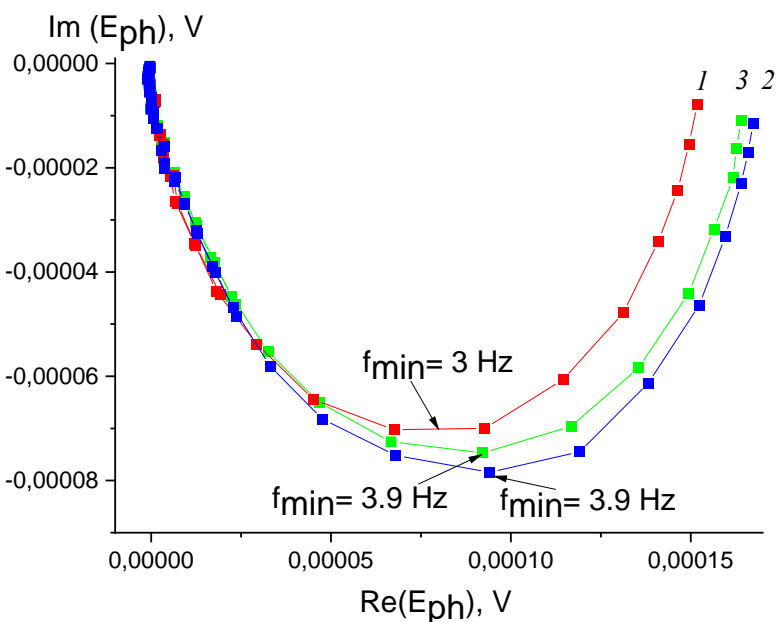


Figure S70. Intensity-modulated photo voltage spectrum (IMPS) for a TiO_2 photoanodes sensitized by complex **1H** (1), complex **2H** (2) and complex **4H** (3). Illumination by monochromatic light (453 nm) at the power of 14 mW.

References

1. A) Poater, A.; Cosenza, B.; Correa, A.; Giudice, S.; Ragone, F.; Scarano, V.; Cavallo, L., SambVca: A Web Application for the Calculation of the Buried Volume of N-Heterocyclic Carbene Ligands, *Eur. J. Inorg. Chem.* **2009**, 1759–1766. <https://doi.org/10.1002/ejic.200801160>. B) Poater, A.; Ragone, F.; Giudice, S.; Costabile, C.; Dorta, R.; Nolan, S. P.; Cavallo, L., Thermodynamics of N-heterocyclic carbene dimerization: The balance of sterics and electronics, *Organometallics* **2008**, 27, 2679–2681. <https://doi.org/10.1021/om8001119>. C) Poater, A.; Ragone, F.; Mariz, R.; Dorta, R. Cavallo, L., Comparing the Enantioselective Power of Steric and Electrostatic Effects in Transition-Metal-Catalyzed Asymmetric Synthesis, *Chem. Eur. J.* **2010**, 16, 14348–14353. <https://doi.org/10.1002/chem.201001938>.
2. Bezzubov, S. I.; Zharinova, I. S.; Khusyainova, A. A.; Kiselev, Y. M.; Taydakov, I. V.; Varaksina, E. A.; Metlin, M. T.; Tobohova, A. S.; Korshunov, V. M.; Kozyukhin, S. A.; Dolzhenko, V. D. Aromatic β -Diketone as a Novel Anchoring Ligand in Iridium(III) Complexes for Dye-Sensitized Solar Cells. *Eur. J. Inorg. Chem.* **2020** (34), 3277–3286. <https://doi.org/10.1002/ejic.202000372>.
3. Tatarin, S. V.; Kalle, P.; Taydakov, I. V.; Varaksina, E. A.; Korshunov, V. M.; Bezzubov, S. I. Sterically Hindered Phenanthroimidazole Ligands Drive the Structural Flexibility and Facile Ligand Exchange in Cyclometalated Iridium(III) Complexes. *Dalt. Trans.* **2021**, 50 (20), 6889–6900. <https://doi.org/10.1039/D1DT00820J>.